Improving volcanic ash forecasts with ensemble-based data assimilation

Fu, Guangliang

DOI
10.4233/uuid:97d82967-998a-413d-b1f8-8c46f3e064cc

Publication date
2017

Document Version
Final published version

Citation (APA)
Fu, G. (2017). *Improving volcanic ash forecasts with ensemble-based data assimilation*. [Dissertation (TU Delft), Delft University of Technology]. https://doi.org/10.4233/uuid:97d82967-998a-413d-b1f8-8c46f3e064cc

Important note
To cite this publication, please use the final published version (if applicable).
Please check the document version above.

Improving volcanic ash forecasts with ensemble-based data assimilation

Improving volcanic ash forecasts with ensemble-based data assimilation

Proefschrift

ter verkrijging van de graad van doctor
aan de Technische Universiteit Delft,
op gezag van de Rector Magnificus prof. ir. K.C.A.M. Luyben,
voorzitter van het College voor Promoties,
in het openbaar te verdedigen op maandag 9 januari 2017 om 15:00 uur

door

Guangliang Fu

Master of Science in Numerical Mathematics,
Shandong University, China
geboren te Shandong, China

Dit proefschrift is goedgekeurd door de

promotor: Prof. dr. ir. H.X. Lin
promotor: Prof. dr. ir. A.W. Heemink

Samenstelling promotiecommissie:

Rector Magnificus,	voorzitter
Prof. dr. ir. H.X. Lin,	Technische Universiteit Delft, Promotor
Prof. dr. ir. A.W. Heemink,	Technische Universiteit Delft, Promotor
Onafhankelijke leden:	
Prof. dr. ir. R.F. Hanssen,	Technische Universiteit Delft
Prof. dr. M. Schaap,	Free University of Berlin, Germany
Prof. dr. B. Wang,	Tsinghua University, China
Prof. dr. R. Heana,	University of Stavanger, Norway
Prof. dr. ir. C. Vuik,	Technische Universiteit Delft, reservelid
Overige leden:	
Dr. ir. A.J. Segers,	TNO Utrecht, The Netherlands

Dr. ir. A.J. Segers heeft in belangrijke mate aan de totstandkoming van het proefschrift bijgedragen.

Keywords: ensemble-based data assimilation, volcanic ash forecasts, aviation advice, aircraft measurement, spurious correlations, satellite measurement, high performance computing

Printed by: Ipskamp Printing

ISBN 978-94-92516-34-3

An electronic version of this dissertation is available at
http://repository.tudelft.nl/.

To be quiet, for science

— My Father

Contents

Summary

The 2010 Eyjafjallajökull volcano eruption had serious consequences to civil aviation. This has initiated a lot of research on volcanic ash forecasting in recent years. For forecasting the volcanic ash transport after eruption onset, a volcanic ash transport and diffusion model (VATDM) needs to be run with Eruption Source Parameters (ESPs) such as plume height and mass eruption rate as input, and with data assimilation techniques to continuously improve the forecast. Reliable and accurate ash measurements are crucial for providing successful ash clouds advices. In the first phase of this research work, simulated aircraft-based volcanic ash measurements, will be assimilated into a transport model to identify the potential benefit of this kind of observations in an assimilation system. The results show that assimilating aircraft-based measurements can improve the state of ash clouds, and can provide an improved forecast. We also show that for an advice on the aeroplane flying level, aircraft-based measurements should preferably be taken at this level. Furthermore it is shown that in order to make an acceptable advice for aviation decision makers, accurate knowledge about uncertainties of ESPs and measurements is of great importance.

The forecast accuracy of distal volcanic ash clouds is important for providing valid aviation advice during volcanic ash eruptions. However, because the distal part of a volcanic ash plume is far from the volcano, the influence of eruption information on this part becomes rather indirect and uncertain, resulting in inaccurate volcanic ash forecasts in these distal areas. In this thesis, we use real-life aircraft in situ observations, measured in the North-West part of Germany during the 2010 Eyjafjallajökull eruption, in an ensemble-based data assimilation system to investigate the potential improvement on the forecast accuracy with regard to the distal volcanic ash plume. We show that the error of the analyzed volcanic ash state can be significantly reduced by assimilating real-life in situ measurements. After assimilation, it is shown that the model-based aviation advice for Germany, the Netherlands and Luxembourg can be improved. We suggest that with suitable aircrafts measuring once per day across the distal volcanic ash plume, the description and prediction of volcanic ash clouds in these areas can be improved significantly.

Among the data assimilation approaches, the ensemble Kalman filter (EnKF) is a well-known and popular method. A proper covariance localization strategy in the analysis step of EnKF is essential for reducing spurious covariances caused by the finite ensemble size, as shown for this application for assimilation of aircraft in situ measurements. After analyzing the characteristics of the physical forecast error covariances, we present a two-way tracking approach to define the localization matrix for covariance localization. The result shows that the Two-way-tracking Localized EnKF (TL-EnKF) effectively maintains the correctly specified physical covariances

and largely reduces the spurious ones. The computational cost of TL-EnKF is also evaluated and is shown to be advantageous for both serial and parallel implementations. Compared to the commonly used distance-based covariance localization, the two-way tracking approach is shown to be more suitable. In addition, the covariance inflation approach is verified as an additional improvement to TL-EnKF to achieve more accurate results.

A timely prediction requires that the computations of the data assimilation system can be performed quickly (at least than the Wall-clock). We therefore investigate strategies for accelerating the data assimilation algorithm. Based on evaluations of the computational time, the analysis step of the assimilation turns out to be the most expensive part. After a study on the characteristics of the ensemble ash state, we propose a mask-state algorithm which records the sparsity information of the full ensemble state matrix and transforms the full matrix into a relatively small one. This will reduce the computational cost in the analysis step. Experimental results show the mask-state algorithm significantly speeds up the analysis step. Subsequently, the total amount of computing time for volcanic ash data assimilation is reduced to an acceptable level. The mask-state algorithm is generic and thus can be embedded in any ensemble-based data assimilation framework. Moreover, ensemble-based data assimilation with the mask-state algorithm is promising and flexible, because it implements exactly the standard data assimilation without any approximation and it realizes the satisfying performance without any change of the full model.

Infrared satellite measurements of volcanic ash mass loadings are often used as input observations for the assimilation scheme. However, these satellite-retrieved data are often two-dimensional (2D), and cannot easily be combined with a three-dimensional (3D) volcanic ash model to improve the volcanic ash state. By integrating available data including ash mass loadings, cloud top heights and thickness information, we propose a satellite observational operator (SOO) that translates satellite-retrieved 2D volcanic ash mass loadings to 3D concentrations at the top layer of the ash cloud. Ensemble-based data assimilation is used to assimilate the extracted measurements of ash concentrations. The results show that satellite data assimilation can force the volcanic ash state to match the satellite observations, and that it improves the forecast of the ash state. Comparison with highly accurate aircraft in situ measurements shows that the effective duration of the improved volcanic ash forecasts is about a half day.

Samenvatting

De uitbarsting van vulkaan Eyjafjallajökull in 2010 had ernstige gevolgen voor de burgerluchtvaart. Dit heeft geleid dat veel onderzoek naar de verspreiding van vulkanische as zijn gestart in de afgelopen jaren. Voor het voorspellen van de vulkanische as transport nadat die in de lucht is gekomen via uitbarsting, een vulkanische as transport en diffusie model (VATDM) dient te worden uitgevoerd met als invoer de Eruption Source parameters (ESP's), zoals pluim hoogte en snelheid van massa-uitspuit. Deze simulatie resultaten kunnen met data-assimilatie technieken continu worden verbeterd voor een betere prognose. Betrouwbare en accurate metingen van as concentratie zijn van cruciaal belang voor het verstrekken van een succesvolle aswolken adviezen. In de eerste fase van dit onderzoek, gesimuleerdevliegtuigen op basis van vulkanische as metingen, wordt geassimileerd in een transportmodel om de effecten van dit soort observaties in een assimilatie systeem te bestuderen. De resultaten tonen aan dat assimilatie op basis vliegtuig metingen de berekende resultaten over de aswolken kan verbeteren die weer tot een verbeterde prognose kan leiden. We tonen ook aan dat voor een advies met betrekking tot het wel/niet vliegen, vliegtuigmetingen bij voorkeur op de normale vlieghoogte moeten worden gedaan. Voorts wordt aangetoond dat ter ondersteuning van het maken van een betrouwbaar advies door de luchtvaart autoriteit, accurate kennis over de onzekerheden van de ESP's en metingen van groot belang is.

De voorspellingsnauwkeurigheid van de distale vulkanische aswolken is belangrijk voor het verstrekken van geldig luchtvaartadvies tijdens de vulkanische as uitbarstingen. Omdat het distale deel van een vulkanische aswolk ver van de vulkaan is, wordt de invloed van uitbarsting gegevens (zoals ESP's) op dit deel nogal onzeker en indirect, wat resulteert in onnauwkeurige vulkanische as prognoses in deze distale gebieden. In dit proefschrift maken we gebruik van real-life vliegtuigen in situ waarnemingen, gemeten in het noordwesten van Duitsland tijdens de 2010 Eyjafjallajökull uitbarsting, in een ensemble-gebaseerde data assimilatie systeem om de prognose ten aanzien van de distale vulkanische aswolk te verbeteren. We laten zien dat de fout van de geanalyseerde vulkanische as staat aanzienlijk kan worden verminderd door het assimileren van in situ metingen. We laten zien dat na de assimilatie de modelmatige luchtvaart advies voor Duitsland, Nederland en Luxemburg wordt verbeterd. Op basis van deze studie constateren we dat het een keer per dag meten over de distale vulkanische aswolk met geschikte vliegtuigen, de beschrijving en voorspellen van vulkanische aswolken boven verre gebieden aanzienlijk kan worden verbeterd.

Onder de data-assimilatie benaderingen, het ensemble Kalman filter (EnKF) is een bekende en populaire methode. Een goede covariantie lokalisatiestrategie in de analysestap van EnKF is essentieel voor het verminderen van valse covarianties

die door de eindige ensemble grootte, zoals voor deze toepassing voor assimilatie van vliegtuigen in situ afmetingen, zijn veroorzaakt. Na analyse van de kenmerken van de fout in covarianties, presenteren we een tweerichtings volgmethode om de lokalisatie matrix voor covariantie-lokalisatie te definiëren. Het resultaat toont aan dat de Two-way-tracking Localized EnKF (TL-EnKF) methode de correcte fysieke covarianties effectief handhaaft en tegelijkertijd valse covarianties grotendeels vermindert. Evaluaties van computationele kosten van TL-EnKF laten zien dat het voordelig is voor zowel seriële en parallelle implementaties. Bovendien laat deze nieuwe lokalisatieaanpak zich makkelijk met de covariantie inflatie benadering combineren wat tot een verder verbetering in de nauwkeurigheid kan leiden.

Een tijdige voorspelling vereist dat de berekeningen van het data assimilatie systeem snel kan worden uitgevoerd (in ieder geval sneller dan de muurklok). We onderzoeken daarom strategieën voor het versnellen van het data assimilatie algoritme. Op basis van analyse van de rekentijd in verschillende onderdelen, blijkt de analysestap van de assimilatie het meest tijdrovende onderdeel te zijn. Na onderzoek van de kenmerken van typische vulkaanas verspreiding , stellen we een masker algoritme voor dat de ijlheid van de volledige ensemble-staat matrix registreert en de volledige matrix naar een betrekkelijk kleine matrix transformeert. Computer experimenten tonen aan dat het masker algoritme de analysestap aanzienlijk versnelt. Aanvankelijk duurt een voorspelling met data assimilatie langer dan de muurklok, na deze optimalisatie met het masker algoritme wordt de totale rekentijd voor vulkanische as data assimilatie gereduceerd tot een aanvaardbaar niveau. Het masker algoritme is generiek en dus kan in een ensemble-gebaseerde data assimilatie kader worden ingebed. Ensemble gebaseerde data assimilatie met het masker algoritme is veelbelovend en flexibel, omdat het precies het standaard data-assimilatie algoritme implementeert zonder enige benaderingen en bevredigende prestaties realiseert zonder enige verandering in het volledige model.

Infrarood satellietmetingen van vulkanische as-massa-ladingen worden vaak gebruikt als input waarnemingen voor het assimilatie systeem. Echter, deze satelliet-teruggehaalde gegevens zijn vaak tweedimensionaal (2D), en kunnen niet eenvoudig worden gecombineerd met een driedimensionaal (3D) vulkanische as model. Door integratie van de beschikbare gegevens, inclusief as-massa-ladingen, aswolk tophoogte en dikte informatie, ontwerpen we een satelliet observationele operator (SOO) die satelliet teruggehaalde 2D vulkanische as-massa-ladingen naar 3D concentraties aan de toplaag van de aswolk vertaalt. Ensemble gebaseerde assimilatie wordt vervolgens gebruikt om de geëxtraheerde as concentraties te assimileren. De resultaten tonen aan dat satellietgegevens assimilatie de voorspelde as concentraties dichter bij de satellietwaarnemingen brengt en een nauwkeurigere prognose oplevert. Vergelijking met zeer nauwkeurige vliegtuigen in situ metingen blijkt dat de effectieve duur van de verbeterde vulkanische as prognoses ongeveer een halve dag is.

1

Introduction

*The April–May 2010 eruption of Eyjafjallajökull volcano (Iceland) caused an unprecedented closure of the European and North Atlantic airspace with global economic losses of **5 billion** US dollars.*

Oxford-Economics (2010)

We must make decisions based on the real situation in the sky, not on theoretical models

Nature 464, 1253 (2010)

1

1.1. Motivation

Figure 1.1: Eyjafjallajökull volcano eruption plume.

The volcanic activity of Eyjafjallajökull in Iceland in 2010 (Figure 1.1) has shown that air traffic is highly vulnerable to volcanic eruptions. Volcanic ash is dangerous to commercial jet aircraft (Casadevall, 1994). Volcanic ash contains micron-size silicate particles that can melt in the hot parts of jet turbine engines. Little is known about the exact atmospheric concentrations of ash that cause build-up on the jet turbine, but now the current regulation states that the highest concentration an aircraft can endure is 4000 μg m^{-3} (EASA, 2015). Until carefully designed engine performance tests are conducted in realistic volcanic ash cloud conditions, a cautious approach to advising commercial jet operations in airspace affected by volcanic ash is recommended. For example, the sudden eruption of the Eyjafjallajökull volcano in Iceland from 14 April to 23 May 2010, had caused an unprecedented closure of the European and North Atlantic airspace resulting in a huge global economic loss up to 5 billion US dollars (Bonadonna *et al.*, 2012). Due to the huge impacts on aviation community, a lot of research has been initiated on how to efficiently reduce these aviation impacts, starting with improving the accuracy of volcanic ash forecast after eruption onset (Eliasson *et al.*, 2011; Schumann *et al.*, 2011).

1.2. Volcanic ash transport models

For forecasting volcanic ash plumes, numerous volcanic ash transport and dispersion models (VATDM) are available worldwide, and in recent efforts a comparison report among these existing models has been compiled (Bonadonna *et al.*, 2012, 2014). These models are usually off-line coupled to a meteorological model, which require that numerical weather prediction data should be generated first such that the VATDM could use these data. For the transport either Lagrangian or Eulerian approach are used. Some models run quickly such as PUFF (Searcy *et al.*, 1998) can run within minutes and others require many hours to run, such as ATHAM (Ober-

huber *et al.*, 1998) requires several days. Several VATDM are used in operational settings, like NAME (Jones *et al.*, 2007) and HYSPLIT (Draxler and Hess, 1998) and therefore are designed to produce volcanic ash simulations quickly for the corresponding volcanic ash advisory center. Inter-comparisons between volcanic ash transport and dispersion models, volcanic ash real-time advisories as well as to the satellite observations have been reported by multiple authors, such as (Witham *et al.*, 2007) and (Webley *et al.*, 009b).

The meteorological wind fields and estimates of Eruption Source Parameters (Mastin *et al.*, 2009) (ESPs) such as Plume Height(PH), Mass Eruption Rate (MER), Particle Size Distribution (PSD) and Vertical Mass Distribution (VMD) are needed as input to the VATDM model. A VATDM uses physical parameterizations of source and removal processes that affect the concentrations in the dispersing volcanic cloud. Aggregation of ash particles and subsequent enhanced removal is an extremely important process for estimating the atmospheric ash burden (Durant *et al.*, 2010), yet this process is not included in most dispersion models because of its complexity and the demand on computation time (Folch *et al.*, 2010). Without accurate knowledge of the temporal variation of the mass eruption rate at the volcano and particle removal rate in the atmosphere, it is not possible to provide accurate quantitative forecasts of the ash concentrations arriving in the airspace over a long distance (Prata and Prata, 2012).

In this thesis, the LOTOS-EUROS (abbreviation of LOng Term Ozone Simulation – EURopean Operational Smog) model is used (Schaap *et al.*, 2008) with model version 1.10. This model is an operational air-quality model, used for daily air quality forecasts over Europe (Curier *et al.*, 2012), focussing on ozone, nitrogen oxides, and particular matter. In addition, it could be configured to simulate transport of tracers in other regions of the world. The model uses the off-line approach and is driven by meteorological data produced by European Centre for Medium-Range Weather Forecasts (ECMWF). The model is used in a tracer mode to produce volcanic ash simulations in a timely and useful manner for forecasting.

1.3. Data assimilation identified as a research priority

To improve the accuracy of volcanic ash concentration forecasts, efficient technologies must be employed to compensate the VATDM's inaccuracies. As a result of the serious consequences on civil aviation, more than 50 volcanologists, meteorologists, atmospheric dispersion modellers, and space and ground-based monitoring specialists from 12 different countries (including representatives from 6 Volcanic Ash Advisory Centers and related institutions) gathered at the Weather Meteorology Organization (WMO) headquarters in Geneva, addressing some important research priorities related to Volcanic Ash Transport Forecast problems (Bonadonna *et al.*, 2012). One of the priorities they identified was to use data assimilation (Zehner, 2010), which had not been tried/employed for volcanic ash forecasts. Ensemble-based data assimilation, which refers to the sequential use of the direct measurements to create accurate initial conditions for model runs (Zehner, 2010), is one of

the most commonly used approaches for real-time forecasting problems (Evensen, 2009). In each assimilation step, a forecast from the previous model simulation is used as a first guess, using the available observation this forecast is modified in better agreement with these observations.

Ensemble-based data assimilation (Evensen, 1994, 2003) can be used to compensate for the problems of employing inaccurate ESPs by continuously assimilating in situ observations to estimate volcanic ash concentrations. This approach has been successfully applied in many atmospheric applications, such as weather forecasting (Houtekamer and Mitchell, 2001) or ozone forecasting (Curier *et al.*, 2012). It has been proposed that for real-time applications, the ensemble size can be limited to 10 – 100 for cost effectiveness (Barbu *et al.*, 2009).

This thesis is the first study on volcanic ash data assimilation, which is aimed to guide the followers on (1) how much ensemble-based data assimilation can contribute to the ash forecasting/aviation community; (2) how to efficiently perform an ensemble-based data assimilation method.

1.4. Volcanic ash measurements

Ensemble-based assimilation is an effective approach where valid real-life volcanic ash measurements are necessary and required to guarantee the forecast accuracy. Fortunately, during volcanic ash transport, different types of scientific measurement campaigns are performed to gather information about the nature and occurrence of the ash plume. The measurements contained e.g., ground-based lidar and ceilometer measurements (Pappalardo *et al.*, 2010; Wiegner *et al.*, 2012), satellite observations (Stohl *et al.*, 2011; Prata and Prata, 2012; Lu *et al.*, 2016a), aircraft-based measurements (Schumann *et al.*, 2011; Weber *et al.*, 2012; Schäfer *et al.*, 2011), ground-based in situ measurements (Emeis *et al.*, 2011), balloon measurements (Flentje *et al.*, 2010) and ground-based remote sensing Sun photometer observations (Ansmann *et al.*, 2010).

Among these measurements, aircraft-based measurements were obtained close to the eruption plume, which are probably the most direct observations possible. These aircraft-based data has some advantages compared with other types of measurements: (1) The aircraft measurement is frequently obtained from the optical particle counters which are equipped on the aircraft, thus the particle concentration observation is real-time and directly detected and it has a higher accuracy. With an error estimate of about 10 percent, which can be achieved by well calibrated instruments (Weber *et al.*, 2012), the accuracy of these observations is high compared to for example satellite data, for which errors 50-60 percent are reported (Zehner, 2010). (2) The aircraft measurement is in situ which is suitable to be compared directly to a 3-dimensional model state, whereas some other measurements such as satellite data and LIDAR data observe optical properties being accumulated into a single value per vertical column which cannot be compared directly to a 3D model state. (3) An aircraft can decide the route in the sky to follow the ash cloud to always get an appropriate ash concentration. And it can also decide to fly at different altitudes, e.g., if we mainly care about the intercontinental commercial aircraft safety, we can choose to fly at 9 km with a suitable research aircraft (which is com-

monly the lowest height level for intercontinental commercial planes) to perform measurements. Note that most national and maybe some continental passenger flights are below 9 km altitude, while intercontinental flights are at 9 km and higher altitude.

Besides aircraft measurements, satellite measurements are also of interest, because the detection domain is large and the output data is long-time continuous. For example, the Spin Enhanced Visible and Infrared Imager (SEVIRI, on board the Meteosat Second Generation (MSG) platform provides a large view coverage of the atmoshere and earth's surface from 70° S to 70° N and 70° W to 70° E (Schmetz *et al.*, 2002). There are 3712 × 3712 pixels covering the full-disk. Images can be acquired for the whole disk every 15 minutes. These satellite data have been used for many years to retrieve ash mass loadings in a dispersing volcanic plume (Zehner, 2010). Nowadays, ash mass loadings (Prata and Prata, 2012), the effective particle size (Kylling *et al.*, 2015) as well as the ash cloud top height (Francis *et al.*, 2012), are available in near real-time as satellite products during volcanic plume transport.

1.5. Research questions

As mentioned in the previous section, data assimilation has been identified as a research priority for volcanic ash forecast and available volcanic ash measurements. This thesis is aimed to investigate the improvements of volcanic ash forecasts using ensemble-based data assimilation to assimilate the available measurements.

Aircraft measurement, as the most direct observations possible for volcanic ash plume (as introduced in Section 1.4), will be first considered in this thesis. Previously (before the year 2015), the aircraft-based measurements were mainly used for validation purpose of volcanic ash clouds (Weber *et al.*, 2012), not involved in data assimilation systems. This thesis will first assimilate aircraft-based measurements in the ensemble-based data assimilation scheme. Thus the first research question in this thesis is

RQ1: What is the potential benefit of assimilating aircraft measurements in a volcanic ash data assimilation system?

To avoid irrelevant influences of long-distance transport on the assimilation results, the focus of this invesigation was on the near-volcano areas where the uncertainties on plume height and mass eruption rate have a large influence on the estimates of the forecasted ash concentrations.

For distal volcanic ash plume, the eruption parameters hardly improve the forecasts over a long distance. A larger mass eruption rate may cause the distal volcanic ash plume to spread stronger and wider after a long time period. But this potential effect can be significantly influenced or even canceled out by a combination of a number of elusive physical factors over a long time period such as wind speed and direction. Thus the results on near-volcano areas cannot be directly employed for far-volcano regions, e.g., central Europe in the case of a volcanic eruption in Iceland. Thus

RQ2: How to evaluate the improvements of aircraft data assimilation for the distal volcanic ash foreasts and regional aviation advice?

is the second research question in this thesis.

Because of the limited ensemble size, ensemble-based assimilation methods often produce severe spurious covariances between measurements and state variables (Houtekamer and Mitchell, 1998; Anderson, 2001). This side effect implies that the state variables (which are in fact independent with an observation) are computed as dependent, resulting in an unphysical update. Over time, this will lead to an erroneous reduction of ensemble variance which may significantly underestimate the true variance and finally may lead to filter divergence (Anderson, 2001; Evensen, 2009). Covariance localization is a known approach to overcome this problem (Petrie and Dance, 2010), but

RQ3: How can an accurate covariance localization for volcanic ash application be chosen to remove spurious covariances due to using a finite ensemble size in ensemble-based data assimilation?

remains unknown and will be investigated as the third research question in this thesis.

To make the methodology of assimilating aircraft data efficient also in an operational (real-time) sense, the computational efforts must be acceptable (at least than the Wall-clock). For volcanic ash assimilation problems, so far, no studies on the computational aspects have been reported in the literature. Actually, when large amounts of volcanic ash erupted into atmospheres, the computational speed of volcanic ash forecasts is just as important as the forecast accuracy (Zehner, 2010). The accuracy of volcanic ash transport is aimed to be investigated based on the research questions RQ1–RQ3, thus it is urgent to also consider the computational aspect, i.e., improving the computational speed of the volcanic ash assimilation system as fast as possible.

RQ4: How can the aircraft data assimilation be accelerated to provide timely volcanic ash forecasts?

is the fourth research question of this thesis.

Besides aircraft data assimilation, the availability of satellite-based data (as introduced in Section 1.4) provides us with an opportunity to employ data assimilation with a VATDM to continuously correct the volcanic ash state, and then improve the forecast accuracy of volcanic ash concentrations. There still exist difficulties on how to efficiently use satellite-retrieved volcanic ash mass loadings, because a VATDM is in most cases a 3D model, while the retrieved ash mass loadings are 2D data. One 2D mass loading can be considered as an integral of ash concentrations along a retrieval path (the path can be a line or a curve which depends on a specified retrieval algorithm) (Prata and Prata, 2012). Thus, the 2D measurements are not directly suited in a 3D data assimilation system.

RQ5: How can the 2D accumulated satellite retrieved measurements be assimilated in an ensemble-based assimilation system?

is the fifth research question of this thesis. How to construct an operator to make both types of information directly comparable remains an essential part for RQ5 to efficiently use satellite data in ensemble-based assimilation systems.

1.6. Organizations of this thesis

This thesis is organized as follows. Chapter 1 gives an overall motivation and introduces the problems studied in this thesis. Chapter 2 introduces the LOTOS-EUROS model to simulate volcanic ash transport, and also describes the methodology of ensemble-based data assimilation. Chapter 3 studies the potential benefit of aircraft observations in an ensemble-based assimilation system. Chapter 4 investigates the improvements on the forecast accuracy and regional aviation advice with regard to the distal volcanic ash plume. In Chapter 5, a two-way-tracking localization is proposed to maintain the correctly specified physical covariances and to largely reduce the spurious ones. In Chapter 6, a mask-state algorithm is proposed to accelerate aircraft data assimilation. Besides previous aircraft data assimilation, Chapter 7 proposes a satellite observational operator (SOO) for satellite data assimilation, that translates satellite-retrieved 2D volcanic ash mass loadings to 3D concentrations at the top layer of the ash cloud. Finally, Chapter 8 summarizes the conclusions of this thesis, and the recommendations for further study.

2

The LOTOS-EUROS model and ensemble-based data assimilation

For forecasting the volcanic ash transport after eruption onset, a volcanic ash transport and diffusion model (VATDM) is needed.

The VATDM is run with Eruption Source Parameters (ESP) such as plume height and mass eruption rate as input, and with a data assimilation technique to continuously improve the initial conditions of the forecast.

In this chapter, the LOTOS-EUROS model that is used to simulate volcanic ash transport is described.

The methodology of ensemble-based data assimilation, such as the ensemble Kalman filter (EnKF) and the ensemble square root filter (EnSR), is also specified in this chapter.

Parts of this chapter have been published in:
(Fu *et al.*, 2015): *Assimilating aircraft-based measurements to improve Forecast Accuracy of Volcanic Ash Transport*, **Atmospheric Environment**, 115, 170-184. doi:*10.1016/j.atmosenv.2015.05.061*.

2.1. The LOTOS-EUROS model

To simulate a volcanic ash plume, an atmospheric transport model is needed. In this thesis, the LOTOS-EUROS (abbreviation of LOng Term Ozone Simulation – EUropean Operational Smog) model is used (Schaap *et al.*, 2008) with model version 1.10 (*http://www.lotos-euros.nl/*). This model is an operational air-quality model, used for daily air quality forecasts over Europe (Curier *et al.*, 2012), focusing on ozone, nitrogen oxides, and particular matter. In addition, it could be configured for the other regions of the world. The model uses an off-line approach and is driven by meteorological data produced by European Centre for Medium-Range Weather Forecasts (ECMWF). Among the variables of ECMWF model fields, the most important fields for volcanic ash modeling are the wind vectors (the "forecast" wind in an operational sense, not "analysis") since these describe the transport.

2.1.1. Domain

For the study of Eyjafjallajökull event, the model is configured on a domain from 45° to 70° North and 30° West to 15° East covering Iceland and North Europe (Figure 2.1). The grid resolution is 0.25° longitude × 0.125° latitude, approximately 12 × 12 km. In the vertical direction, the model version used has 18 vertical layers. On top of a surface layer of 25 m, three dynamic layers are present, where the lowest dynamic layer represents the variable mixing layer with the height obtained from the meteorological input, and the upper two dynamic layers are reservoir layers with equal thickness; the top of the dynamic layers is set to 3.5 km. The remaining 14 layers have fixed altitudes with equal thickness of 1 km, which set the top to 17.5 km in total.

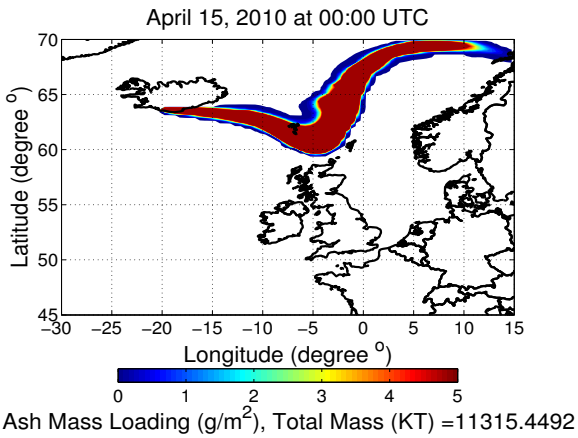

Figure 2.1: LOTOS-EUROS simulation for Eyjafjallajökull volcano eruption plume.

2.1.2. Tracers

The LOTOS-EUROS model is used in a tracer mode to produce volcanic ash simulations in a timely and useful manner for forecasting. In this thesis, we choose the

2010 Eyjafjallajökull volcano eruption plume as the study case. The tracers used in LOTOS-EUROS to simulate the ash plume are defined in the type S2 as defined by Mastin *et al.* (2009), in which the mass fraction of erupted debris finer than 63 μm is 0.4. The distributions of the coarse ash bines (ash_1 to ash_2) and the fine ash bines (ash_3 to ash_6) are provided in Table 2.1, which is defined based on the analysis of Durant and Rose (2009). According to Table 2.1, the volcanic ash concentrations are described by 6 aerosol tracers (ash_1 to ash_6) to model the plume transport.

Table 2.1: Volcanic Ash Particle Size Distribution and ash bins property for LOTOS-EUROS model simulation.

Bins	Particle Diameter	Percent of Mass	Average Particle Size (μm)
ash_1	250 to 2000 μm	29	1125.00
ash_2	63 to 250 μm	31	156.50
ash_3	30 to 63 μm	12	46.50
ash_4	10 to 30 μm	18	20.00
ash_5	2.5 to 10 μm	8	6.25
ash_6	0.0 to 2.5 μm	2	1.25

The volcanic ash concentration is described by 6 aerosol tracers as mentioned above. The physical processes that are relevant for volcanic ash are similar as those that apply for mineral dust, e.g., advective transport and diffusion, deposition, coagulation, sedimentation, and resuspension (Langmann, 2013). Where the transport is determined by the wind fields that could be regarded as rather well known, the other processes deposition and sedimentation processes are rather uncertain. The parameterizations for the later processes involve assumptions on the particle shape for example, which is difficult to summarize in a few numbers. These processes act on the distribution of the total ash mass over the modes (particle sizes) and the total mass load; one could therefore state that almost everything in the description of an ash cloud is uncertain, except for its shape and position. The processes included in this thesis are transport, sedimentation, and wet- and dry-deposition. The relevant properties for ash particles such as average particle size are listed in Table 2.1. Deposition and sedimentation are implemented following Zhang (2001). Processes that are missing yet are for example coagulation, and resuspension, which might be considered in future when appropriate observations are available to constrain them, for example sedimentation amounts.

2.1.3. Continuity equation

The model simulation on the domain is based on a discretization of the advection diffusion equation:

$$\frac{\partial \mathbf{c}_s}{\partial t} = -\nabla \cdot (\mathbf{u} \cdot \mathbf{c}_s) + \frac{\partial}{\partial \mathbf{v}} \left(\boldsymbol{\mu}_\mathbf{v} \frac{\partial \mathbf{c}_s}{\partial \mathbf{v}} \right) + \mathbf{E}_s - \mathbf{S}(\mathbf{c}_s) \tag{2.1}$$

where $\mathbf{c}_s$ (the subscript "s" refers to the number of species) is the concentration field of the volcanic ash bins (Table 2.1), $\mathbf{u}$ (U, V, W) is the velocity field in three

dimensions and U, V and W are the large scale wind components in respectively West to East, South to North and vertical direction. In LOTOS-EUROS, U and V are directly read from ECMWF wind field, while W are further calculated according to the mass conservation law of incompressible fluids. $\boldsymbol{\mu}_{\mathbf{v}}$ represents the vertical diffusion coefficient, which is defined using stability theory based on the meteorological input.

The advection part of Eq. (2.1) can be represented by $\mathbf{A} = -\nabla \cdot (\mathbf{u} \cdot \mathbf{c}_s)$, while the diffusion part $\mathbf{F} = \frac{\partial}{\partial \mathbf{v}} \left(\boldsymbol{\mu}_{\mathbf{v}} \frac{\partial \mathbf{c}_s}{\partial \mathbf{v}} \right)$.

$\mathbf{S}$ accounts for sink processes including deposition and sedimentation. The eruption source term $\mathbf{E}$ represents emissions. The sink processes are the same as for the other aerosols following Zhang (2001). The emission is discussed below in Section 2.1.4.

Eq. (2.1) can be described as a state-space form:

$$\mathbf{x}(k) = M_{k-1}(\mathbf{x}(k-1)) \tag{2.2}$$

Here in this thesis, state vector $\mathbf{x}$ represents concentration vector $\mathbf{c}$ and the state space operator of the LOTOS-EUROS model is denoted by M_{k-1}. This operator computes the concentration vector $\mathbf{c}$, which contains all considered components for all grid cells, at time t_k given the concentrations at time t_{k-1}.

2.1.4. Emissions

To describe a volcanic eruption in the LOTOS-EUROS model, Eruption Source Parameters (ESP) such as Plume Height (PH), Mass Eruption Rate (MER) and Vertical Mass Distribution (VMD) are needed. In (Mastin *et al.*, 2009) ESPs for different volcanoes are provided as a look up table. These ESPs could be used in a transport model to simulate the ash plume. In this thesis, the LOTOS-EUROS model with volcanic ash configuration has been used to simulate the April–May 2010 period of activity from Eyjafjallajökull.

An important ESP is the Plume Height (PH). For the 2010 Eyjafjallajökull eruption, the input parameter PH is taken from the real-time referred from hourly based Icelandic Meteorological Office (IMO) plume height detection (every 5 minutes, see Fig. 2.2) by Icelandic Meteorological Office (IMO) (Gudmundsson *et al.*, 2012; Webley *et al.*, 2012). Usually the uncertainty of PH is taken as 20 % (Bonadonna and Costa, 2013).

For the Vertical Mass Distribution (VMD), large explosive volcanic plumes have a typical 'umbrella' shaped vertical distribution (Sparks *et al.*, 1997) and as such this 'umbrella' shaped VMD is adapted into LOTOS-EUROS in this chapter, see Fig. 2.3.

Another input parameter Mass Eruption Rate (MER) is usually very hard to measure for an explosive erupting volcano. Usually it is calculated from the plume height. Mastin *et al.* (2009) did some studies on the parameter relationship and concluded that an empirical relationship between MER (kg s^{-1}) and PH (km):

$$\mathrm{PH} = 2.00\mathrm{V}^{0.241}, \quad and \quad \frac{\mathrm{MER}}{\mathrm{V}} = \frac{4.0e^6}{1.5e^3}. \tag{2.3}$$

where V (m^3 s^{-1}) represents the volumetric flow rate. Mastin *et al.* (2009) estimated the uncertainty of MER through this calculation is about 50%.

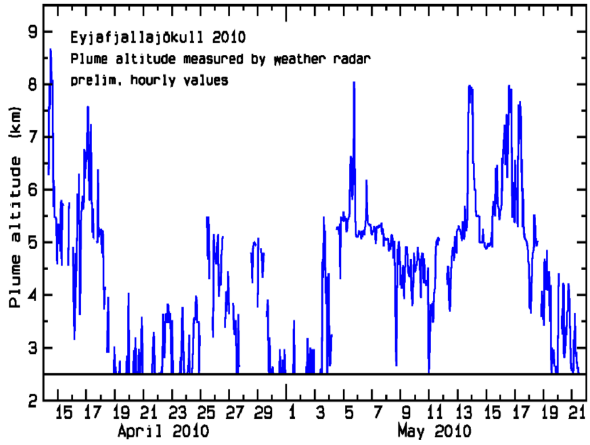

Figure 2.2: Icelandic Meteorological Office [IMO] plume height detection from April to May, 2010. Courtesy from IMO on-line database.

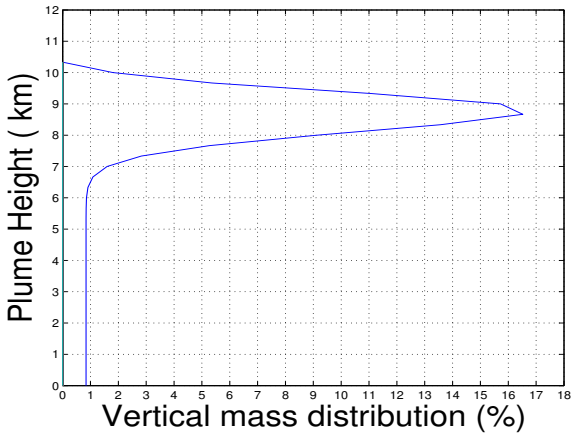

Figure 2.3: The 'umbrella' vertical mass distribution (VMD) of ash cloud in LOTOS-EUROS. Shown in this case is the vertical profile of an eruption with 10 km plume height.

2.2. Ensemble-based data assimilation methodology

To be able to provide an accurate forecast of volcanic ash transport, here we use ensemble-based data assimilation to combine the model and the measurements together. The detailed motivations and methodologies are specified below.

2.2.1. Motivations for using data assimilation

The motivations for using data assimilation is two-fold.

(i) The meteorological wind fields and estimates of Eruption Source Parameters (Mastin *et al.*, 2009) (ESPs) are needed as input to the VATDM model. A VATDM uses physical parameterizations of source and removal processes that affect the concentrations in the dispersing volcanic cloud. Aggregation of ash particles and subsequent enhanced removal is an extremely important process for estimating the atmospheric ash burden (Durant *et al.*, 2010), yet this process is not included in most dispersion models because of its complexity and the demand on computation time (Folch *et al.*, 2010). Without accurate knowledge of the temporal variation of the mass eruption rate at the volcano and particle removal rate in the atmosphere, it is not possible to provide accurate quantitative forecasts of the ash concentrations arriving in the airspace over a long distance (Prata and Prata, 2012). Data assimilation is needed to provide this knowledge.

Table 2.2: Comparison of Total Mass in KT (10^6 kg) between the LOTOS-EUROS model and the WRF-Chem model simulation of eruption of Eyjafjallajökull volcano in 2010.

Time	LOTOS-EUROS	WRF-Chem
00:00 (UTC) 15 April	11315.45	10648.4
00:00 (UTC) 17 April	5738.63	6729.2

(ii) Based on the ESPs described in Section 2.1.4, detailed validation with the LOTOS-EUROS model has been made in (Fu *et al.*, 2015), which evaluates that the LOTOS-EUROS model is capable of modeling volcanic ash transport problem. Table 2.2 implies that different VATDMs will provide different forecast values because different models have different details, therefore only relying on VATDM to make forecast is not sufficient, that is also another motivation in this thesis for using assimilation to correct the LOTOS-EUROS simulation to improve the forecast accuracy.

2.2.2. Motivations for using ensemble-based data assimilation

Ensemble-based data assimilation, which refers to the sequential use of the direct measurements to create accurate initial conditions for model runs (Zehner, 2010), is one of the most commonly used approaches for real-time forecasting problems

(Evensen, 2009). In each assimilation step, a forecast from the previous model simulation is used as a first guess, using the available observation this forecast is modified in better agreement with these observations.

Thus, for the application of volcanic ash transport, ensemble-based data assimilation (Evensen, 1994, 2003) can be used to compensate for the problems of employing inaccurate ESPs by continuously assimilating in situ observations to estimate volcanic ash concentrations.

This explains why ensemble-based data assimilation is useful, and the detailed methodology is discussed below.

The ensemble Kalman filter (EnKF) (Evensen, 1994) and the ensemble square root filter (EnSR) (Evensen, 2004), as two main ensemble-based data assimilation methods (Evensen, 2009), are used in this thesis to investigate the potential improvements on volcanic ash state by continuously assimilating aircraft-based or satellite-based measurements. Apart from EnKF and EnSR, other variants have been introduced such as the ensemble Kalman smoother (EnKS) (Evensen and van Leeuwen, 2000), and the reduced rank square root filter (RRSQRT) (Verlaan and Heemink, 1997). Ensemble-based assimilation is easy to implement, suitable for real-time estimation of concentrations and has a very general statistical formulation.

The ensemble Kalman filter technique (EnKF), as the most known ensemble-based data assimilation technique, is used to assimilate aircraft in situ measurements from Chapter 3 to Chapter 6. In addition, EnKF is chosen because it can be easily combined with covariance localization (Hamill *et al.*, 2001). An accurate covariance localization is essential to reduce spurious covariances during assimilating the less but accurate aircraft measurements. In Chapter 7 the ensemble square root filter (EnSR), in most applications a more efficient method (Evensen, 2004) than EnKF, is employed to assimilate the satellite-extracted in situ measurements.

2.2.3. The ensemble Kalman filter (EnKF)

EnKF essentially is a Monte Carlo ensemble-based method (Evensen, 2003), based on the representation of the probability density of the state estimate in an ensemble of N states, $\boldsymbol{\xi}_1, \boldsymbol{\xi}_2, \cdots, \boldsymbol{\xi}_N$. Each ensemble member is assumed to be a single sample out of a distribution of the true state. The number of required ensemble members depends on the complexity of the probability density function to be captured, which is usually determined by the nonlinearity of the model and the description of the involved uncertainties.

For volcanic ash assimilation, an ensemble size of 50 is considered acceptable in terms of accuracy while keeping computation time within reach (see Chapter 3). For application of the filter algorithm to the LOTOS-EUROS model, in the first step of this algorithm an ensemble of N volcanic ash states $\boldsymbol{\xi}^a(0)$ is generated to represent the uncertainty in the initial condition $\mathbf{x}(0)$. In the second step, the forecast step, the LOTOS-EUROS model (with stochastic plume height) propagates the ensemble members from the time $k-1$ to k, as defined in Eq. (2.4):

$$\boldsymbol{\xi}_j^f(k) = M_{k-1}(\boldsymbol{\xi}_j^a(k-1)). \tag{2.4}$$

The state-space operator M_{k-1} describes the time evolution from the time $k-1$ to k of the state vector which contains the ash concentrations in the model grid boxes. The filter state is a stochastic distribution with mean $\mathbf{x}^f$ and covariance $\mathbf{P}^f$ following:

$$\mathbf{x}^f(k) = [\sum_{j=1}^{N} \boldsymbol{\xi}_j^f(k)]/N, \tag{2.5}$$

$$\mathbf{L}^f(k) = [\boldsymbol{\xi}_1^f(k) - \mathbf{x}^f(k), \cdots, \boldsymbol{\xi}_q^f(k) - \mathbf{x}^f(k)], \tag{2.6}$$

$$\mathbf{P}^f(k) = [\mathbf{L}^f(k)\mathbf{L}^f(k)^T]/(N-1), \tag{2.7}$$

where the superscript "^{T}" represents the transpose of the matrix. In this thesis, the forecast step is performed in parallel because of the natural/common parallelism of the independent ensemble propagation, which is a trivial approach when employing ensemble-based data assimilation (Liang *et al.*, 2009; Tavakoli *et al.*, 2013; Khairullah *et al.*, 2013).

The observational network is defined by the observation operator H that maps state vector $\mathbf{x}$ to observation space $\mathbf{y}$:

$$\mathbf{y}(k) = H_k(\mathbf{x}(k)) + \mathbf{v}(k), \quad \mathbf{v}(k) \sim N(0, \mathbf{R}), \tag{2.8}$$

where the observation error $\mathbf{v}$ is drawn from a Gaussian distribution with zero mean and covariance matrix $\mathbf{R}$. Here, $\mathbf{y}$ contains measurements of ash concentration and $\mathbf{R}$ is filled in a diagonal matrix with the square of the standard deviation of y. The operator H_k then selects the grid cell in $\mathbf{x}$ that corresponds to the observation location. When measurements become available, the ensemble members are updated in the analysis step using the Kalman gain:

$$\mathbf{K}(k) = (\mathbf{f} \circ \mathbf{P}^f(k))\mathbf{H}(k)^T[\mathbf{H}(k)(\mathbf{f} \circ \mathbf{P}^f(k))\mathbf{H}(k)^T + \mathbf{R}]^{-1}, \tag{2.9}$$

$$\boldsymbol{\xi}_j^a(k) = \boldsymbol{\xi}_j^f(k) + \mathbf{K}(k)[\mathbf{y}(k) - \mathbf{H}(k)\boldsymbol{\xi}_j^f(k) + \mathbf{v}_j(k)], \tag{2.10}$$

$$\mathbf{P}^a = (\mathbf{I} - \mathbf{KH})\mathbf{P}^f, \tag{2.11}$$

where $\mathbf{v}_j$ represents realizations of the observation error v.

In Eq. (2.9), the covariance localization (Houtekamer and Mitchell, 1998, 2001) is obtained using a Schur product $\mathbf{f} \circ \mathbf{P}^f$ (i.e., element-wise multiplication) in order to reduce the spurious covariances caused by the finite ensemble size, which is a general problem in ensemble-based data assimilation. The localization matrix $\mathbf{f}$ is obtained by applying a localization function to the Euclidean distance between two points. The covariances decrease to zero beyond a certain distance. This distance-based covariance localization can easily be implemented for eliminating the spurious covariances outside the localized region. For some applications (e.g., ozone, CO_2, sulfur dioxide), this approach has achieved an acceptable performance with a simple setup using a constant localization parameter of 50–500 km (Curier *et al.*, 2012; Chatterjee *et al.*, 2012; Barbu *et al.*, 2009).

2.2.4. The ensemble square root filter (EnSR)

To reduce the sampling errors introduced by adding random numbers $\mathbf{v}_j$ to the observations, the analysis step can be written in a square root form (Evensen, 2004; Sakov and Oke, 2008a,b). Using the notations $\mathbf{Y} = \mathbf{H}\mathbf{L}^f$ and $\mathbf{S} = \mathbf{Y}\mathbf{Y}'$, the updated covariance matrix becomes:

$$\mathbf{P}^a = \mathbf{L}^a(\mathbf{L}^a)' = \mathbf{L}^f(\mathbf{I} - \mathbf{Y}'\mathbf{S}^{-1}\mathbf{Y})(\mathbf{L}^f)' = \mathbf{L}^f\mathbf{T}\mathbf{T}'(\mathbf{L}^f)' \quad , \tag{2.12}$$

thus $\mathbf{L}^a$ can be represented by

$$\mathbf{L}^a = \mathbf{L}^f\mathbf{T} \quad , \tag{2.13}$$

where $\mathbf{T}$ is an $N \times N$ matrix which satisfies: $\mathbf{T}\mathbf{T}' = \mathbf{I} - \mathbf{Y}'\mathbf{S}^{-1}\mathbf{Y}$. It can easily be shown that there is a unique symmetric positive definite solution defined as the square root of the symmetric positive definite matrix: $\mathbf{T}^s = [\mathbf{I} - \mathbf{Y}'\mathbf{S}^{-1}\mathbf{Y}]^{\frac{1}{2}}$. By using the eigenvalue decomposition, the matrix $\mathbf{T}^s$ has the following form:

$$\mathbf{T}^s = \mathbf{C}\mathbf{\Lambda}^{\frac{1}{2}}\mathbf{C}', \tag{2.14}$$

where $\mathbf{T}^s$ is referred as the symmetric factor. The symmetric algorithm defined above introduces the smallest analysis increments for an arbitrary compatible norm. The good performance of EnSR has been obtained on improving the forecast accuracies without introducing additional sampling errors (Evensen, 2004; Sakov and Oke, 2008a).

2.2.5. Framework

In this thesis, OpenDA (Open Data Assimilation, *www.openda.org*) software (van Velzen and Verlaan, 2007) is used to implement EnKF/EnSR combining LOTOS-EUROS model running with the aircraft/satellite measurements. The framework is shown in Fig. 2.4. The reason why we choose it is because: (1) OpenDA is an open interface standard for a set of tools, filters, and numerical techniques to quickly implement data assimilation. (2) A model that conforms to the OpenDA standard can use all the tools that are available in OpenDA. This allows experimentation with data-assimilation methods without the need for extensive programming.(3) OpenDA has been designed for high performance. Hence, even large-scale models can use it. Thus for practical EnKF/EnSR implementation with lare-scale LOTOS-EUROS model (van Velzen and Segers, 2010), OpenDA is powerful but not difficult to be used and can quickly implement data assimilation method.

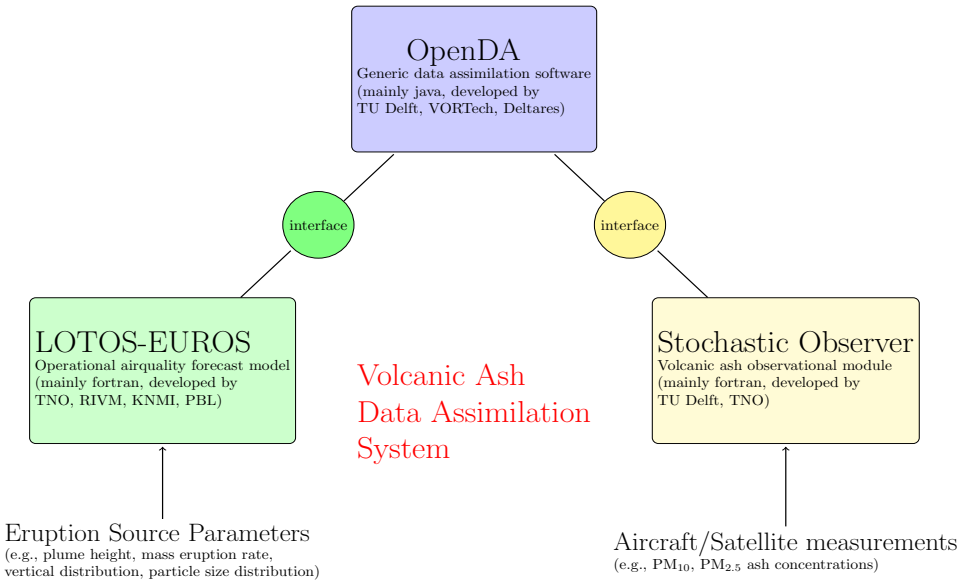

Figure 2.4: The ensemble-based data assimilation framework

3

Assimilating aircraft-based measurements to improve forecast accuracy of volcanic ash transport

Reliable and accurate ash measurements are crucial for providing a successful ash clouds advice. In this chapter, simulated aircraft-based measurements, as one type of volcanic ash measurements, will be assimilated into a transport model to identify the potential benefit of this kind of observations in an assimilation system.

The results show assimilating aircraft-based measurements can significantly improve the state of ash clouds, and further providing an improved forecast as aviation advice. We also show that for advice of aeroplane flying level, aircraft-based measurements should be preferably taken from this level to obtain the best performance on it. Furthermore it is shown that in order to make an acceptable advice for aviation decision makers, accurate knowledge about uncertainties of ESPs and measurements is of great importance.

Parts of this chapter have been published in:
(Fu *et al.*, 2015): *Assimilating aircraft-based measurements to improve Forecast Accuracy of Volcanic Ash Transport*, **Atmospheric Environment**, 115, 170-184. doi:*10.1016/j.atmosenv.2015.05.061*.

3.1. Introduction

For the purpose of using a data assimilation system to improve the initial conditions of the the ash load, the volcanic ash measurements must be available near-real-time. Flemming and Inness (2013) assimilated for example satellite retrievals in a four-dimensional variation (4D-var) approach. Besides satellite observations of volcanic ashes, many other different scientific measurement campaigns were performed in order to get information about the ash plume, such as using lidars, ceilometers, balloon sondes etc. Among these, also aircraft-based measurements were obtained close to the eruption plume, which are probably the most direct observations possible. In this chapter, the potential benefit of these kind of observations in an assimilation system is studied. The experiments consist of so-called twin-experiments, where observations are simulated from model simulations and fed into an assimilation system using the same model. In this setup it is a first step towards assimilation of real observations, to obtain a first idea on how to use this kind of observations and what their impact is in an assimilation system.

For employment of ensemble-based data assimilation, in situ measurements are the optimal type of observations (Evensen, 2009). Although satellite measurements are considered as the most commonly used volcanic ash observations based on their large detection domain and long-time continuous output data, they are not directly suited for data assimilation systems. This is because satellite observations are often not direct measurements of the quantity of interest, but optical property measurements. Therefore the aerosol quantity needs to be derived by a retrieval process or a complex observation operator. Moreover, satellite data are often two-dimensional (2D), and thus lack sufficient vertical resolution (Bocquet *et al.*, 2015). Note that, some satellites can provide very detailed vertical information on plumes (e.g., Cloud-Aerosol Lidar with Orthogonal Polarization (CALIOP) lidar measurements) but are spatially sparse (Winker *et al.*, 2012). Fortunately, the in situ volcanic ash state variables can be directly and accurately measured nowadays by means of airborne observations of volcanic ash (Weber *et al.*, 2012). These aircraft-based measurements can be obtained in the boundaries of volcanic ash plume, which are probably the most direct volcanic ash observations possible.

Currently aircraft-based measurements are only used for validation purpose of volcanic ash clouds (Weber *et al.*, 2012), not yet involved in data assimilation systems. This chapter will study the use of aircraft-based measurements in data assimilation with an ensemble Kalman filter (EnKF) algorithm. This chapter aims at (1) investigating the performance of aircraft-based measurements in data assimilation systems; (2) study the impact of measurements from different flight altitudes on forecasts at aviation level; (3) discuss the influence of uncertainties in the ESPs and measurements.

This chapter is organized as follows. Section 3.2 gives an introduction of the aircraft-based measurements used in our assimilation experiments. Section 3.3 contains the assimilation results and the discussion on the results. Finally, the last section summarizes the concluding remarks of our research.

3.2. Aircraft-based measurements

3.2.1. Measurement description

During the period of eruption of the Icelandic volcano Eyjafjallajökull, a large number of different scientific measurement campaigns were performed to gather information about the nature and occurrence of the ash plume. The measurements comprised for example LIDAR measurements (Pappalardo *et al.*, 2010; Tesche *et al.*, 2010; Groß *et al.*, 2010; Miffre *et al.*, 2010; Flentje *et al.*, 2010), satellite observations (Stohl *et al.*, 2011), groundbased in situ measurements (Schäfer *et al.*, 2010; Emeis *et al.*, 2011), as well as balloon (Flentje *et al.*, 2010) and aircraft based measurements (Weber *et al.*, 2010; Schumann *et al.*, 2011; Bukowiecki *et al.*, 2011; Eliasson *et al.*, 2011; Lolli *et al.*, 2010). Aircraft-based measurements are of special interest, because they allow sampling of the ash plume with a high temporal and spatial resolution. Another beneficial aspect of aircraft measurements is that they are more flexible than other type measurements, because usually the aircraft is operated as a "state aircraft" enabling operations in otherwise closed air space where the pilots are able to change the flight plan in-flight in direct contact with air traffic control or wisely decide to follow the downwind ash trend to obtain the best observations.

During the period of that eruption, the outskirts of the eruption plume were entered directly by research flights (Fig. 3.1(a)), delivering most direct measurements within the eruption plume during this eruptive event. All of the measurement flights were equipped with optical particle counters for in situ measurements. Real-time monitoring of the particle concentrations was possible during the flights and in situ measurements from the eruption plume were obtained with high time- and spatial-resolution. It has been proven that by entering the outskirts of the plume directly the research aircraft can detect ash concentrations of up to 2000 μg m^{-3} (Weber *et al.*, 2012). That used to be considered as the highest concentration an aircraft can endure at that time, because areas with ash concentration higher than 2000 μg m^{-3} were classified as No Fly Zone (NFZ) (Zehner, 2010), which means the aircraft flying in these areas can crash. However, recently 2000-4000 μg m^{-3} is classified as medium level concentration (EASA, 2015). Many airlines are certified to operate in this regime based on the application of Safety Risk Assessment. Therefore now the highest concentration an aircraft can endure is updated to be 4000 μg m^{-3} instead of 2000 μg m^{-3}.

Optical particle counters (OPC) were used for in situ ash concentration measurements. The principle of OPC's can be summarized as follows: Ash contaminated air is pumped through the OPC where the particles cross a continuous laser beam. Every single particle causes a scattering/diffraction of the laser beam. This is recorded by a detector that counts the particles, see Fig. 3.1(b). Moreover, scattering/diffraction intensity of the laser beam is a measure for the size of the particles. From that, the mass can be calculated, provided the density of the particles is known. A mean mass density of 2.65 gcm^{-3} (Heim *et al.*, 2008) for the coarse mode ash particles is recommended to use by European Facility for Airborne Research (EUFAR) for Eyjafjallajökull volcano ash.

In this chapter, the most interesting thing is how accurate OPC's measurements

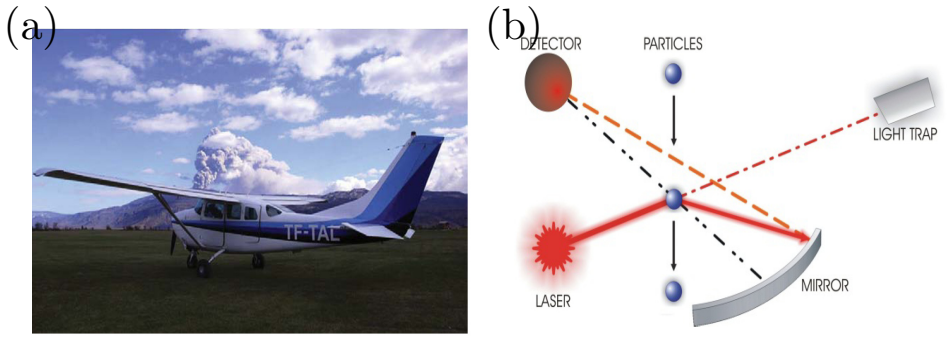

Figure 3.1: (a) Example of aircrafts used for volcanic ash measurements and (b) optical particle counter OPC equipped on aircrafts. Courtecy from (Weber *et al.*, 2012) and (Weber *et al.*, 2010), respectively.

are, because the knowledge of uncertainties is crucial for a successful data assimilation. Through a direct laboratory calibration experiment, in which the mass concentration obtained with the OPC was compared with the absolute mass concentration gathered on a gravimetric filter, the deviation between the gravimetric measurement and the OPC was about 10% (Weber *et al.*, 2010) which can be taken as the instrumental error for this type of measurements in well calibrated cases.

3.2.2. Model representation error

For assimilation of measurements with a simulation model, it is necessary to quantify the model representation error. The model representation error is the difference between the quantity that instrument tries to observe, and what the model could represent in terms of its state. This does not include instrumental errors as defined above, or model deficiencies such as inaccurate input parameters, but only the difference due the model being defined on a discrete grid with finite resolution and simulations valid for discrete time steps.

The spatial resolution of the model used in this chapter is around 25 km $\times$ 25 km $\times$ 1 km, therefore the volume of one grid-box is about 625 km^3. Through model processing, the concentration of one grid-box represents an average value for this grid-box, while one aircraft-based measurement is a sample (a point value) in a 3 dimensional field. In this chapter, we choose the in situ measurement corresponding to the grid-box average value. This approximation makes sense only when two assimilated measurements are positioned in two different grid-boxes. This requires that the assimilation frequency is not too high, so that the measurements used in two sequential assimilation steps are in different grid-boxes. Moreover, the assimilation frequency should also not be too low because a measuring aircraft usually can work in the sky for less than 10 hours continuously (Weber *et al.*, 2012; Schumann *et al.*, 2011). If an hourly assimilation frequency is chosen, then along the whole route, only less than 10 measurements will be used, which is a waste for other continuous measurements. Therefore based on the analysis above and also considering the aircraft speed of 100-200 km/h (Weber *et al.*, 2012) and the

LOTOS-EUROS horizontal resolution, a 15 minutes assimilation frequency is chosen in this chapter. Within 15 minutes, the aircraft can fly over about 2 grid-boxes in the model, which guarantees different assimilated measurements are in different grid-boxes. The model time step cannot be over the assimilation time step, hence in this chapter, 15 minutes is also chosen to be one model time step, without loss of generality. Note that if the research aircraft is faster or the horizontal resolution is higher, the assimilation frequency can be chosen smaller than 15 minutes (e.g., 10 or 5 minutes which can be considered sufficient).

Through the settings defined above, the observation almost corresponds to one model state in a grid-box, which means the representation error of the model is probably small. For the moment we will there not explicitly specify a model representation error, but implicitly assume that it is zero. Therefore, the total observation representation error, defined as the sum of the instrumental error and the model representation error, is taken as 10% in this chapter.

Since the knowledge about the uncertainties and representation errors of aircraft measurements are known, data assimilation can now be used to combine observations with the model to get an improved estimate of the ash load.

3.3. Assimilation results and discussions

3.3.1. Experimental setup

The EnKF is applied to the stochastic version of LOTOS-EUROS. The chapter comprises experiments with different settings for the uncertainty in parameters such as plume height (PH), mass eruption rate (MER), particle size distribution (PSD) and vertical mass distribution (VMD). In this chapter, the uncertainty of PH and MER are taken as 20 % and 50 %, respectively (see Section 2.1.4). The stochastic version of the model is built by considering these two uncertain parameters. The temporal correlation for a uncertain model parameter defines how the value at current time is related to that at prior time. However, due to volcano inner fierce and fast physical processes, the PH and MER could change very fast, and therefore taking temporal correlation into account is not necessary and realistic. Therefore, in this chapter, we consider PH and MER as temporal uncorrelated. Aircraft-based measurements are used in the analysis step of the EnKF algorithm; the uncertainty in the measurements has been investigated as a fixed standard deviation of 10 %, see Section 3.2. This chapter focuses on studying how aircraft-based measurement performs well in a data assimilation system, thus it is not necessary to use real measurements. Therefore, the measurements in this chapter are designed based on the real aircraft-based measuring campaigns (Weber *et al.*, 2012). In these campaigns, concentrations of ash with diameter 0 to 2.5 and 2.5 to 10 μm were observed, which from Table 2.1 respectively corresponds to ash_5 and ash_6 in this chapter.

From (Weber *et al.*, 2012; Schumann *et al.*, 2011), a measuring aircraft can work in the sky for less than 10 hours continuously, so based on this condition, a 10 hour aircraft measurement experiment is designed. Note that in reality usually an aircraft measurement mission is 4 to 6 hours, 10 hours is not very realistic,

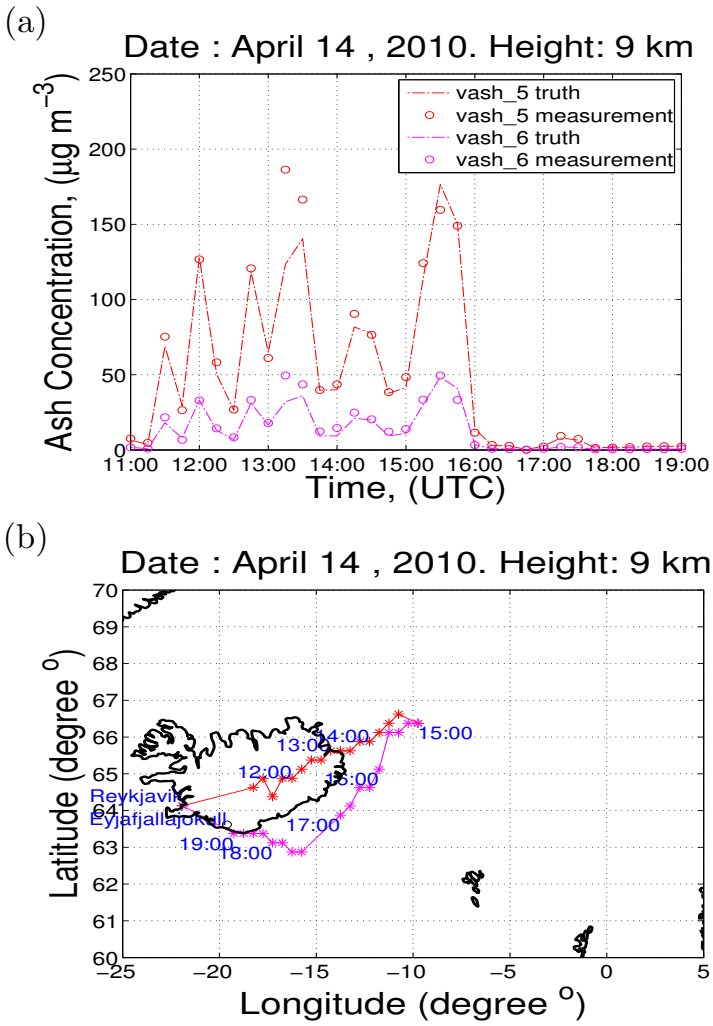

Figure 3.2: (a) Aircraft-based Measurements for ash_5 and ash_6. (b) is the designed route at 9 km where the measuring aircraft enters the outskirts of ash plume, red and magenta lines represent different flying directions to Reykjavik airport.

but we use the duration of 10 hours in our twin experiments to evaluate effect of assimilation over a longer time. The height of interest in this chapter is 9 km as mentioned in Section 3.1. The flight routes are chosen at an altitude of 9 km, 7 km, 5 km, 3 km separately to study which level measurements provide the best air traffic advisory for 9 km. The start time of Eyjafjallajökull eruption is set at 9:00 (UTC), 14 April 2010, and the aircraft-based measurements are designed to start at 11:00 (UTC), 14 April 2010. The whole assimilation time is from 11:00 to 19:00 (UTC), 14 April 2010. The flying route is designed as shown in Fig. 3.2(c) based on the fact that the measuring aircraft can enter the plume outskirt where the ash concentration is less than 4000 μg m^{-3} (see Section 3.2.1). During this period, measurements are taken every 15 minutes, see Fig. 3.2(a) and Fig. 3.2(b) taken at 9 km for example.

From the start time to aircraft returning time, the simulation parameters are set as introduced in Section 2.1. For evaluating the performance of assimilation, twin experiments are designed with the Truth obtained as one realization of the stochastic model by adding uncertainty 20 %, 50 % to PH, MER, separately. The measurements are obtained through combining the Truth values with 10 % uncertainty, see Fig. 3.2(a) and Fig. 3.2(b).

Table 3.1: Plume height and Eruption rate used in LOTOS-EUROS to generate the Truth for April 14-18, 2010.

Start Time – End Time	Height ASL (km)	Eruption Rate (kg/s)
4/14 09:00 – 4/14 11:00	8.8	5.23E+05
4/14 11:00 – 4/14 13:00	9.3	5.85E+05
4/14 13:00 – 4/14 15:00	7.8	3.98E+05
4/14 15:00 – 4/14 17:00	9.1	5.38E+05
4/14 17:00 – 4/14 19:00	8.5	4.41E+05
4/14 19:00 – 4/14 22:00	6.3	5.73E+04
4/14 22:00 – 4/15 01:00	4.8	3.13E+04
4/15 01:00 – 4/15 04:00	5.9	4.97E+04
4/15 04:00 – 4/15 17:00	5.0	5.07E+04
4/15 17:00 – 4/16 06:00	7.1	8.32E+04
4/16 06:00 – 4/16 19:00	6.8	8.15E+04
4/16 19:00 – 4/17 01:00	9.2	5.10E+05
4/17 01:00 – 4/17 07:00	8.0	3.12E+05
4/17 07:00 – 4/17 13:00	9.4	3.89E+05
4/17 13:00 – 4/17 19:00	7.9	2.97E+05
4/17 19:00 – 4/18 01:00	8.5	3.93E+05

The experiment procedure can be briefly summarized by stating that the model run starts at 09:00 (UTC), 14 April, 2010 by considering the first initial condition as zero. With the model propagating, the model result from previous time step is taken as the initial condition for the next time step. When the model run arrives at

11:00 (UTC), 14 April, the initial condition gets continuously modified by the data assimilation process through combining all the aircraft-based measurements until the time 19:00 (UTC), 14 April. Thus at this time, an analyzed state (which can be taken as an initial condition for next model run) combining all aircraft measurements of 8 hours can be obtained. Evaluation on this analyzed state will be given to invastigate the possible improvement compared to simulation without assimilation. In the remainder of the chapter, AnaSta and SimSta are used to denote the analyzed state (obtained with assimilation) and the simulation state (obtained without assimilation), respectively. Thus, $\text{AnaSta}_{19:00(14)}$ denotes AnaSta at 19:00 (UTC), 14 April, 2010 and will be further used to forecast over multiple days (typically one or two days according to NAME model forecast).

3.3.2. Assimilation experiments

Based on the setup above, an experiment is designed to test whether the analyzed state $\text{AnaSta}_{19:00(14)}$ is improved through an 8 hours continuous assimilation of aircraft-based measurements. For this experiment, the measuring aircraft flies at the 9 km height and the ensemble size is chosen to be 50 in the EnKF system. Before we show the result of $\text{AnaSta}_{19:00(14)}$, first how data assimilation continuously works in this system is explained using Fig. 3.3 and Fig. 3.4.

Fig. 3.3 is the result of specific measurements at one location on 12:00 (UTC), 14 April, 2010. At this time, we can see from Fig. 3.2, the measuring aircraft location is (11.75°W, 65.625°N, 9 km). In Fig. 3.3, the forecast of the ash concentrations at this location in each of the 50 ensemble members shown. The concentrations are distributed around the mean values (96.38 μg m^{-3} for ash_5, 24.80 μg m^{-3} for ash_6) indicated by the black circle. At this time, the measurements of the concentrations are (126.69 μg m^{-3}, 32.93 μg m^{-3}) which is significantly different from the forecast mean. Through assimilating these measurements at this time, analysis values of ash_5 and ash_6 are obtained as (123.61 μg m^{-3}, 32.54 μg m^{-3}) which are much closer to the truth (135.88 μg m^{-3}, 33.88 μg m^{-3}) than the forecast mean. This result illustrates that the assimilated state better approximates the truth than that without assimilation. Moreover, spread in the analysis ensemble is smaller than that of the forecast ensemble, that means the error variance of analysis value is reduced through assimilation.

Fig. 3.3 only shows the assimilation result at the measuring location, we cannot see the influence of the assimilation on the whole plume. It is not clear whether measurements from one location can influence the whole plume or not. Fig. 3.4 is used to answer this question. In Fig. 3.4, without loss of generality the time 16:30 (UTC), 14 April, 2010 is chosen to show the result for the whole plume at 9 km. $\text{Tru}_{16:30(14)}$ in Fig. 3.4 is the truth state, while $\text{FC}_{16:30(14)}$ is the forecast state and $\text{AnaSta}_{16:30(14)}$ is the analyzed state. By comparing $\text{FC}_{16:30(14)}$ with $\text{AnaSta}_{16:30(14)}$, we can see that with assimilating aircraft-based measurements at one location, the difference between them only appears in a local area (approximatly the red ellipse in Fig. 3.4) around the measuring location, while the results outside this local area are hardly changed. This means that the assimilation process doesn't influence the entire plume, but only a local area around the measuring aircraft

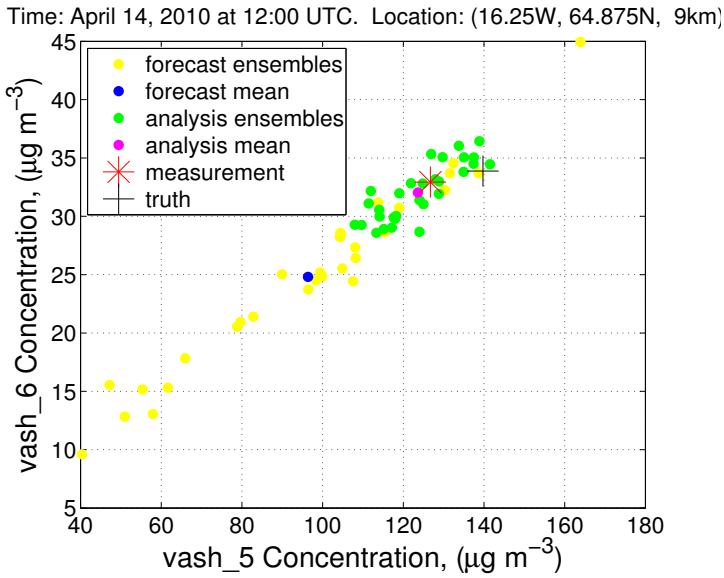

Figure 3.3: Assimilation at one location.

location. Note that this is achieved without explicit enforcing of localization as for example in (Houtekamer and Mitchell, 1998). In the chosen setup without temporal correlation (see Section 3.3.1), the ensembles consist of patterns that arise from uncertainties during a single time step. The spatial impact of observations from a single location is therefore bounded to an area where ashes present have been emitted during a short period. Moreover, in this local area, $\text{AnaSta}_{16:30(14)}$ is much closer to $\text{Tru}_{16:30(14)}$ than $\text{FC}_{16:30(14)}$. This shows that through each assimilation, the state within a local area is improved. Therefore with a continuously assimilation using aircraft-based measurements of changing locations, the states in a large area around the measuring flight route will be improved, as shown in Fig. 3.2(c).

Next, the experiment result of $\text{AnaSta}_{19:00(14)}$ is shown in Fig. 3.5. $\text{Tru}_{19:00(14)}$ is the Truth at 19:00 (UTC), 14 April, 2010 which is implemented based on Table 3.1. $\text{SimSta}_{19:00(14)}$ is the simulation result without assimilating aircraft-based measurements. $\text{AnaSta}_{19:00(14)}$ is the assimilation result at this time with assimilating aircraft-based measurements (detailed settings are in Section 3.3.1). Big differences can be observed between Fig. 3.5(a) and Fig. 3.5(b). The difference is caused by implementing with different PH and MER. In reality, $\text{Tru}_{19:00(14)}$ is unknown, thus $\text{SimSta}_{19:00(14)}$ is used as the initial condition for the forecast over multiple days. $\text{AnaSta}_{19:00(14)}$ is that with continuously assimilating aircraft-based measurements. Comparing $\text{AnaSta}_{19:00(14)}$ and $\text{SimSta}_{19:00(14)}$, we can see both of them overestimate the truth, but $\text{AnaSta}_{19:00(14)}$ is much closer to $\text{Tru}_{19:00(14)}$ and the overestimation is much lower than $\text{SimSta}_{19:00(14)}$. This means the state after assimilating aircraft-based measurements is much more accurate than that without assimilation.

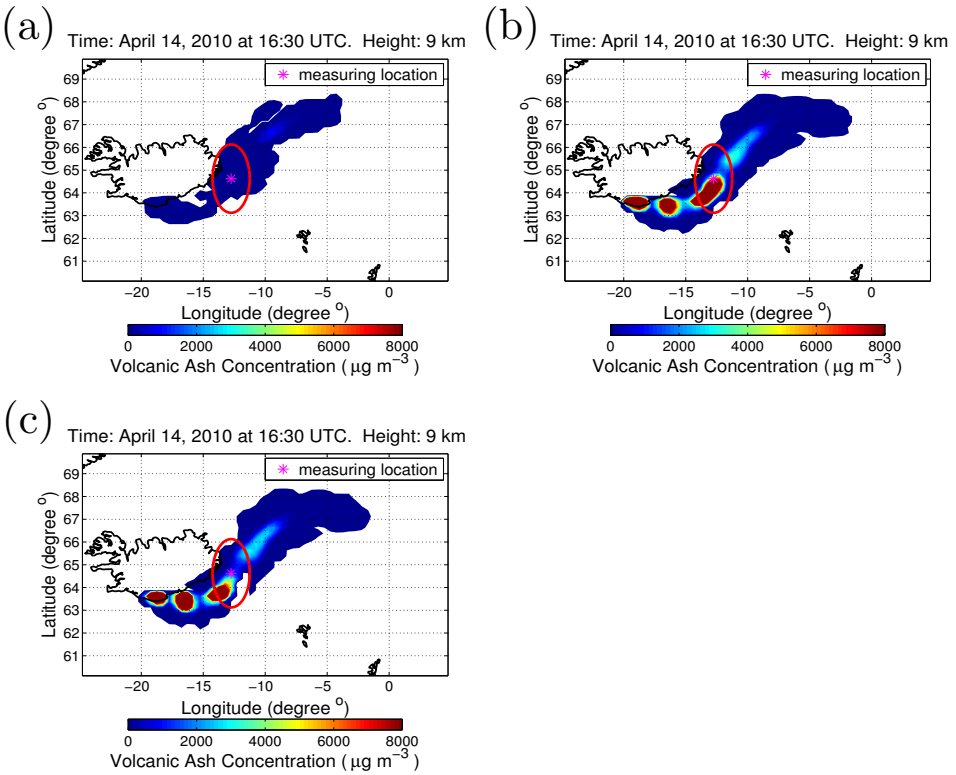

Figure 3.4: Assimilation results during continuously assimilation (red ellipse represents a local area where the assimilation can influence). (a) $\mathrm{Tru}_{16:30(14)}$, (b) $\mathrm{FC}_{16:30(14)}$ and (c) $\mathrm{AnaSta}_{16:30(14)}$.

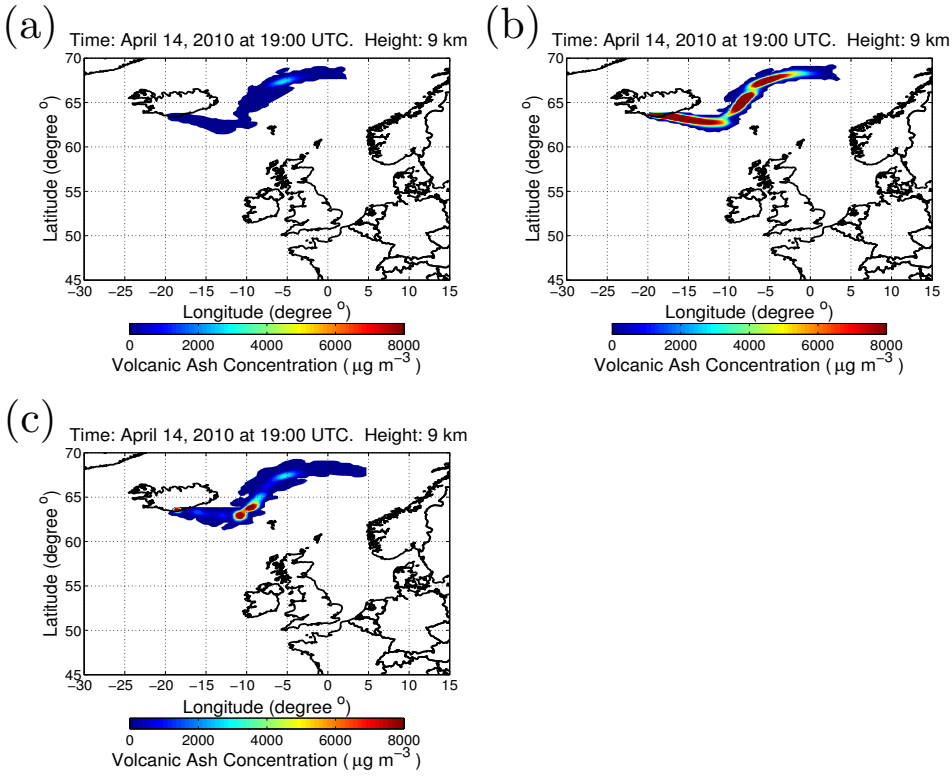

Figure 3.5: Comparison of results with and without assimilating aircraft-based measurements. (a) $\text{Tru}_{19:00(14)}$, (b) $\text{SimSta}_{19:00(14)}$ and (c) $\text{AnaSta}_{19:00(14)}$.

Now we have verified that through continuously assimilating aircraft-based measurements, an improved state is obtained. There are two main reasons that explain why it performs very well: (a) The measuring aircraft always follows the ash flowing trend and enters the plume outskirt to measure concentration. This movable aircraft-based measuring path makes the measurements always informative and useful for data assimilation; (b) the uncertainty knowledge of PH, MER and the measurements is known, which is important for EnKF to generate proper ensembles.

$\text{AnaSta}_{19:00(14)}$ can be used as an initial condition to do forecast over multiple days to see the possible improvement in advisories to aviation. Without loss of generality, the forecast at 00:00 (UTC) 15 April is chosen as illustration in Fig. 3.6. $\text{FC}^{n}_{00:00(15)}$ and $\text{FC}^{a}_{00:00(15)}$ are used to represent the forecast initiated with $\text{SimSta}_{19:00(14)}$ and the forecast with $\text{AnaSta}_{19:00(14)}$ as an initial condition.

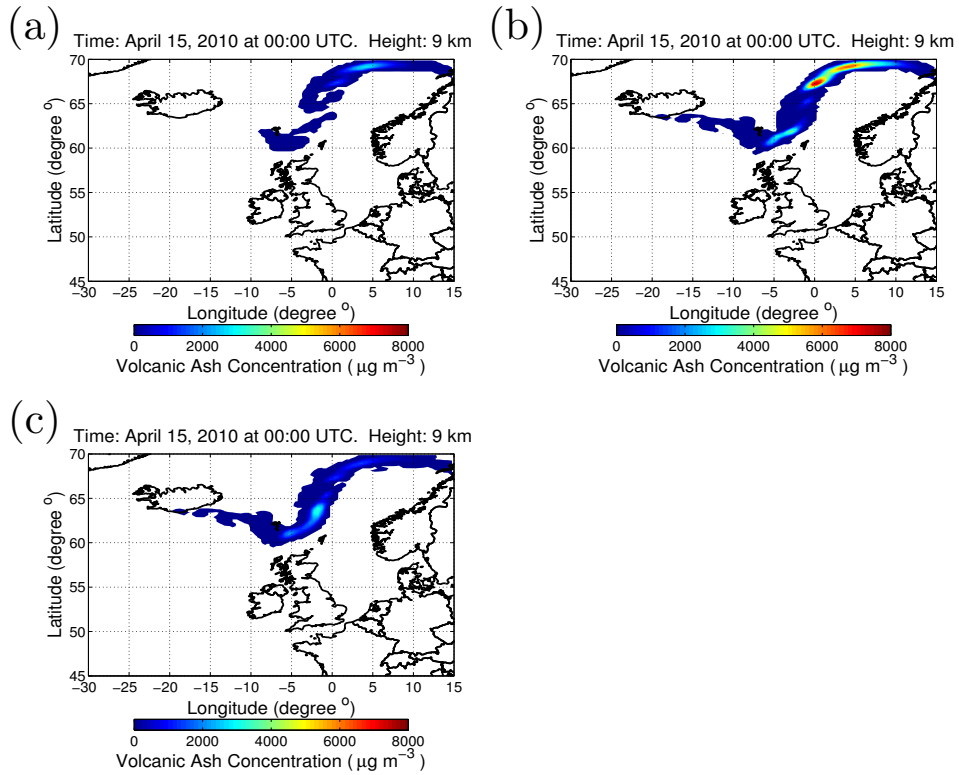

Figure 3.6: Comparison of Volcanic Ash Forecast with assimilating aircraft-based measurements and without assimilation. (a) $\text{Tru}_{00:00(15)}$, (b) $\text{FC}^{n}_{00:00(15)}$ and (c) $\text{FC}^{a}_{00:00(15)}$.

In Fig. 3.6, at time 00:00 (UTC) 15 April, 2010, we can see $\text{FC}^{a}_{00:00(15)}$ better approximates $\text{Tru}_{00:00(15)}$ than $\text{FC}^{n}_{00:00(15)}$. The result shows the forecast accuracy is improved through assimilating aircraft-based measurements. Note that in Fig.

3.6(a), the plume does not appear south of Iceland, it means in this area the ash plume is below the altitude of 9 km. In real life, the truth is unknown, thus usually Fig. 3.6(b) is used to provide advice to decision makers. In this experiment, if we use $FC^{n}_{00:00(15)}$ for the advice, then it will be that at 9 km ash concentrations in West-North areas outside Norway are higher than 6000 μg m^{-3}. Whereas in fact this advice is inaccurate compared to the truth which shows in these areas ash concentrations are lower than 4000 μg m^{-3}. This clearly shows only using simulation to provide advice is not sufficient for decision makers. Fig. 3.6(c) is the assimilation forecast combining 8 hours continuous aircraft real-time measurements (Fig. 3.2). The only difference between Fig. 3.6(c) and Fig. 3.6(b) is that Fig. 3.6(c) assimilates aircraft-based measurements. From Fig. 3.6(c), we can get an accurate advice with a much closer to truth estimate at 00:00 (UTC) 15 April, where ash concentrations in all the areas at 9 km are lower than 4000 μg m^{-3}. This is a big improvement compared to Fig. 3.6(b).

In this experiment, through initiation with $\text{AnaSta}_{19:00(14)}$, the forecast of volcanic ash transport has been significantly improved. This tells us for volcanic ash forecast, with a good state obtained from assimilating aircraft-based measurements, it can provide an improved advice for aviation. In the following, two other experiments are designed to study (1) for the interested advice at height level of 9 km, at which altitude the aircraft should fly to give the best analyzed state $\text{AnaSta}_{19:00(14)}$? (2) how important is having a good knowledge of uncertainties in parameters PH, MER and measurement?

3.3.3. Experiments with different flight levels

In this experiment, measurements are simulated at different altitudes as 7 km, 5 km, 3 km, respectively. The interested level is still 9 km as in last experiments and Fig. 3.7(a), Fig. 3.7(b) and Fig. 3.7(c) are the designed aircraft measurement routes at different heights 3 km, 5 km, 7 km, respectively. The performance of assimilating these measurements compared with the 9 km measurements is shown in Fig. 3.8. We extend $\text{AnaSta}_{19:00(14)}$ to $\text{AnaSta}^{3}_{19:00(14)}$, $\text{AnaSta}^{5}_{19:00(14)}$, $\text{AnaSta}^{7}_{19:00(14)}$ and $\text{AnaSta}^{9}_{19:00(14)}$ to represent the analyzed state at 19:00 (UTC) 14 April, 2010 through assimilating aircraft-based measurements from heights 3 km, 5 km, 7 km and 9 km, respectively. $\text{Tru}_{19:00(14)}$ is the truth and $\text{SimSta}_{19:00(14)}$ is the simulation result without assimilation. From Fig. 3.8(c) to Fig. 3.8(f), we can see that all cases with different altitude perform worse than the 9 km case, and some of them (3 km case and 5 km case) are even worse than the case without assimilation.

From these comparison, we can get that the locations (flight levels in this chapter) of aircraft-based measurements are crucial for providing a more accurate analyzed state on interested level. The best $\text{AnaSta}_{19:00(14)}$ is that assimilating aircraft-based measurements from the same flight level with interested level. Furthermore, Fig. 3.8(e) is also shown to perform an improvement compared to the case without assimilation. Thus based on $\text{AnaSta}^{7}_{19:00(14)}$ we can also obtain an improved advice where the overestimation of ash concentrations has been reduced compared to $\text{SimSta}_{19:00(14)}$.

Through this experiment, two conclusions can be drawn that (1) in order to get

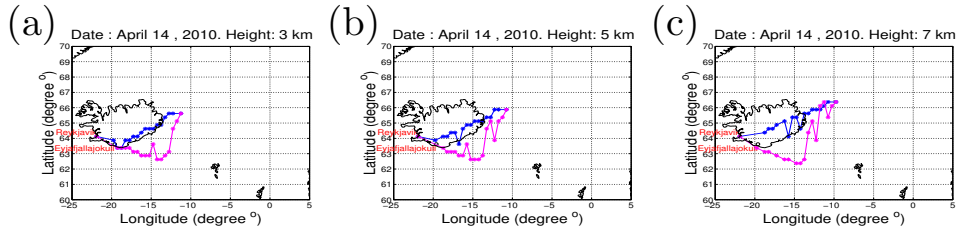

Figure 3.7: Designed aircraft-based measurements on different flight levels (a) 3 km, (b) 5 km and (c) 7 km.

the best analyzed state on the interested commercial aeroplane level with assimilation, the aircraft-based measurements should be preferably taken at the same level of height; (2) If this level measurements can not be provided, through assimilating measurements from close levels, an acceptable analyzed state can still be obtained.

3.3.4. Uncertainties in plume height, mass eruption rate and measurement

This experiment is undertaken to investigate the importance of having a good knowledge of uncertainties for assimilating aircraft-based measurements. In this chapter, the uncertainties of PH, MER and measurements are considered to be 20 %, 50 % and 10 % respectively as discussed in Section 3.3.1. However, if the uncertainty information can not be well estimated, how will the assimilation perform? What are the consequences due to overestimation and underestimation of uncertainty? Which uncertainty information is of most importance for ash forecast? To answer these three questions, we modify the three uncertainties in the experiment one by one and evaluate the performance. For evaluating influence of one uncertainty, we change its uncertainty with underestimation and overestimation, separately, while, we keep uncertainties of other two unchanged. The results are summarized in Fig. 3.9.

Fig. 3.9(g) is the truth, Fig. 3.9(h) is the analyzed state through assimilating aircraft-based measurements with the correct uncertainty information of PH, MER and measurement. Fig. 3.9(a) and Fig. 3.9(d) are the results with the wrong PH uncertainty of 10 % and 30 %, respectively. Similarly, Fig. 3.9(b) and Fig. 3.9(e) are results with the wrong MER uncertainty of 30 %, 70 %; Fig. 3.9(c) and Fig. 3.9(f) are results with the wrong measurement uncertainty of 1 % and 30 % respectively. We extend a superscript in $\text{AnaSta}_{19:00(14)}$ as PH10, PH30, MER30, MER70, meas01 and meas30 to represent these different cases, respectively.

The result in Fig. 3.9 shows that $\text{AnaSta}_{19:00(14)}$ with the correct uncertainties has the best performance to approximate the truth. All the other assimilation results are inferior to $\text{AnaSta}_{19:00(14)}$. Among them, some have very strong overestimation such as $\text{AnaSta}^{MER30}_{19:00(14)}$, $\text{AnaSta}^{MER70}_{19:00(14)}$ and $\text{AnaSta}^{meas30}_{19:00(14)}$. Based on these results, the answer to the first question is that when the uncertainty information is not well estimated, the assimilation accuracy cannot be guaranteed. In order to get

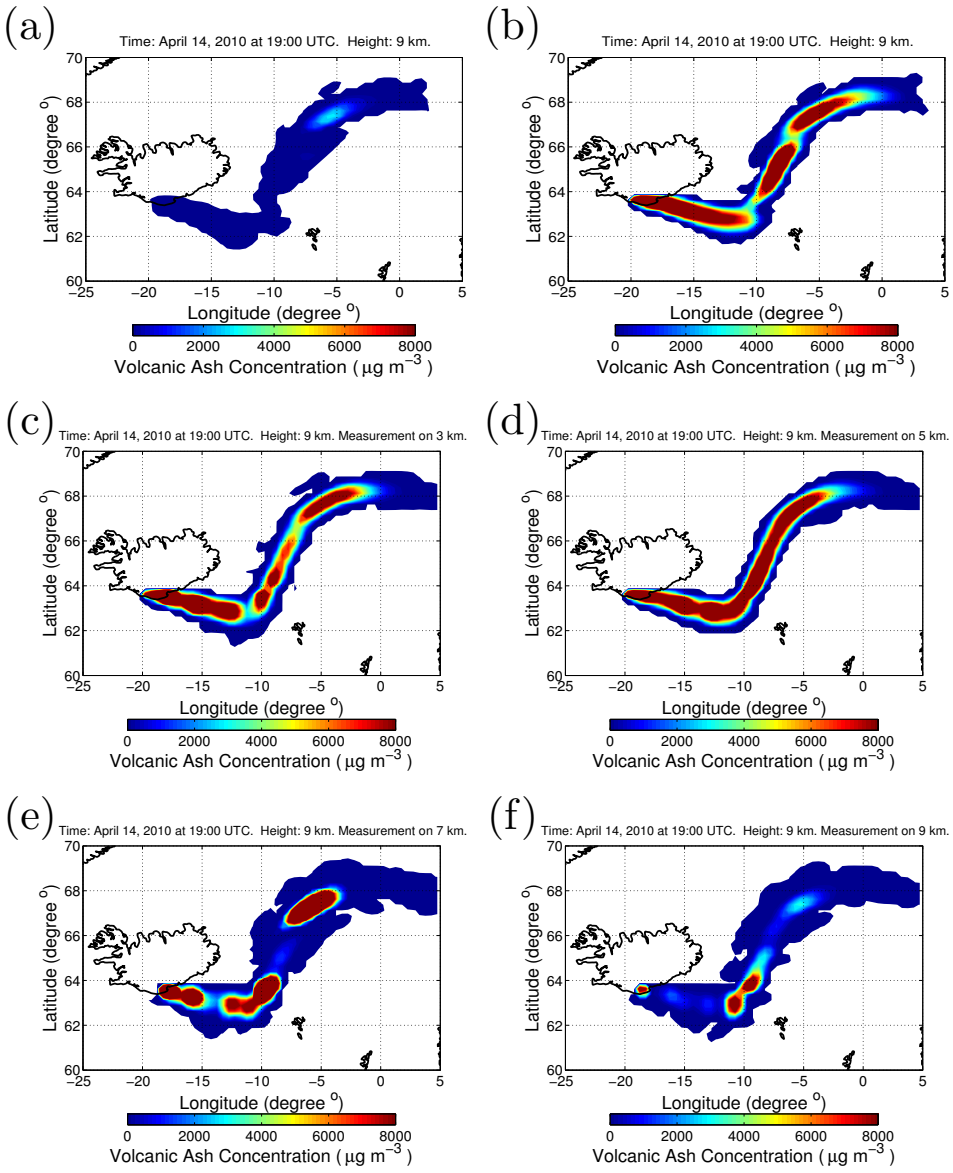

Figure 3.8: $\text{AnaSta}_{19:00(14)}$ Comparison with assimilating aircraft-based measurements taken from different flight levels. (a) $\text{Tru}_{19:00(14)}$, (b) $\text{SimSta}_{19:00(14)}$, (c) $\text{AnaSta}^{3}_{19:00(14)}$, (d) $\text{AnaSta}^{5}_{19:00(14)}$, (e) $\text{AnaSta}^{7}_{19:00(14)}$ and (f) $\text{AnaSta}^{9}_{19:00(14)}$.

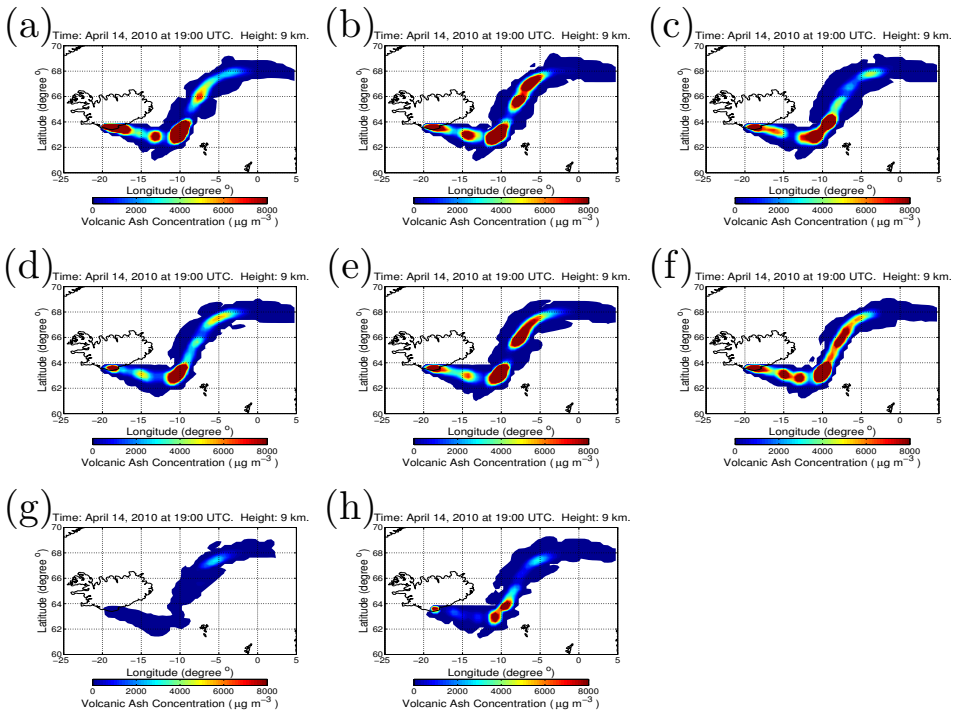

Figure 3.9: AnaSta$_{19:00(14)}$ implemented with different uncertainties of PH, MER and measurement. (a) AnaSta$^{PH10}_{19:00(14)}$, (b) AnaSta$^{MER30}_{19:00(14)}$, (c) AnaSta$^{meas01}_{19:00(14)}$, (d) AnaSta$^{PH30}_{19:00(14)}$, (e) AnaSta$^{MER70}_{19:00(14)}$, (f) AnaSta$^{meas30}_{19:00(14)}$, (g) Tru$_{19:00(14)}$ and (h) AnaSta$_{19:00(14)}$.

a better analyzed state in data assimilation systems, the uncertainties of PH, MER and measurement should be obtained as accurate as possible, otherwise analyzed state can become very unacceptable.

The second question is to investigate the consequences due to overestimation and underestimation of uncertainties. Fig. 3.9(a), Fig. 3.9(b) and Fig. 3.9(c) are forecast with underestimated uncertainty of PH, MER and measurement, respectively. Whereas Fig. 3.9(d), Fig. 3.9(e) and Fig. 3.9(f) are the cases with overestimated uncertainties. The result shows for uncertainties of PH or MER, overestimation can provide a better result, while for uncertainties of measurement, underestimation is better. This knowledge is of practical importance because when we are not sure about some parameter uncertainties in real-life assimilation, this investigation can give a guidance for choosing reasonable initial uncertainties.

Finding the most important uncertainty is equal to investigate which one is the most sensitive to forecast accuracy. For this, we first introduce a measure for sensitivity of accuracy, which is defined as:

$$(SenAccu)_p = \frac{|(TotalMass)_p(i) - (TotalMass)_p(j)|}{|(Uncert)_p(i) - (Uncert)_p(j)|}, \tag{3.1}$$

where p means one of the parameters PH, MER, measurement, i and j means implementations with parameter uncertainties. Moreover, $(TotalMass)_p$ and $(Uncert)_p$ represent total mass and parameter uncertainties corresponding to some parameter p. Using Eq. (3.1), we can get sensitivities of PH, MER and measurement as: $(SenAccu)_{PH} = 15.74$, $(SenAccu)_{MER} = 12.69$ and $(SenAccu)_{measurement} = 25.52$. So the parameter sensitivity in descending order is measurement, MER and PH. Thus, the most sensitive parameter for assimilation is measurement whose uncertainty is the most important uncertainty for achieving an accurate analyzed state. Therefore, we should be very careful about defining measurement uncertainty, a slight overestimation can already cause a big inaccuracy.

3.4. Conclusions

In this chapter aircraft-based measurements have been assimilated in a ensemble-based data assimilation system to provide volcanic ash transport forecast. Our goals were to improve ash transport forecast accuracy through assimilating aircraft-based measurements, and to study the impact of measurements from different flight heights and the influence of uncertainties in PH, MER and measurements.

Twin experiments were carried out to evaluate the assimilation results. The results showed through assimilating aircraft-based measurements, the forecast of volcanic ash transport can be significantly improved. The accurate advice of aeroplane flying safety was made through the assimilation forecast, whereas the simulation result gave a wrong advice.

Another experiment revealed that for the interested advice level 9 km, the aircraft-based measurements should be taken at this level. However, when at this level measurements can not be provided, through assimilating measurements from close levels, an acceptable advice can still be obtained. Through comparing assimilation result of correct PH, MER and measurement uncertainty with those of wrong

uncertainty information, we found that assimilating aircraft-based measurements only can perform well with sufficient knowledge of the statistics of the uncertainties. Otherwise, accurate assimilation results cannot be guaranteed. One thing needs to be mentioned that from this chapter, we investigated measurement is the most sensitive parameter for our assimilation system, which only means for assimilating aircraft-based measurements, not for all the other assimilation systems such as assimilating satellite measurements. For these assimilation systems, the sensitivity of parameters still needs to be investigated.

4

Model-based aviation advice on distal volcanic ash clouds

The forecast accuracy of distal volcanic ash clouds is important for providing valid aviation advice during volcanic ash eruption. However, because the distal part of volcanic ash plume is far from the volcano, the influence of eruption information on this part becomes rather indirect and uncertain, resulting in inaccurate volcanic ash forecasts in these distal areas.

In this chapter, we use real aircraft in situ observations, measured in the North-West part of Germany during the 2010 Eyjafjallajökull eruption, in an ensemble-based data assimilation system combined with a volcanic ash transport model to investigate the potential improvement on the forecast accuracy with regard to the distal volcanic ash plume. We show that the error of the analyzed volcanic ash state can be significantly reduced through assimilating real in situ measurements. After a continuous assimilation, it is shown that the aviation advice for Germany, the Netherlands and Luxembourg can be significantly improved. We suggest that with suitable aircrafts measuring once per day across the distal volcanic ash plume, the description and prediction of volcanic ash clouds in these areas can be greatly improved.

Parts of this chapter have been published in:
(Fu *et al.*, 2016a): *Model-based aviation advice on distal volcanic ash clouds by assimilating aircraft in situ measurements*, **Atmospheric Chemistry and Physics**, 16 (14), 9189-9200. doi:*10.5194/acp-16-9189-2016*.

4.1. Introduction

Currently a lot of approaches, employing satellite-based (Prata and Prata, 2012; Stohl *et al.*, 2011; Lu *et al.*, 2016b) or ground-based (Emeis *et al.*, 2011) measurements, focus on improving the estimation of Eruption Source Parameters (ESPs) such as plume height and mass eruption rate. These are very important for a good estimation of volcanic ash emission. However, for the volcanic ash plume far from the volcano which could be very important for local aviation, more accurate ESPs alone will not be very useful. This is mainly because (1) compared to ESPs, the plume transport becomes more and more dominant as the distance to the volcano increases (Macedonio *et al.*, 2016); (2) the small errors in ESPs can accumulate into large errors in predicted ash concentrations after a large transport distance (Webster *et al.*, 2012). Therefore, additional observation data, e.g., direct observations of distal volcanic ash plume must be employed to improve the aviation advice over continental Europe.

The benefit of aircraft in situ observations in an ensemble Kalman filter (EnKF) system has been studied in Chapter 3. It was shown using so-called twin experiments that ensemble-based data assimilation is in principle able to combine the aircraft in situ measurements with a volcanic ash transport and dispersion model (VATDM) to make improvements on volcanic ash estimation close to the eruption location. In that study, the focus was on the near-volcano areas where the uncertainties on plume height and mass eruption rate turned out to have a large influence on the estimates of the forecasted ash concentrations. However, for distal volcanic ash plume, these eruption parameters hardly improve the forecasts over a long distance. A larger mass eruption rate may cause the distal volcanic ash plume to spread stronger and wider after a long time period. But this potential effect can be significantly influenced or even canceled out by a combination of a number of elusive physical factors over a long time period such as wind speed and direction. Thus the results on near-volcano areas cannot be directly employed for far-volcano regions, e.g., central Europe in the case of a volcanic eruption in Iceland. In addition, the aircraft in situ measurements used in the previous studies were self-designed (artificial) based on model simulations from which actual conditions might differ significantly. For example, using data of a period of 10 hours by an aircraft gives accurate assimilation results. But in practical situations, a continuous aircraft measurement mission is at most 3 or 4 hours, thus it is still uncertain whether the assimilation can produce significant effect with a shorter measurement mission. Therefore, in case of real aircraft in situ measurements, it remains unknown whether the ensemble-based data assimilation still has significant improvements on the distal part of volcanic ash clouds and how long the influence will last. The answers of these questions will lead us to a solution for evaluating distal volcanic ash clouds and further provide accurate aviation advice. This chapter aims at investigating these questions. Note that, the term real aircraft measurements in this chapter refer to authentic measurements obtained by real aircrafts. This is to distinguish the artificial aircraft measurements as used in Chapter 3. Another term distal volcanic ash plume is used to clarify the chapter focuses on volcanic ash forecasts far from the volcano, i.e. continental Europe in this study.

This chapter is organized as follows. The assimilation experiments with real aircraft in situ measurements on distal volcanic ash clouds are specified in Section 4.2. Section 4.3 validates the performance of real data assimilation. Section 4.4 contains the benefit of the improved forecasts of distal ash plume on aviation advice, and also how much and how long the benefit has effect. Finally, the last section summarizes the concluding remarks of our research.

4.2. Sequentially assimilating real aircraft in situ measurements for distal volcanic ash clouds

4.2.1. Real aircraft in situ measurements

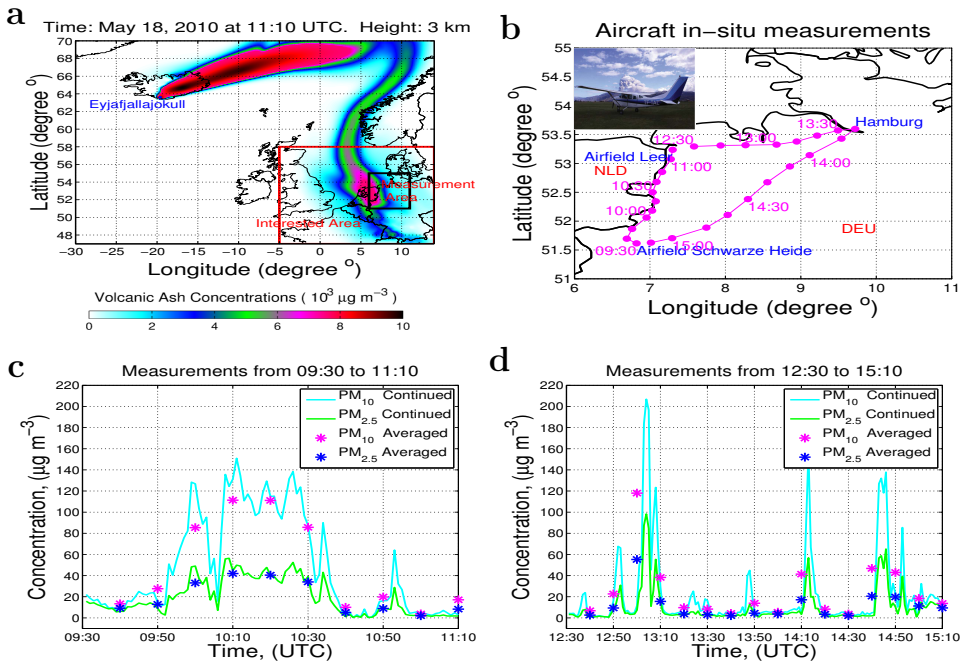

Figure 4.1: **Aircraft in situ measurements of distal volcanic ash plume.** **a**, The LOTOS-EUROS simulation of volcanic ash plume at 11:10 UTC, 18 May 2010. **b**, Measuring aircraft flight route on 18 May 2010. **c**, PM_{10} and $PM_{2.5}$ measurements from 09:30 UTC to 11:10 UTC. **d**, PM_{10} and $PM_{2.5}$ measurements from 12:30 UTC to 15:10 UTC. In **c** and **d**, the curves show the values of PM_{10} and $PM_{2.5}$ measured at a frequency of every 6 seconds. The values marked with a star are the averaged PM_{10} and $PM_{2.5}$ (average every 10 minutes) which are used in the LOTOS-EUROS model in accordance with the model simulation step (10 minutes).

In this chapter we used the aircraft-based measurements taken by one measurement flight on 18 May, 2010 performed by the group Environmental Measurement Techniques at Duesseldorf university of Applied Sciences. The measurements took place in the North-West part of Germany including the border between the Netherlands and Germany, see Fig. 4.1**d** (the red rectangular area in Fig. 4.1**a**).

The aircraft took off from the airfield "Schwarze Heide" in the Northern part of the Rhein-Ruhr area, headed along the Dutch border in the direction of the North Sea, continued towards Hamburg and then returned to the airfield. Along the route, concentrations of PM_{10} and $PM_{2.5}$ (corresponding to ash_5 and ash_6 in Table 2.1) were measured, see Fig. 4.1**e** and 4.1**f**.

4.2.2. Experimental Setup

The ensemble Kalman filter (EnKF) is used in this chapter to assimilate real aircraft in situ observations. The LOTOS-EUROS model run starts at 09:00 UTC 14 April 2010 by considering a zero initial condition, equivalent to an assumption of "no ash load yet". The volcanic ash is released during the first guess forecast based on the defined ESPs (PH, MER, VMD, PSD), as discussed in Section 2.1.4. The model state propagates along the numerical simulation with a time step of 10 minutes), then the model result is taken as an initial state for the next time step. When the model run arrives at 09:40 UTC 18 May, the ash state of volcanic cloud starts to be continuously corrected by data assimilation through combining real aircraft-based measurements taken along the Dutch border until the time 11:10 UTC 18 May.

Since the real measurements of the PM_{10} and $PM_{2.5}$ concentrations are available and the uncertainties of this type of measurements are approximately known, ensemble-based data assimilation can be used to combine them with the LOTOS-EUROS model to reconstruct optimal estimates.

4.2.3. Evaluation of real data assimilation

It is first examined how the data assimilation actually performs in the system. Fig. 4.2 shows the measurements, the mean of the ensemble members, as well as the forecast and the analysis of selected ensemble members. From the estimation of both volcanic ash components PM_{10} and $PM_{2.5}$ (Fig. 4.2**a** and Fig. 4.2**b**), we find the forecast mean largely overestimates the measurement at every time step, but the overestimation diminishes by the assimilation process significantly. Instead, the analysis mean consistently approximates ("very close") the measurements with a high accuracy. This result illustrates that the assimilation at the measurement location is able to approximate the observed values and also solves the problem of overestimation. Moreover, at the measurement location, the spread in the analysis ensembles is much smaller than that in the forecast ensembles, which means the error variance of analysis value at the measurement locations is significantly reduced through the use of assimilation. This is because aircraft in situ measurements are of high accuracy. Note that, Fig. 4.2**a** and Fig. 4.2**b** only show the ensemble mean and the spread of the ensembles at the measuring locations. However, we also want to know how much impact assimilation of aircraft in situ measurements can have on a wide area of the distal volcanic ash plume. If the impact is only limited to the measurement locations or only a small nearby area of ash plume, there will be no significant improvement in terms of aviation advice because flights need a rather large domain for safety guarantee.

In order to further investigate this effect, we first show the ensembles of uncertain volcanic ash simulations (see Fig. 4.2**c** and Fig. 4.2**d**), which correspond to

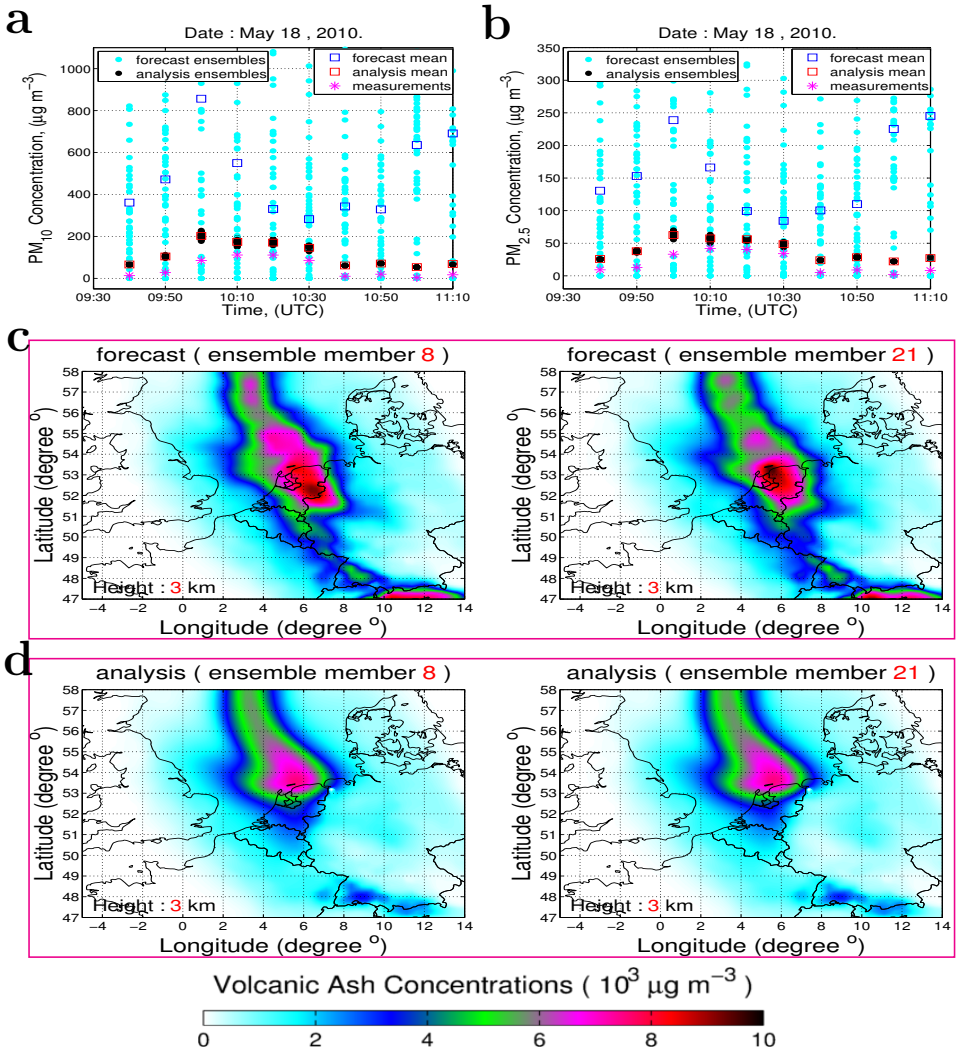

Figure 4.2: **Assimilation effect from 09:40 UTC to 11:10 UTC, 18 May, 2010. a** and **b**, Volcanic ash concentrations of PM_{10} and $PM_{2.5}$ at measurement locations. **c** and **d**, Volcanic ash ensemble state (ensemble member 8 and 21) of forecast and analysis at 11:10 UTC. The measurements, ensembles and mean of forecast and analysis are shown in **a** and **b**. In **c** and **d**, the area of interest is marked as red rectangular in Fig. 4.1**a**. The evaluation height is chosen at 3 km since the measurements are taken at altitudes around this height, see Section 4.2.1.

the ash distribution at 11:10 UTC 18 May 2010 before and after assimilation. Note that, this chapter focuses on the distal volcanic ash plume, thus only the area of the whole plume marked as red rectangular as shown in Fig. 4.1**a** is of interest. Without loss of generality, ensemble member 8 and 21 are chosen for illustrating the ensemble spread of the distal ash plume. Through comparing different ensemble members with respect to the forecast at 11:10 UTC (Fig. 4.2**c**), the ensemble forecast member 21 is shown to be very different from the member 8 in almost all the complete distal plume, thus the large error of the forecast is not only at measurement locations, but also in a large area around the measurement. Compared to the forecast, ensembles of analysis state (Fig. 4.2**d**) show no large differences across the entire domain of interest. This tells us that assimilating aircraft measurements effectively reduce the ensemble spread of the whole distal ash plume, which is a sign of consistency to the measurement locations.

Next, we investigate the assimilation impact on the ensemble mean over the distal volcanic ash plume. Fig. 4.3 shows examples of the mean at 09:40 UTC and 11:10 UTC 18 May with and without assimilating aircraft measurements. Compared to the case without assimilation at 11:10 UTC (Fig. 4.3**b**), large differences can be observed in the simulation results with a continuous assimilation (Fig. 4.3**d**). Note that areas with ash concentration higher than 4000 μg m^{-3} are classified as No Fly Zone (NFZ) (EASA, 2015), which means aviation in these areas is not allowed. After the assimilation process, the calculated volcanic ash concentrations in Germany, Luxembourg and the Netherlands (except in Northern Netherlands) have a lower concentration level (lower than 3000 μg m^{-3}) and the changes on volcanic ash state can be seen across a wide area. This is because the volcanic ash state variables become dependent and correlated due to the transport process (advection and diffusion) and the temporal correlation of emission, see Chapter 3. Thus in a fairly large domain, the state change at measurement location also influences state variables in surrounding areas. This is caused by the chosen localization radius of 500 km in the assimilation process. Further, the downwind direction includes influenced state variables due to the transport of earlier corrected ash concentrations, especially regarding forecasts later than the assimilated time steps. Note that after a careful check on the wind field around the aircraft route, the term "downwind" direction means the direction of "South-East", which will be used in the following discussions. Another note is that the differences between with and without assimilation are not obtained in one-time, but step by step with assimilating measurements over a period of one and a half hours from 09:40 UTC to 11:10 UTC. This can be seen from the assimilation results at 09:40 UTC and 11:10 UTC (Fig. 4.3**c** and Fig. 4.3**d**) where clear differences (Fig. 4.3**e** and Fig. 4.3**f**) between the two times can be observed and the effect of the assimilation at 09:40 UTC is less pronounced than at 11:10 UTC. This shows that after a continuous assimilation of aircraft measurements, the differences with the original simulation are the result of an accumulation of all previous assimilation effects. This analysis also tells us that all the assimilation steps are important for the final result and that only using one or two measurements does not produce accurate results.

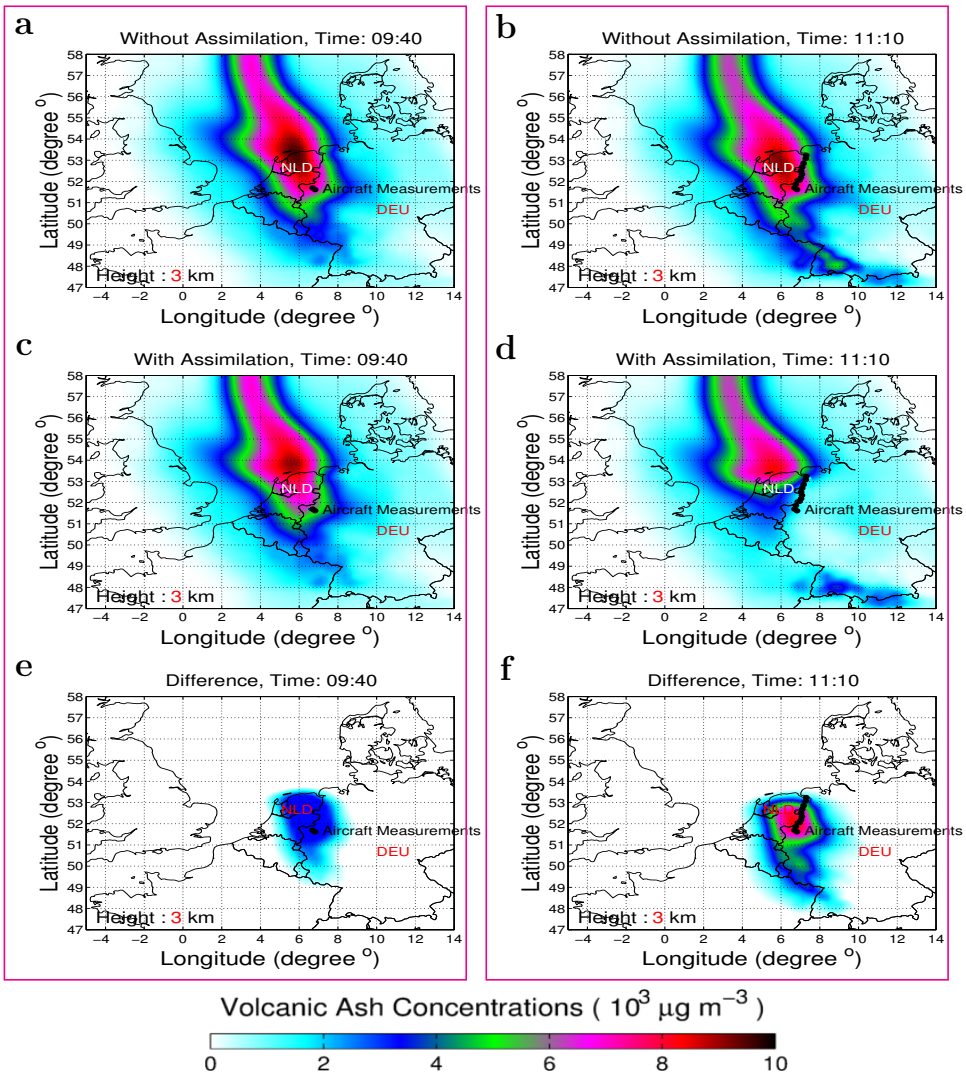

Figure 4.3: **Comparison with and without assimilating aircraft in situ measurements on 18 May 2010.** **a** and **b**, Simulation results without assimilation at 09:40 UTC and 11:10 UTC. **c** and **d**, Simulation results with assimilation at 09:40 UTC and 11:10 UTC. **e**, Differences of **a** and **c**. **f**, Differences of **b** and **d**. The differences are in absolute values which are obtained by numerically subtracting the values between **a** and **c**, or **b** and **d**. **e** and **f** represent the areas where the assimilation has effect.

4.3. Validation of assimilation performance

Based on the analysis above, significant differences between volcanic ash simulations without and with assimilation have been revealed. To examine whether the assimilated results are indeed more accurate than the model results, a further validation must be conducted. Fig. 4.4**a** and Fig. 4.4**b** show the comparison of the forecasted volcanic ash plumes with and without assimilation. The basic idea of this validation is to compare future in situ measurements with the forecast of the volcanic ash plumes initiated with Fig. 4.3**b** and Fig. 4.3**d**. After the assimilation process, the assimilation influenced region temporally propagates to the downwind direction due to the meteorological drive (wind speed and direction). Thus the forecasted downwind ash concentrations are influenced along the length of integration time after assimilation. Because all the other settings in the system are the same, a better forecast is expected due to a more accurate initial state. We use the measurements from 09:30 UTC to 11:10 UTC along the Dutch border to produce the assimilated results, then we validate the results using another set of aircraft in situ measurements in the downwind direction taken from 14:10 UTC to 15:00 UTC 18 May 2010 (see Fig. 4.1**b** and 4.1**d**). The validation data is selected carefully with respect to the influenced area (Fig. 4.3**f**).

With different initialization, the forecast of volcanic ash concentration at 15:00 UTC shows large differences. The forecast after assimilation (see Fig. 4.4**b**, lower than 3000 μg m^{-3} in the downwind direction of the measurement track) is much smaller than that without assimilation (Fig. 4.4**a**, higher than 4000 μg m^{-3} in some areas of continental Europe). Note that the forecast for both cases may be performed better by combining adjustments to state variables as well as eruption parameters. The detailed ash concentrations of two forecasts are compared with measurements in Fig. 4.4**c** and 4.4**d**. Both forecasts are shown to overestimate the measurements. This is in accordance with practical experience that volcanic ash simulations often overestimate the truth to guarantee a safe aviation advice. This is because in practice, if engine performance experiments cannot be designed in accurate and realistic conditions of volcanic ash clouds, cautious approaches (overestimation) to guide commercial flight operations in airspace during volcanic ash transport are often recommended (Prata and Prata, 2012). Furthermore, we can also see that at each validation location, the forecast with assimilation is closer to the measurements than the forecast without assimilation, and also that the overestimation is significantly reduced using assimilation. This shows that the forecast at these locations with assimilation is more accurate than the forecast without assimilation, therefore the assimilated volcanic ash state (Fig. 4.3**d**) is a more accurate approximation to the real state of the distal volcanic ash plume. In addition, we conclude that the assimilation process performs well in combining with the LOTOS-EUROS transport model with real measurements.

4.4. Assimilation benefit for aviation community

Next it will be investigated what is the benefit of the improved forecasts of distal ash plume on aviation advice, and also how much and how long the benefit has

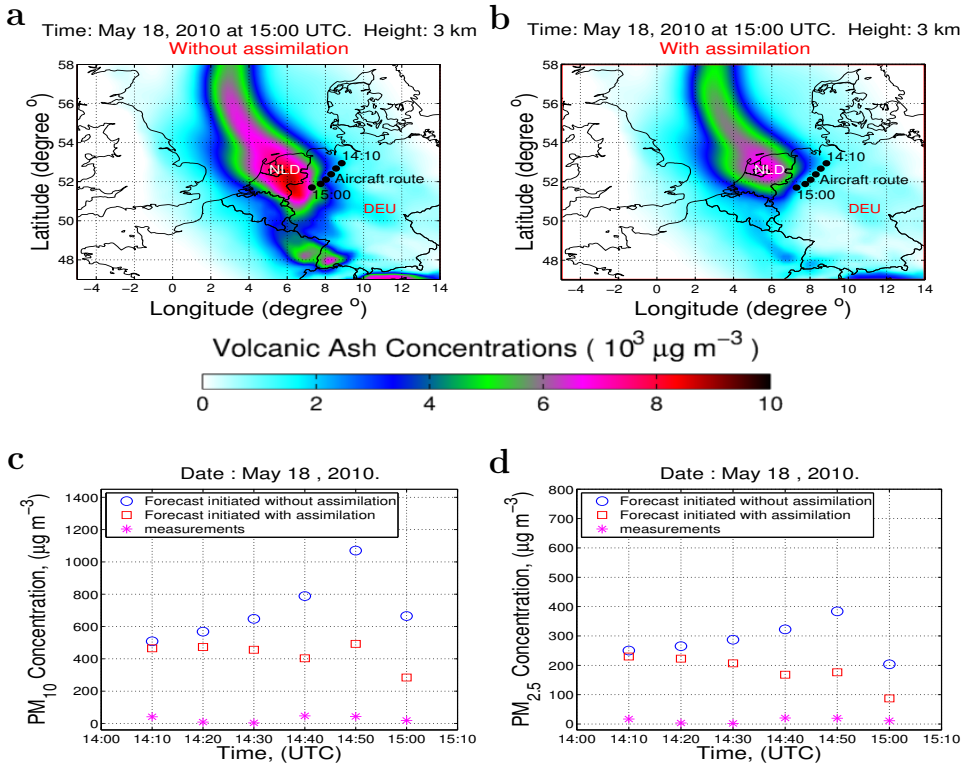

Figure 4.4: **Forecast at 15:00 UTC 18 May 2010 with different initial conditions for the volcanic ash state. a**, Forecast initiated with (Fig. 4.3**b**). **b**, Forecast initiated with (Fig. 4.3**d**). **c**, PM_{10} concentration from 14:10 UTC to 15:00 UTC. **d**, $PM_{2.5}$ concentration from 14:10 UTC to 15:00 UTC.

an effect. Firstly, the assimilation impact in the downwind and upwind directions is considered. For this investigation, 5 big cities around the measurement route are selected (see Fig. 4.5**a**). They are Dortmund, Cologne, Luxembourg in the downwind direction and Amsterdam, Rotterdam in the upwind direction. The evaluation height is chosen at 3 km. For some continental or intercontinental passenger flights, 3 km might be of special interest regarding taking off and landing. The evaluation time is chosen to be 11:10 UTC 18 May 2010 when the assimilation process finishes. The concentrations of two major distal volcanic ash components, i.e., PM_{10} and $PM_{2.5}$ (Webley *et al.*, 2012), are evaluated. Fig. 4.5**b** shows that results with assimilation is lower for both PM_{10} and $PM_{2.5}$ in all the selected cities. To quantify this impact on estimation of both ash components, an impact rate (IR) is introduced for quantification. The IR is defined as:

$$(\mathrm{IR})_p(i) = \frac{(\mathrm{SimuNoAssimi})_p(i) - (\mathrm{SimuAssimi})_p(i)}{(\mathrm{SimuNoAssimi})_p(i)}, \tag{4.1}$$

where p means either PM_{10} or $PM_{2.5}$, i means index of selected cities. Moreover, $(\mathrm{SimuNoAssimi})_p$ and $(\mathrm{SimuAssimi})_p$ represent two simulations without or with assimilation. Using this equation, we can get the IR of all cities (see Fig. 4.5**b**). Based on the IR values, we find the assimilation impact in the downwind direction (Dortmund, Cologne and Luxembourg) are much more significant than those in the upwind direction (Amsterdam, Rotterdam). This means after assimilation, the most significant impact on ash clouds is in the downwind direction where in this chapter it is mainly Germany (see assimilation impact areas in Fig. 4.3**f**).

The analysis above demonstrates that assimilating aircraft in situ measurements has the ability to impact on regional volcanic ash clouds, especially in the downwind direction of the measurement route. It is also shown that assimilation has an impact on aviation advice. If there is no assimilation employed (see Fig. 4.3**b**), the volcanic ash concentration in the main transport direction of the distal ash plume reaches over 4000 μg m^{-3}. Thus, only relying on simulation results, the aviation advice on continental Europe is that the sky above the North Sea, the Netherlands and the western part of Germany is forbidden for flights. This aviation advice would shutdown flights in a large area. Because the Netherlands and Germany are important aviation hubs in Europe, imposing such a no-fly zone will affect all flights in the ash penetrated area and subsequently leads to a huge economic loss. In contrast, if based on the improved simulation after a continuous assimilation (Fig. 4.3**d**), the aviation advice would have been changed. The sky in large parts of Europe is open for commercial flights, because except in small parts of the Netherlands ash concentrations all over the domain of interest are lower than 3000 μg m^{-3}. This illustrates that the accuracy of aviation advice and the NFZ area can significantly benefit from the ensemble-based data assimilation process. Note that we give the aviation advice only on the strength of the results at 3 km height. Generally all model levels must be analyzed for real cases. And the real aviation advice also includes for which exact area and which time frame the advice is given.

Another question is how long the effect of improvement by assimilating aircraft measurements will last? The answer of this will provide us guidance on how often

a

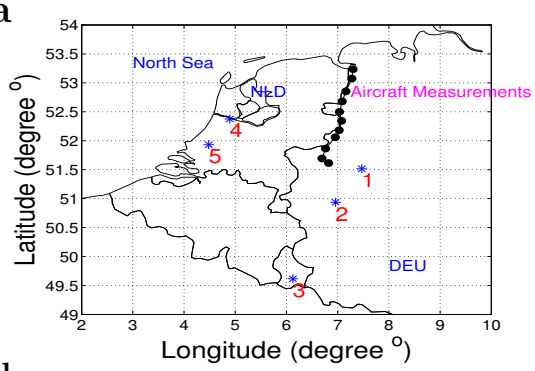

Germany (DEU)	1	Dortmund
	2	Cologne
Luxembourg (LUX)	3	Luxembourg
Netherlands (NLD)	4	Amsterdam
	5	Rotterdam

b

	City Number / Simulation	downwind			upwind	
		1	2	3	4	5
PM_{10}	Without assimilation(μg m^{-3})	574.0	817.5	568.8	1055.3	863.4
	With assimilation(μg m^{-3})	112.1 ↓	219.1 ↓	262.5 ↓	717.8 ↓	724.2 ↓
	Impact rate	80.5%	73.2%	53.9%	32.0%	16.1%
$PM_{2.5}$	Without assimilation(μg m^{-3})	243.7	344.6	216.1	387.9	306.3
	With assimilation(μg m^{-3})	49.3 ↓	90.5 ↓	97.3 ↓	259.3 ↓	256.6 ↓
	Impact rate	79.8%	73.7%	55.0%	33.2%	16.2%

Figure 4.5: **PM_{10} and $PM_{2.5}$ evaluation on selected cities with and without assimilation. a**, Selected international cities around the aircraft measurement track. City 1 – 3 are in the downwind direction, while city 4 – 5 are in the upwind direction. **b**, Concentrations of PM_{10} and $PM_{2.5}$ and the quantified impact rates on selected cities. The height of interest is chosen at 3 km. The red arrow represents the trend of concentration values due to the assimilation process. The impact rates in downwind and upwind cases are distinguished by blue and magenta colors.

aircraft measuring should be performed. For investigating the time period of the assimilation impact, the volcanic ash plume is forecasted one day (Fig. 4.6) starting at 11:10 UTC 18 May 2010. Without loss of generality, PM_{10} is chosen to analyze the forecast performance. 3 time snapshots in Fig. 4.6**a** – Fig. 4.6**c** are chosen to show the forecast differences between without and with assimilation. Since there are clear differences between the two cases, the assimilation impact can last one day. Note that this impact duration is only valid for the areas (especially for regions downwind to the assimilated observations), that are influenced by the assimilation, which changes with time. When forecasting 24 hours (Fig. 4.6**c**), differences still can be observed, but the impact of assimilation is obviously getting much smaller (compared to Fig. 4.6**a** and Fig. 4.6**b**). Actually we also examined the assimilation impact in the forecast of the next day and observed only very small differences. Therefore, the time period of the assimilation impact of this case study can be taken as 24 hours. From this analysis, we suggest the frequency of the measurement campaign to be once per day. This study can be used to provide guidelines for an optimal flight schedule in regional measurement tasks. Note that the impact time investigated is based on the meteorological information in distal volcanic ash plume during the period considered in this chapter. For other cases, the duration of effective assimilation could be differed.

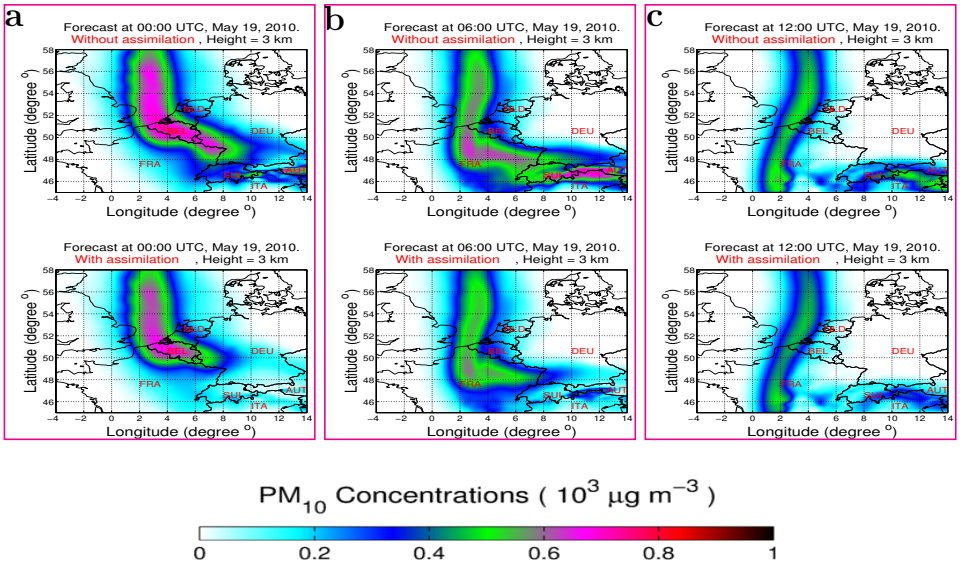

Figure 4.6: **One-day forecast of PM_{10} concentration with and without assimilation.** A larger domain is chosen in this figure (compared to Fig. 4.2, 4.3, 4.4) to demonstrate the downwind change (with time) of the assimilation influenced area. **a**, Forecast at 00:00 UTC 19 May 2010. **b**, Forecast at 06:00 UTC 19 May 2010. **c**, Forecast at 12:00 UTC 19 May 2010.

4.5. Conclusions

In this chapter, aircraft in situ measurements in distal volcanic ash clouds were assimilated in the LOTOS-EUROS model. During a continuous assimilation, the error of the analyzed volcanic ash state was significantly reduced through assimilating real in situ measurements. The improved volcanic ash state after assimilation are the result of an accumulation of all previous assimilation effects. It was shown that all the assimilation steps contribute to the final result. To examine whether the assimilated volcanic ash state were indeed more accurate than the conventional simulation, a validation with future in situ measurements was conducted. The forecast with assimilation was shown more accurate than the conventional forecast without assimilation. It also concluded that the assimilation process performed well in combining with the LOTOS-EUROS transport model with real measurements.

The validation results also revealed that with the transport models alone, it is difficult to accurately model volcanic ash movements. This is probably because model parameters (e.g., the plume height) are uncertain and some processes are missing, for example, coagulation, evaporation, and resuspension. Analysis of the results showed that the data assimilation approach used herein is able to compensate some of the model's deficiencies. Aircraft in situ measurements have a high accuracy and plays an important role to a successful data assimilation. The aircraft can enter the plume to selectively obtain observations, so that the measurements are in situ and optimal for the ensemble-based data assimilation methodology.

Investigation was also carried out on the benefit of the improved forecasts of distal ash plume on aviation advice. We found that after assimilation, the most significant improvements on distal ash clouds are in the downwind direction where in this chapter it is mainly Germany. This phenomenon is due to the wind direction and the transport process during the continuous assimilation. Investigation shows that the accuracy of aviation advice within the assimilation influenced area can significantly benefit from the ensemble-based data assimilation process. The computer experiment revealed that the time period of the improvement effect on the areas downwind to the assimilated observations can be taken as 24 hours. Based on this result, we suggest to schedule an aircraft measurement campaign at a frequency of once per day. This can be used to provide guidelines for planning future regional measurement tasks. The suggested frequency should be adjusted by the temporal strength (due to wind induced transport) on the assimilation influenced area.

5

A two-way-tracking localized ensemble Kalman filter for assimilating aircraft in situ volcanic ash measurements

Data assimilation uses observations to improve the forecast accuracy. Among the data assimilation approaches, the ensemble Kalman filter (EnKF) is a well-known and popular method. A proper covariance localization strategy in the analysis step of EnKF is essential for reducing spurious covariances caused by the finite ensemble size, as shown for this application for assimilation of aircraft in situ measurements.

After analyzing the characteristics of the physical forecast error covariances, we present a two-way tracking approach to define the localization matrix for covariance localization. The result shows that the Two-way-tracking Localized EnKF (TL-EnKF) effectively maintains the correctly specified physical covariances and largely reduces the spurious ones. The computational cost of TL-EnKF is also evaluated and is shown to be advantageous for both serial and parallel implementations. Compared to the commonly used distance-based covariance localization, the two-way tracking approach is shown to be more suitable. In addition, the covariance inflation approach is verified as an additional improvement to TL-EnKF to achieve more accurate results.

Parts of this chapter are under review:
(Fu et al., 2016): *A two-way-tracking localized ensemble Kalman filter for assimilating aircraft in situ volcanic ash measurements*, **Monthly Weather Review (under review)**.

5.1. Introduction

Because of the limited ensemble size, ensemble-based assimilation methods often produce severe spurious noises between measurements and state variables (Houtekamer and Mitchell, 1998; Anderson, 2001). This side effect implies that some state variables which are in fact uncorrelated with an observation are computed as correlated, resulting in an unphysical update. Over time, this will lead to an erroneous reduction of ensemble variance which may significantly underestimate the true variance and finally may lead to filter divergence (Anderson, 2001; Evensen, 2009).

Covariance localization (Houtekamer and Mitchell, 1998; Gaspari and Cohn, 1999; Hamill *et al.*, 2001) is a process of 'cutting off' spurious covariances in the error covariance matrices, which improves the estimate of the forecast error covariances. The localized covariance matrix is more suitable to represent the forecast uncertainty during assimilation (Petrie and Dance, 2010). The localization is achieved using a Schur product of the forecast error covariance matrices and a localization matrix (Houtekamer and Mitchell, 2001). The localization matrix is chosen with ones on the diagonal and with other values decreasing to zero from the diagonal to a specified distance. Thus, the structure of the localization matrix is a band of non-zero elements around the leading diagonal. The distance where the error covariances are reduced to zero is known as the "filtering length scale". It is crucial that when unphysical (spurious) covariances are eliminated, physical (correct) covariances remain well maintained. If the filtering length scale is too long (i.e., all the physical and unphysical covariances are allowed), many of the spurious covariances may not be eliminated well. On the other hand, if the filtering length scale is too short, important physical covariances then may be lost together with the spurious covariances. Therefore, for a given assimilation application, it is essential that the filtering length scale is correctly chosen.

Usually, deciding the length scale for real-time assimilation is a heuristic (experience-based) process (Petrie and Dance, 2010). It is effective for applications where the physical forecast error covariances appear to be "isotropic", such as in weather forecasting (Houtekamer and Mitchell, 2005), SO_2 (Barbu *et al.*, 2009), ozone (Curier *et al.*, 2012) and CO_2 forecasting (Chatterjee *et al.*, 2012). However, if the physical forecast error covariances tend to be "anisotropic", the length scale ("distance" used to calculate the localization matrix) can be defined based on some specific dynamics, e.g, the usage of ensemble forecast sensitivity area on the simple Lorenz 40-variable model (Kalnay *et al.*, 2012), the water- and gas-phase streamline in reservoir engineering (Arroyo *et al.*, 2013), the dynamic height field in an oceanographic application (Cummings, 2005), the potential temperature as the vertical coordinate for tracer assimilation (Riishojgaard, 1998), the usage of the topography as a "vertical" coordinate for a 2d analysis application (Deng and Stull, 2005).

Therefore, for a given assimilation system, how to create a suitable localization matrix (how large the heuristic length scale is or what model dynamics should be included) for covariance localization depends on the characteristics ("isotropic" or "anisotropic") of the physical error covariances for a specific application. In this

chapter, we aim to investigate a suitable covariance localization for volcanic ash data assimilation. The measurements used in the ensemble-based assimilation system are aircraft measurements taken in West-North Germany (Weber *et al.*, 2012). Typically more flights would be carried out after an eruption. For this chapter, we consider one, in order to study the localization process in detail. In (Fu *et al.*, 2016a), the measurements of this flight has been assimilated (including independent validation of the assimilation performances) to improve regional volcanic ash forecasts and aviation advice in the Netherlands and Germany. In that application, a constant filtering length scale (500 km) was used to define the localization matrix. That approach made sense since the region of interest (i.e., the Netherlands and Germany) was quite small compared to the full plume's coverage (almost the whole of Europe). However, the focus in this chapter is on the dynamical covariances over the entire plume and the aim is to design an accurate localization matrix for covariance localization to maintain the correctly specified physical covariances and to remove spurious ones as far as possible.

This chapter is organized as follows. The estimates and the characteristics of the physical error covariances are investigated in Section 5.2. In Section 5.3, the two-way-tracking covariance localization approach is proposed and formulated in details. To support and verify the methodology, experimental results are given and discussed in Section 5.4. Finally, the last section summarizes the concluding remarks of this chapter.

5.2. Estimates and characteristics of the physical forecast error covariances

5.2.1. Approximation of the physical forecast error covariances using a large ensemble size

To define a proper and accurate localization matrix **f** in Eq. (2.9), the physical ("real") forecast error covariances must be first investigated. Usually the physical error covariances cannot be directly obtained, but can be approximated with the sampled covariance matrix, i.e., $\mathbf{P}^f$ (in Eq. (2.7)). As the ensemble size increases, $\mathbf{P}^f$ gets close to the physical forecast error covariances. Thus, we first approximate the physical error covariances with the sampled forecast error covariance matrix $\mathbf{P}^f$ using a large ensemble size.

Fig. 5.1**a** and 5.1**b** are the illustrations of $\mathbf{P}^f$ (actually $\mathbf{P}^f\mathbf{H}^T$) using ensemble sizes of 50 and 500, respectively. The ash_5 concentrations at the measurement height are chosen to illustrate the results. Shown in each figure are the results at 09:40 UTC at the first assimilation step. Note that Fig. 5.1**a**/ 5.1**b** represents one column of $\mathbf{P}^f$, representing the covariances between one state variable (at an aircraft measurement location) and all the state variables (in the full domain). Compared to the rather stable covariance pattern in 5.1**b**, the spurious covariances are clearly shown in Fig. 5.1**a**. Fig. 5.1**a** indicates that, to overcome the spurious covariances at an ensemble size of 50, covariance localization must be employed to improve the performance. Actually, the forecast error covariances with other ensemble sizes (e.g., 400 and 600) have also been used and 500 is found as the

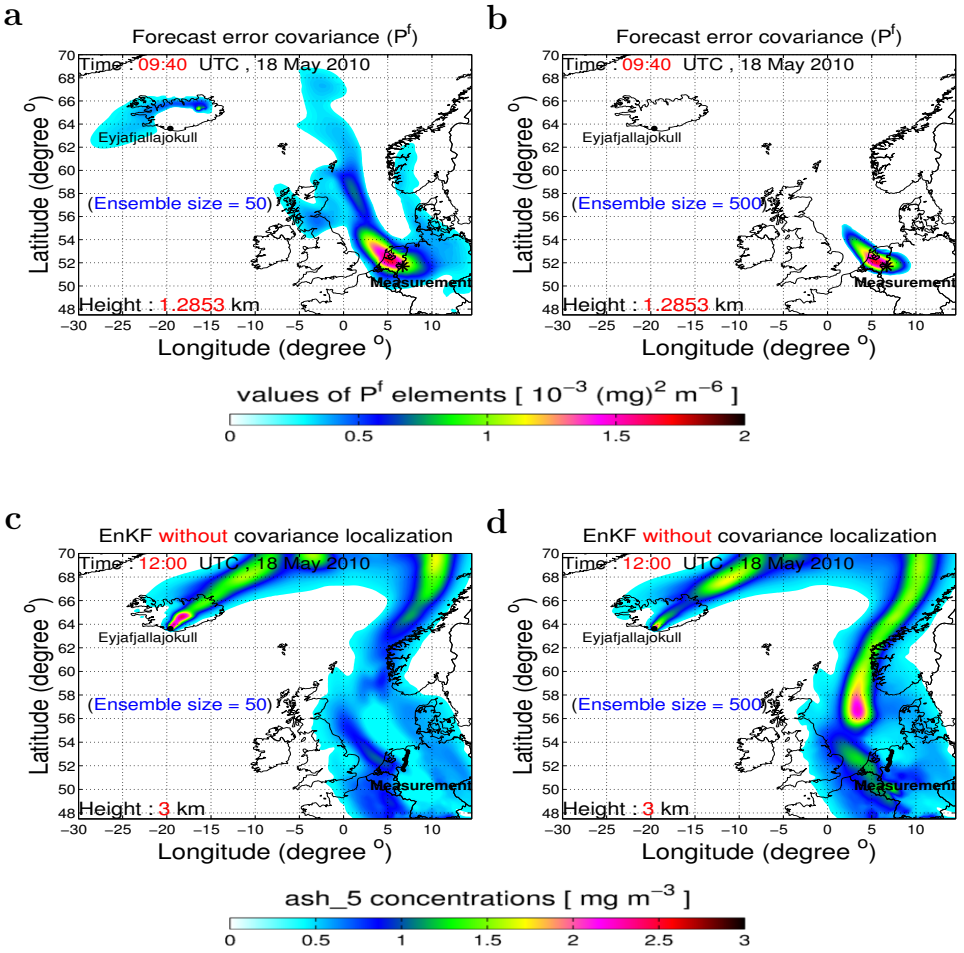

Figure 5.1: **Estimate and impact of the physical error covariances. a** illustrates the forecast error covariances at 09:40 UTC, 18 May, 2010 with an ensemble of 50, i.e., $\mathbf{P}^f[50]$. **b** is the illustration of $\mathbf{P}^f[500]$, which is used as the reference to the physical ("real") forecast error covariances. **c** shows the ash concentrations using EnKF[50] and also shows the accumulation effect of the spurious $\mathbf{P}^f[50]$. **d** is the EnKF[500] result, implemented by the accurate $\mathbf{P}^f[500]$.

smallest ensemble size to approximate the physical error covariances sufficiently accurate. Thus, $\mathbf{P}^f$ at an ensemble size of 500 (Fig. 5.1**b**, abbreviated as $\mathbf{P}^f[500]$) is used in this chapter as a reference to represent the physical error covariances.

Table 5.1: **Computational time of EnKF and TL-EnKF in different cases (ensemble sizes of 50 or 500, without or with covariance inflation).** The time measured is Wall clock time. The results are obtained from the bullx B720 thin nodes of Cartesius cluster, SURFsara, the Netherlands Supercomputing Center. Each node is configured with 2 × 12-core 2.6 GHz Intel Xeon E5-2690 v3 (Haswell) CPUs/node and with memory 64 GB/node. ('m'=minute , 'S'=serial, 'P'=parallel, '—'=not test or not exist.)

Cases[ensemble size]	EnKF[50]	EnKF[500]	TL-EnKF[50]	TL-EnKF[50]-Inflation
Forecast (S/P)	61.8 m / —	875.9 m / 317.1 m	61.8 m / 18.4 m	61.8 m / —
EnKF update (S)	8.6 m	136.7 m	8.6 m	8.6 m
Two-way-tracking (S)	—	—	12.8 m	12.8 m
Inflation (S)	—	—	—	2.3 m
Total Time (S/P)	70.4 m / —	1012.6 m / 458.3 m	83.2 m / 39.8 m	85.5 m / —

After the assimilation of the measurements from 09:40 to 11:10 UTC, the forecasts at 12:00 based on the EnKF using ensemble sizes of 50 and 500 (abbreviated as EnKF[50] and EnKF[500]) are shown in Fig. 5.1**c** and 5.1**d**, respectively. Due to the accumulation of spurious covariances in $\mathbf{P}^f[50]$, Fig. 5.1**c** strongly deteriorates compared to 5.1**d**, especially for the plume in Norway and North Sea. Therefore, the sampling errors in EnKF[50] have a large effect on the forecasts and are likely to deteriorate the accuracy. In this chapter, the terms EnKF[50] and EnKF[500] represent the EnKF implementations without covariance localization. Note that for large scale three-dimensional atmospheric assimilation, it is usually unrealistic to employ an ensemble size over 100 because of the large computational cost (Nerger and Hiller, 2013; Barbu *et al.*, 2009). This can also be confirmed by Table 5.1 which lists the computational time of EnKF[50] (Fig. 5.1**c**) and EnKF[500] (Fig. 5.1**d**).

5.2.2. Characteristics of physical forecast error covariances

An efficient localization should mimic the patterns of the error covariances. In this section, we will therefore study these patterns in more details. We will use $\mathbf{P}^f[500]$ as a proxy for the true covariances.

Anisotropic

Two-way-anisotropic

To investigate the properties of $\mathbf{P}^f[500]$, Fig. 5.2**a** is the zooming-in of Fig. 5.1**b**. Based on Fig. 5.2**a**, the first impression of $\mathbf{P}^f[500]$ is that it is "anisotropic", i.e., the covariance shape and spread varying in different directions. This implies that a proper localization function **f** does not only depend on the distance, but should have a structure varying over space.

Because there is only one emission point (at the volcano) for volcanic ash application, all the ashes in atmospheres are transported by the directional wind drive from the same source point. As a result, the anisotropic structure of the forecast error covariances is directional along the wind forcing (i.e., directionally anisotropic).

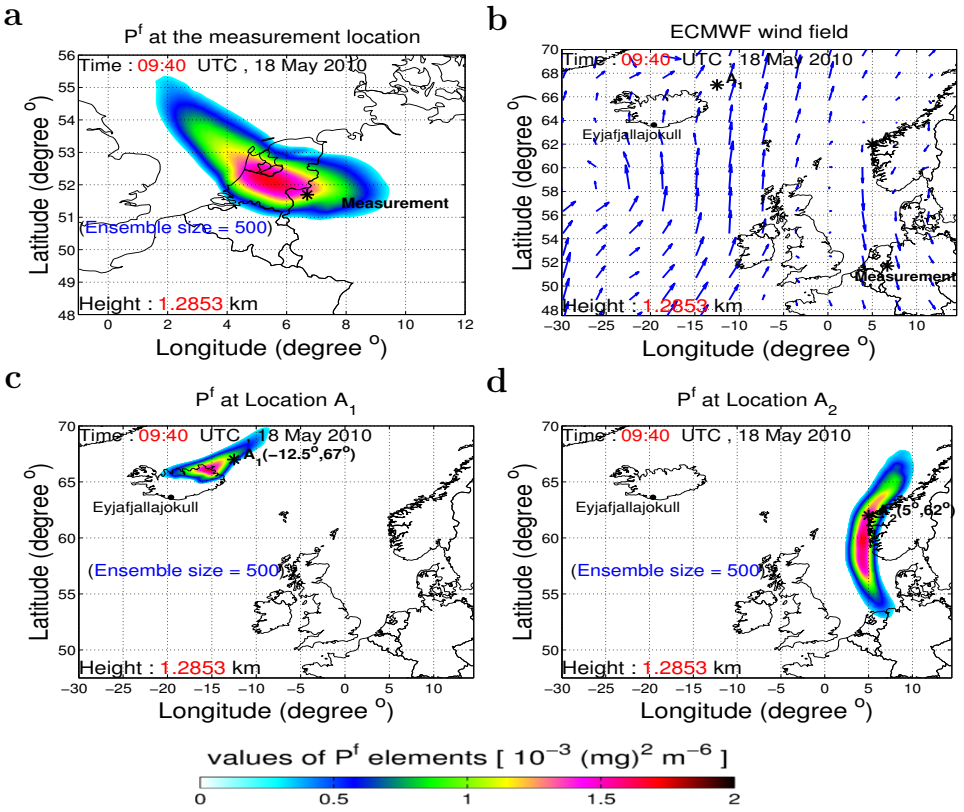

Figure 5.2: **Characteristics of the forecast error covariances. a** is the zooming-in version of Fig. 5.1**b**, showing the detailed structure. **b** is the actual ECMWF wind field. **c** and **d** illustrate the forecast error covariances corresponding to the location (-12.5°, 67°, 1.2853 km) and (8°, 67°, 1.2853 km), respectively.

This can be confirmed by comparing the structure of $\mathbf{P}^f[500]$ (Fig. 5.2**a**) with the corresponding ECMWF wind field (Fig. 5.2**b**). The comparison shows that the forecast error covariances are two-way prominent (northwest-southeast), which is in agreement with the wind southeast direction at the measurement location.

It is also observed that the forecast error covariances in Fig. 5.2**a** tends to be more in a northwest direction than in the other directions. In many cases we observed the covariances to be upwind-dominant. Physically, this makes sense because (1) errors reduced by assimilation propagate downstream, so that subsequent observations require larger updates upstream; (2) the ash concentrations are reduced over time, so that larger concentrations and covariances are expected upstream. To examine whether this phenomenon is generally correct, two other locations $\mathbf{A}_1$(-12.5°, 67°, 1.2853 km) and $\mathbf{A}_2$(5°, 62°, 1.2853 km) are chosen to illustrate the forecast error covariances $\mathbf{P}^f[500]$, as shown in Fig. 5.2**c** and 5.2**d**. Compared to another upwind-dominant covariance structure in Fig. 5.2**c**, the forecast covariances shown in Fig. 5.2**d** are actually "downwind-dominant". Therefore, based on these evidences, generally the two-way-anisotropic forecast error covariances are not always "upwind-dominant" or "downwind-dominant", but do include both upwind and downwind covariances at the same time.

Standard-deviation-dependent

The previous results showed that the forecast error covariances are "two-way-anisotropic", but it is not yet clear how to define a proper localization matrix to capture both upwind and downwind covariances. The upwind covariances during assimilation arise from the wind fields that drive the forward model, thus a backward model driven by the reversed wind field (reversing the actual wind direction) is the key for tracking the upwind covariance structures. Similarly, the downwind covariances at the current time are due to the forward model run in the past time, thus the forward model run from a specified past time to the present time is essential for capturing the downwind covariance structures. Therefore, combining forward and backward tracking, the downwind and upwind covariance structures are aimed to be captured. However, the current investigation is not sufficient for accurate tracking, because the two-way covariances are not constant or regular but varied spatially and temporally, i.e., sometimes "upwind-dominant" or "downwind-dominant" or possibly "upwind-downwind-equivalent".

Thus, to accurately capture the covariances in both directions, further information or other covariance characteristic must be investigated and included, so that the tracked covariance structures can be automatically scaled to reveal the actual (e.g., upwind- or downwind-dominant) covariance structures. For this investigation, the key point is to understand why the covariances are sometimes upwind-dominant or downwind-dominant. We take Fig. 5.2**a** for example, where the upwind-dominant phenomenon is shown in the forecast error covariances. Although it is the covariances on which the localization is applied, it remains very interesting to also check the properties of the correlations and the forecast error standard deviations, which usually helps to understand the reason behind its structure.

The sampled forecast error standard deviations ($\mathbf{Std}^f[500]$) are equivalent to the square root of the diagonal values of $\mathbf{P}^f[500]$. The correlations ($\mathbf{Cor}^f$) between

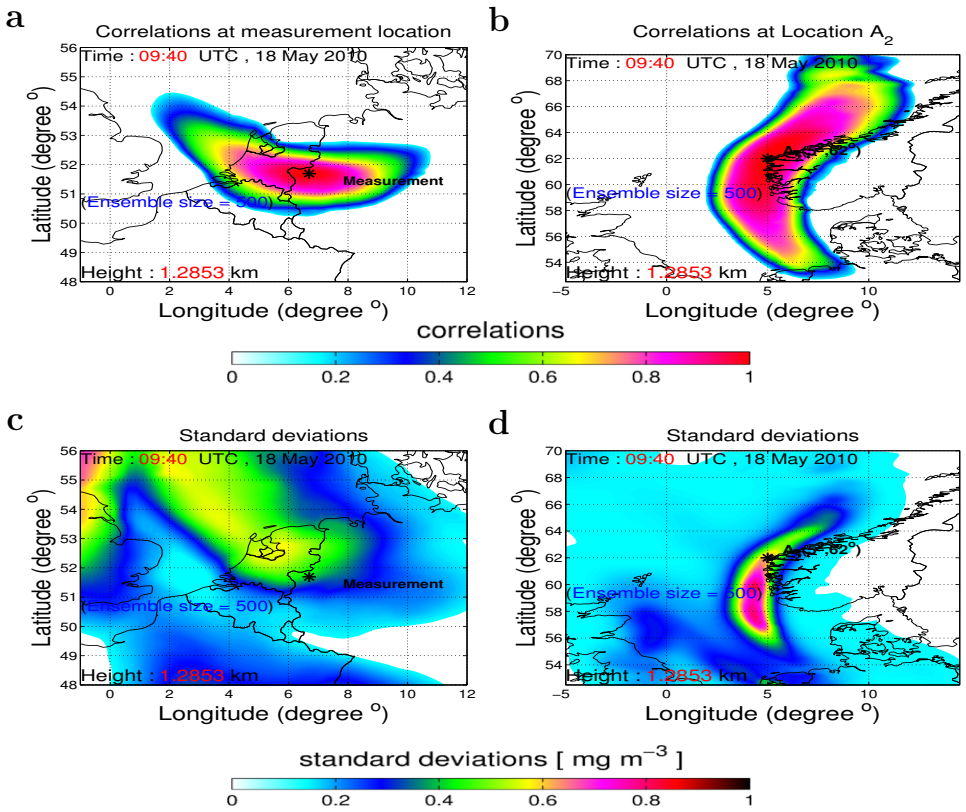

Figure 5.3: **Correlations and standard deviations.** **a**,**c** illustrate the correlations, standard deviations at the measurement location. **b**,**d** illustrate the correlations, standard deviations at A_2 (5°,62°,1.2853 km).

ash state variables at two locations $\mathbf{A}_i$ and $\mathbf{A}_j$ can be numerically estimated by

$$\mathbf{Cor}^f(\mathbf{A}_i, \mathbf{A}_j) = \frac{\mathbf{P}^f[500](\mathbf{A}_i, \mathbf{A}_j)}{\mathbf{Std}^f[500](\mathbf{A}_i) \cdot \mathbf{Std}^f[500](\mathbf{A}_j)}. \tag{5.1}$$

Fig. 5.3a and 5.3c illustrate the the correlations (based on Eq. (5.1)) and the sampled (500) standard deviations at the measurement location. The "upwind-dominant" structure does not occur in the correlations, but does occur in the standard deviations. It is revealed that the correlations are flow-dependent and two-way-anisotropic, without obvious directional preferences (upwind- or downwind-dominant). This correlation structure makes sense, since it is in an agreement with the physical correlation meaning, i.e., in the past time, the concentration at one fixed location was not only contributed by the upwind state variables, but also contributing the variables in the downwind direction.

Although the correlation structure is more or less equivalent in the upwind and downwind directions, the standard deviations have a clear upwind-dominant tendency at the measurement location. Thus, the key to explain the "upwind-dominant" covariances is not correlations, but the standard deviations, which reveals that the other characteristic of the forecast error covariances is "standard-deviation-dependent". This claim is confirmed by another check on the correlations (Fig. 5.3b) and the standard deviations (Fig. 5.3d) at the location $\mathbf{A}_2$(5°, 62°, 1.2853 km). The correlations shown look "symmetric" and the standard deviations tend to be more in the downwind direction, which is consistent with the "downwind-dominant" covariances shown in Fig. 5.2**d**.

We here give some explanations why the standard deviations are sometimes downwind- decreasing or increasing. For our one-source application, once the ashes are erupted into atmospheres, they start to be transported by the downwind drive, thus for concentrations from the same eruption episode (with similar eruption rates), the standard deviations (directly related to concentrations) are in a downwind-decreasing tendency. However, for concentrations from different episodes when latter eruption rate is much smaller than former, the standard deviations are actually in an increasing trend in the downwind direction.

5.3. EnKF with two-way-tracking covariance localization (TL-EnKF)

"Two-way-anisotropy" and "standard-deviation-dependence" have been investigated as two characteristics of the forecast error covariances. By considering these two characteristics, we propose a new approach to define the localization matrix for accurate covariance localization during volcanic ash assimilation. Here we adopt a two-way tracking to capture the covariance structures between each individual measurement and the state variables. The EnKF using Two-way-tracking covariance Localization (TL) is abbreviated with TL-EnKF.

The localized forecast error covariances are built in every analysis step, and we define the localization matrix **f** for covariance localization in five steps.

(1) Forward track the downwind correlations.

In the forecast step from time t_{k-1} to t_k, each ensemble member is propagated using the model dynamics M_{k-1}. After the model has been propagated from the time t_i to t_k (t_i is a time prior to t_k and $k \geq i+1$), the model dynamics over these time steps can be represented with

$$M_{i\to k} = M_{k-1}(M_{k-2}(\cdots M_{i+1}(M_i))). \tag{5.2}$$

According to Section 2.1, M_{k-1} can be represented as the summation of three parts, i.e., advection ($\mathbf{A}$), diffusion ($\mathbf{F}$), sink ($\mathbf{S}$) including deposition and sedimentation, and emissions ($\mathbf{E}$). In the formation of an forward operator to track the downwind correlations at the flight measurement location, we don't consider the near-volcano regions (<100 km from the volcano), because aircraft measurements cannot be performed in these regions due to safety considerations (Marenco *et al.*, 2011). For other regions (i.e., distal parts which are >100 km from the volcano), for example Marenco *et al.* (2011) and Fu *et al.* (2015) have shown that the dominated processes are the advection and diffusion. Thus the sink processes such as deposition and sedimentation are probably small compared to the advection and diffusion. We will therefore not explicitly calculate $\mathbf{S}$, but assume that it is zero. Therefore, the formed forward operator $M_{i\to k}^{fwd}$ equals to $M_{i\to k}$ ignoring the sink $\mathbf{S}$:

$$M_{i\to k}^{fwd} = M_{k-1}^{fwd}(M_{k-2}^{fwd}(\cdots M_{i+1}^{fwd}(M_i^{fwd}))), \tag{5.3}$$

where $M_{k-1}^{fwd} = \mathbf{A} + \mathbf{F} + \mathbf{E}$.

The forward operator $M_{i\to k}^{fwd}$ is can be determined if the source term $\mathbf{E}$ is given. Thus, for the source term at time t_i, we only put a constant value α (e.g., α=1 mg m^{-3} in this chapter) for ash_5 at the measurement location, ignoring the ash state variables in all the other locations. Then run the model from t_i to t_k forward by

$$\mathbf{Z}_{i\to k}^{fwd} = M_{i\to k}^{fwd}(\mathbf{z}^{fwd}), \tag{5.4}$$

where $\mathbf{z}^{fwd}$ is the vector, with a dimension of the state number (i.e., 180×200×18×6 here, see Section 2.1), containing one non-zero value (α mg m^{-3}) corresponding to one state variable at the measurement location at t_k. From this we compute a scaled version with values in [0,1] (which represents the downwind correlations):

$$\mathbf{Z}_{i\to k}^{fwd,scaled} = \frac{\mathbf{Z}_{i\to k}^{fwd}}{max(\mathbf{Z}_{i\to k}^{fwd})}. \tag{5.5}$$

(2) Backward track the upwind correlations:

For the backward track, the adjoint of the tangent linear approximation of the forward model needs to be used in this step. The forward model operator in volcanic ash transport (i.e., M_{k-1}) is nonlinear. This is because the LOTOS-EUROS employs the advection scheme proposed by Walcek and Aleksic (1998), the advection part $\mathbf{A} = -\nabla\cdot(\mathbf{u}\cdot\mathbf{c}_s)$ of M_{k-1} (see Section 2.1) is nonlinear. In addition, because

the sink ($\mathbf{S}$) such as the deposition and sedimentation scheme for volcanic ash removals is complicated and relies on a combination of several parameters (Fu *et al.*, 2015), thus the part $\mathbf{S}$ is also nonlinear. Therefore, due to the nonlinearity of the forward model operator M_{k-1}, the adjoint of the tangent linear approximation of M_{k-1} cannot easily be developed, as discussed by Errico (1997).

In this chapter, we will not implement the adjoint model. Instead, we approximate the adjoint using a practical approach. We define the backward operator M_{k-1}^{bck} to approximate the adjoint operator. This is implemented by reversing the time steps to calculate the backward advection $\mathbf{A}^{bck}$ and the backward diffusion $\mathbf{F}^{bck}$ using the backward wind field. This approach in atmospheric science to get an adjoint operator is only correct in the linear case (Errico, 1997). Therefore, the suggested backward approach is actually an approximation of the adjoint approach. Note that we don't explicitly calculate $\mathbf{S}^{bck}$ (the backward $\mathbf{S}$), but also assume that it is zero (as we deal with $\mathbf{S}$ in the step (1)).

To summarize, the backward operator is formulated as:

$$M_{k\to i}^{bck} = M_{i}^{bck}(M_{i+1}^{bck}(\cdots M_{k-2}^{bck}(M_{k-1}^{bck}))), \tag{5.6}$$

where $M_{k-1}^{bck} = \mathbf{A}^{bck} + \mathbf{F}^{bck} + \mathbf{E}^{bck}$ and $\mathbf{E}^{bck}$ is a given source term for backward operator. Therefore, the backward operator is formulated practically using the model dynamics and related meteorology (wind field). The backward operator is aimed to roughly capture the upwind correlation patterns.

Since the backward operator $M_{k\to i}^{bck}$ is constructed using Eq. (5.6), the backward track can be determined if the source term $\mathbf{E}^{bck}$ is given. Here $\mathbf{E}^{bck}$ is chosen as another constant value β (e.g., β=1 mg m^{-3} in this chapter). Then run the backward model from t_k to t_i (with a constant source $\mathbf{y}(k)$) by

$$\mathbf{Z}_{k\to i}^{bck} = M_{k\to i}^{bck}(\mathbf{z}^{bck}), \tag{5.7}$$

where $\mathbf{z}^{bck}$ and $\mathbf{z}^{fwd}$ are alike, except that the non-zero values are set to β now. We then scale $\mathbf{Z}_{k\to i}^{bck}$ to values in [0,1] (representing the upwind correlations):

$$\mathbf{Z}_{k\to i}^{bck,scaled} = \frac{\mathbf{Z}_{k\to i}^{bck}}{max(\mathbf{Z}_{k\to i}^{bck})}, \tag{5.8}$$

(3) Combine two-way correlations:

After separately tracking the downwind and upwind correlations, the two-way correlations at t_k can be estimated by combining both correlations together:

$$\mathbf{Z} = pmax(\mathbf{Z}_{i\to k}^{fwd,scaled}, \mathbf{Z}_{k\to i}^{bck,scaled}), \tag{5.9}$$

where the operator $pmax$ represents "pairwise maximum", i.e., it compares all the corresponding elements of two vectors $\mathbf{Z}_{i\to k}^{fwd,scaled}$ and $\mathbf{Z}_{k\to i}^{bck,scaled}$, and sets every largest value to $\mathbf{Z}$.

In the two-way track, (at t_k) we start with the ash concentration at the observation location only. After the forward and backward track, the combined domain

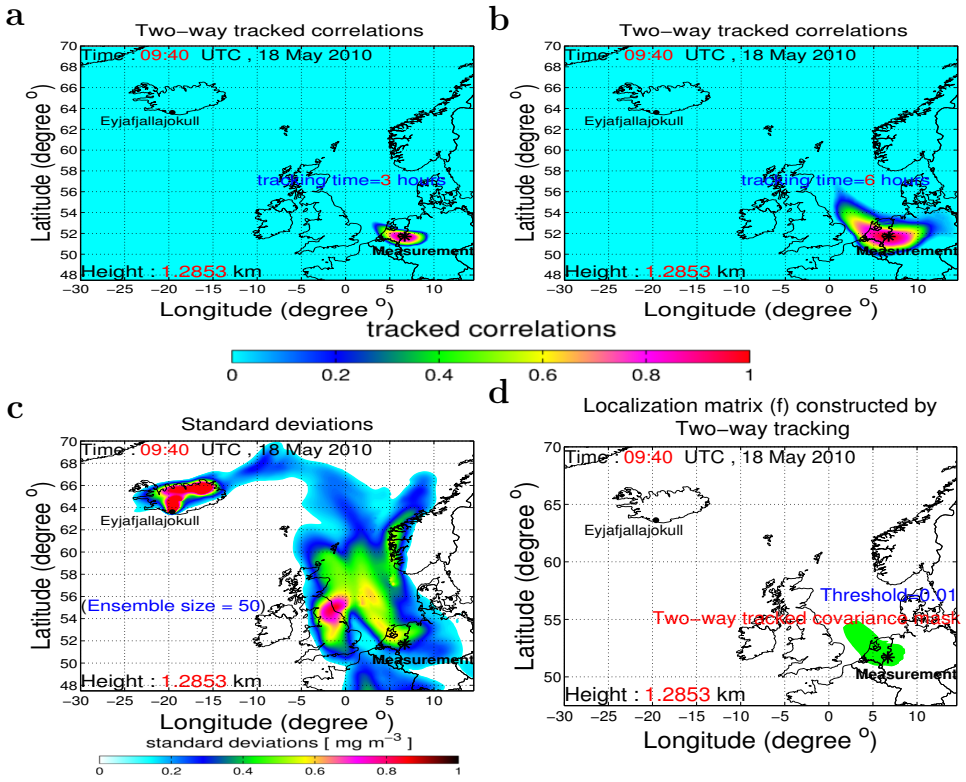

Figure 5.4: **Construct the localization matrix with two-way tracked covariance mask. a** and **b** show the tracked correlations with tracking times of 3 and 6 hours, respectively. **c** shows the standard correlations (at a small ensemble size of 50) used for inclusion in the tracked correlations. **d** is the construted covariance mask created at a threshold of 0.01.

where the particles are transported is considered as the region where one measurement may have influences. Here, t_k and t_i are respectively the start/end time and the end/start time for the backward/forward track. Fig. 5.4**a** and 5.4**b** show the two-way tracked region with different tracking times. Compared with the estimated correlation structures (at an ensemble of 500) at 09:40 as shown in Fig. 5.3**a**, the case with the tracking time of 6 hours (Fig. 5.4**b**) is shown to agree best with the coverage of the physical correlations. Therefore, 6 hours is employed in this chapter as the two-way tracking time. Note that we only do once the two-way track at each assimilation cycle, because one aircraft can only fly at one location at each time. If we have two aircrafts to measure at the same time, we then need to do the two-way-tracking calculation twice.

(4) Include standard deviations:

Since the localization is applied on the covariances, to have the tracked correlations $\mathbf{Z}$ only is not enough. The covariances' "standard-deviations-dependent" characteristic has been revealed in Section 5.25.2.25.2.2. The tracked correlations are "two-way-anisotropic" but have no preferences on upwind or downwind directions (kind of "symmetric"). However, the standard deviations have clear concentration differences around the flight measurement location, which determines the covariances' directional strength.

The standard deviations at a small ensemble size of N_s (here N_s=50) can be obtained by

$$\mathbf{Std}^f[N_s] = \sqrt{\text{diag}(\mathbf{P}^f[N_s])}, \tag{5.10}$$

where the operator "diag" gets the diagonal values of the covariance matrix $\mathbf{P}^f[N_s]$ and forms a vector with the dimention of the state number. Fig. 5.4**c** illustrates $\mathbf{Std}^f[50]$. Although $\mathbf{Std}^f[50]$ is not as accurate as $\mathbf{Std}^f[500]$, its accuracy is capable of providing the assistance to indicate the covariances' directional strength. We next create the $\mathbf{Std}$-based correlations by

$$\mathbf{Z}^{std} = \frac{\mathbf{Z} \circ \mathbf{Std}^f[N_s]}{max(\mathbf{Z} \circ \mathbf{Std}^f[N_s])}. \tag{5.11}$$

(5) Create a covariance mask for localization:

Next, we create a mask at a threshold (γ):

$$\widehat{\mathbf{Z}}^{std} = \begin{cases} 1, & where \quad \mathbf{Z}^{std} > \gamma \\ 0, & where \quad \mathbf{Z}^{std} \leq \gamma. \end{cases} \tag{5.12}$$

After a careful check on different thresholds of $\widehat{\mathbf{Z}}_k^{std}$, we find the locations where the scaled values larger than a threshold of 0.01 (γ=0.01 in this chapter) are concentrated in a rather small region (see Fig. 5.4**d**). The rest of the domain can be cut off because $\widehat{\mathbf{Z}}^{std} \leq 0.01$ can hardly influence the localization matrix $\mathbf{f}$. Therefore, the region (locations with $\widehat{\mathbf{Z}}^{std} > 0.01$) can be captured and taken as the localization region where one aircraft in situ observation at each flight location can really affect.

The created covariance mask $\widehat{\mathbf{Z}}^{std}$ is equivalent to $\mathbf{fH}^T$, where $\mathbf{f}$ is the localization matrix as described in Eq. (2.9)). Note that for practical implementation, we do not compute $\mathbf{f}$ complete, but only the column ($\mathbf{fH}^T$) corresponding to the grid cell with the observation; thus in fact we only need to compute $\widehat{\mathbf{Z}}^{std}$. With $(\mathbf{fH}^T) \circ (\mathbf{P}^f\mathbf{H}^T)$, i.e. $(\mathbf{f} \circ \mathbf{P}^f)\mathbf{H}^T$ in Eq. (2.9), the sampled forecast error covariance matrix $\mathbf{P}^f$ can be cut off corresponding to the locations only in the localized region, and then a localized Kalman gain can be calculated, and further the analysis step is completed.

5.4. Experimental Results with TL-EnKF

5.4.1. Performance in capturing the physical forecast error covariances

The concept of TL-EnKF has been formulated in Section 5.3. The effect of the two-way-tracking localization in capturing the physical structures of the forecast error covariances will be investigated through experiments.

In TL-EnKF[50], using the localization matrix $\mathbf{f}$ defined based on the two-way track, the localized forecast error covariance matrix (i.e., $\mathbf{f} \circ \mathbf{P}^f[50]$) is illustrated in Fig. 5.5**a**. Compared to Fig. 5.1**a** ($\mathbf{P}^f[50]$), the spurious covariances are significantly removed by the tracked localization matrix. On the other hand, through the comparison with Fig. 5.5**b** (i.e., the referenced physical error covariances $\mathbf{P}^f[500]$), Fig. 5.5**a** achieves a similar performance, indicating that the physical covariance structures can indeed be well captured by the two-way-tracking localization. Note that the covariance structures captured by TL-EnKF[50] are not exactly the same as that in EnKF[500] but the basic shape of the physical covariances are well kept.

Using the localized forecast error covariance matrix, the first analysis result (at 09:40 UTC, 18 May, 2010) with TL-EnKF[50] is checked in Fig. 5.5**c**. As expected, based on the well captured error covariances, TL-EnKF[50] performs comparable as EnKF[500] does (only a slight difference can be visualized at areas around (1°,55°)).

The performance of TL-EnKF[50] at another time 10:10 UTC, 18 May, 2010 is also evaluated. Based on the tracked localization matrix $\mathbf{f}$ (Fig. 5.6**a**) and the forecast error covariance matrix $\mathbf{P}^f[50]$ (Fig. 5.6**b**), the Schur products of both are conducted in Fig. 5.6**c**. Compared to the approximated physical forecast error covariances as illustrated in Fig. 5.6**d**, TL-EnKF[50] is observed to be able to maintain most of the physical covariances. Note that there are also some clear differences between Fig. 5.6**c** and 5.6**d**, which are due to the accumulation of sampling errors of TL-EnKF[50]. By studying on the analysis results shown in Fig. 5.6**e** and Fig. 5.6**f**, TL-EnKF[50] is shown to be a good approximation to EnKF[500].

TL-EnKF[50] has been shown to be capable of maintaining the physical covariances at each analysis step during assimilation from 09:40 UTC to 11:10 UTC. We now evaluate the forecast, Fig. 5.7**a** shows the forecast at 12:00 UTC using TL-EnKF[50], which appears to approximate the reference (Fig. 5.7**b**, estimated using EnKF[500]) with a high accuracy. The agreement between TL-EnKF[50] and EnKF[500] confirms that the accumulated inaccuracies of TL-EnKF[50] are actually very small and acceptable. It also shows that the constructed covariance mask $\widehat{\mathbf{Z}}^{std}$ (defined in Eq. (5.12)) can indeed roughly capture the covariance patterns

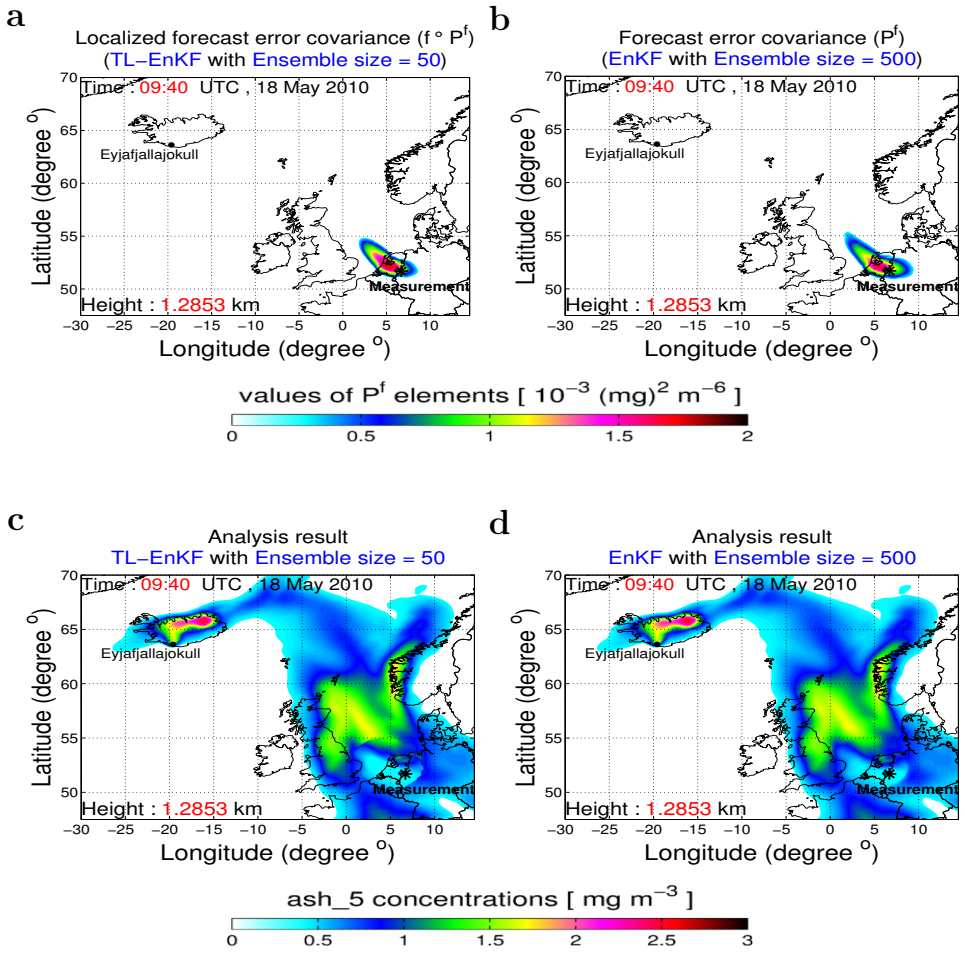

Figure 5.5: **Performance of TL-EnKF. a** is an illustration of the localized forecast error covariances in TL-EnKF[50]. **b** is the reference to the physical ("real") forecast error covariances, estimated by EnKF[500]. **c** is the first analysis result with TL-EnKF[50] at 09:40 UTC, 18 May, 2010. **d** is the first analysis result with EnKF[500].

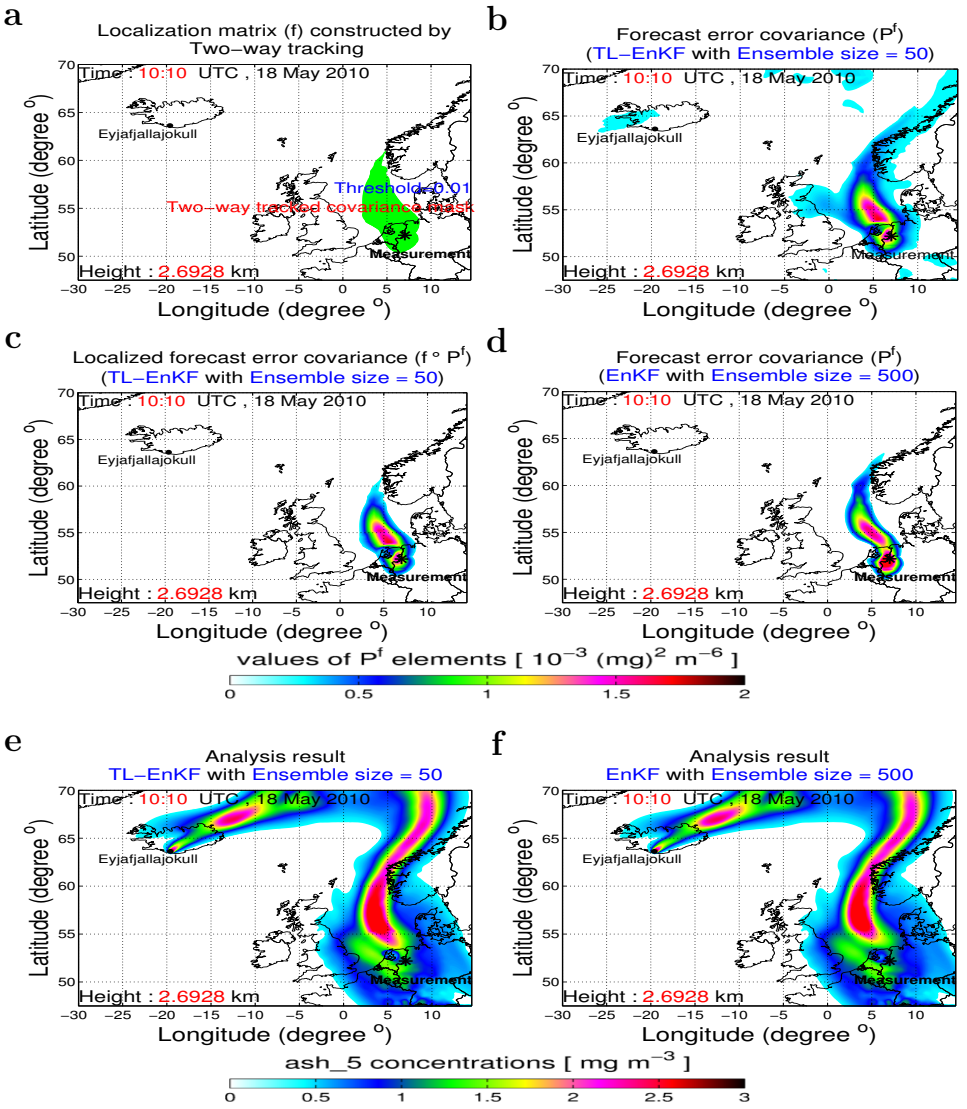

Figure 5.6: **Performance of TL-EnKF[50] at the time 10:10 UTC, 18 May, 2010.** **a** shows the two-way tracked covariance mask at this time. **b** illustrates the forecast error covariances of TL-EnKF[50] corresponding to the current measurement and current time. **c** is an illustration of the localized forecast error covariances in TL-EnKF[50]. **d** illustrates the physical forecast error covariances, estimated by EnKF[500]. **e** is the analysis result with TL-EnKF[50] at 10:10 UTC. **f** is the analysis result with EnKF[500] at this time.

with an acceptable accuracy. Although $\hat{\mathbf{z}}^{std}$ may not be very accurate, its accuracy is indicated as satisfactory because it is only used for constructing the domain for the localization procedure.

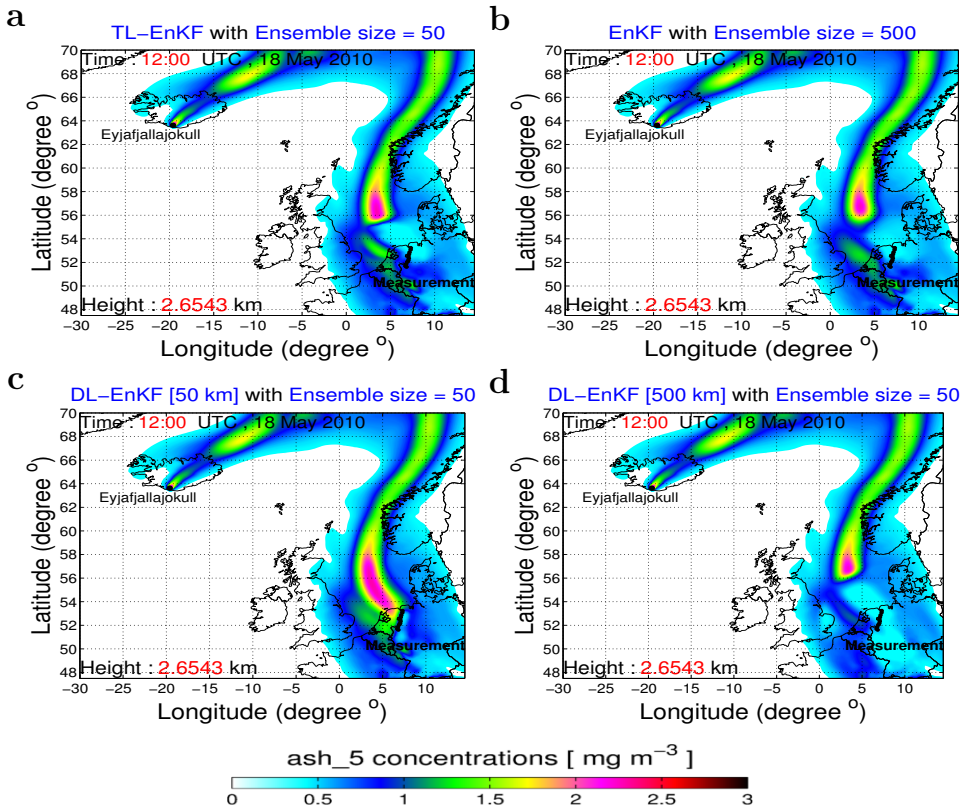

Figure 5.7: **Comparison between TL-EnKF and the EnKF with a distance-based covariance localization (DL-EnKF). a** is the forecast at 12:00 UTC, 18 May, 2010 with TL-EnKF[50]. **b** is the forecast with EnKF[500]. **c** is the forecast with DL-EnKF[50,50 km], where the filtering length scale is chosen at 50 km. **d** is the forecast with DL-EnKF[50,500 km].

5.4.2. Comparison between TL-EnKF and EnKF with distance-based localization (DL-EnKF)

According to the results above, the two-way-tracking localization approach is shown to be a proper and accurate covariance localization for the application of volcanic ash assimilation. How does it perform comparing to the other localization approaches? Currently, in atmospheric applications, the most commonly used covariance localization is distance-based localization (DL), where the localization matrix **f** is defined by applying an "isotropic" structure to the Euclidean distance between two points. The values decrease to zero beyond a certain distance. For some applications (e.g., ozone, CO_2, sulfur dioxide), this approach (DL-EnKF) has obtained acceptable per-

formances (in maintaining most of the physical covariances) with a simple setup using a constant localization parameter (Curier *et al.*, 2012; Chatterjee *et al.*, 2012; Barbu *et al.*, 2009).

While, in the TL-EnKF approach, the localization matrix **f** is obtained directly based on the model's physics ("two-way-anisotropy" and "standard-deviation-dependence"). The two-way-tracking approach works because it is designed to track the physical covariance structures as many as possible. Therefore, based on previous results, one would not argue the efficiency of TL-EnKF for volcanic ash assimilation, but may wonder whether DL-EnKF can also have a similar or an acceptable performance.

For this investigation, the performances of DL-EnKF[50] are shown in Fig. 5.7**c** and 5.7**d**, where without loss of generality, 50 km and 500 km are respectively chosen as the constant filtering length scale. Compared to EnKF[500], the effect of DL-EnKF[50,50 km] is rather little (only in small areas around the measurement route) and DL-EnKF[50,500 km] appears to largely over-correct the concentrations (especially in regions of South Netherlands and Belgium). This directly implies that DL-EnKF has poorer performances in dealing with sampling errors and it is likely to deteriorate the accuracy.

Although DL-EnKF is not a good choice compared to TL-EnKF, it is interesting in future to investigate some other variants of DL-EnKF (e.g., with adaptive radius or radius based on various distance-based functions) might achieve an acceptable performance to well maintain the "two-way-anisotropic" and "standard-deviation-dependent" covariances during assimilation.

5.4.3. Combination with covariance inflation

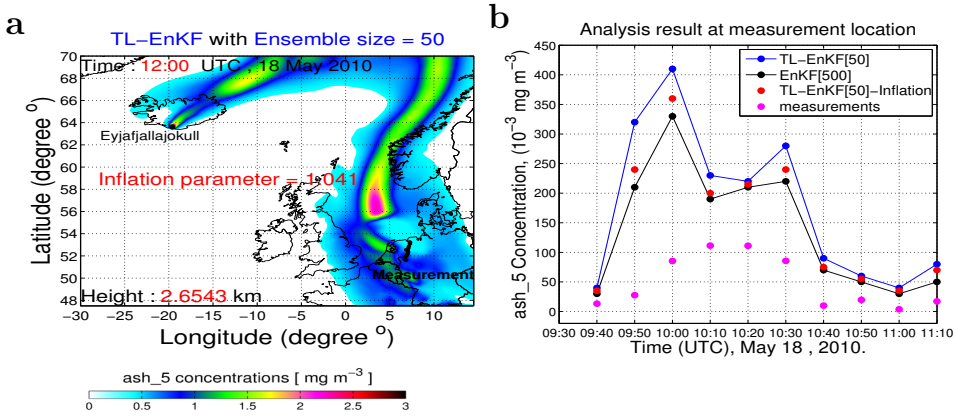

Figure 5.8: **Impact of covariance inflation. a** is the forecast at 12:00 UTC, 18 May, 2010 using TL-EnKF[50] combined with covariance inflation (inflation factor is chosen at 1.041). **b** shows the analysis results at the measurement locations using TL-EnKF[50]-Inflation.

Covariance localization (either TL or DL) helps to improve the estimates of the forecast error covariances by cutting off the spurious covariances using the defined

localization matrix. However, the under-sampling still exists in the localized error covariances, which is commonly known to cause the underestimation problem (Houtekamer and Mitchell, 1998).

Covariance inflation, introduced by Anderson and Anderson (1999), is an approach to correct the problem of underestimation in the sampled forecast error covariance matrix. This approach is a useful technique and now is commonly used in ensemble-based data assimilation (Evensen, 2009). The principle of the covariance inflation procedure is to simply increase the forecast error covariances by an inflation factor ρ, which negates the systematic underestimation in each assimilation step. The inflation factor is used to replace the forecast ensemble according to Eq. (5.13),

$$\boldsymbol{\xi}_j^f = \rho(\boldsymbol{\xi}_j^f - \mathbf{x}) + \mathbf{x}, \tag{5.13}$$

where ρ is the inflation factor and is usually chosen, based on experience, to be slightly larger than 1.0 (typically 1.01). For applying covariance inflation in our application, we can actually estimate an inflation factor based on Eq. (5.14),

$$\rho = \frac{S_{\mathbf{P}^f[500]}}{S_{\mathbf{f}\circ\mathbf{P}^f[50]}}, \tag{5.14}$$

where the estimate of the physical error covariances $\mathbf{P}^f[500]$ is included in the calculation. $S_{\mathbf{f}\circ\mathbf{P}^f[50]}$ represents the summation of all the elements in the localized forecast error covariance matrix $\mathbf{f}\circ\mathbf{P}^f[50]$ as used in TL-EnKF[50], while $S_{\mathbf{P}^f[500]}$ calculates the summation of the elements in $\mathbf{P}^f[500]$ as used in EnKF[500]. ρ is estimated only at the time 09:40 UTC and is used for all the following assimilation cycles. According to Eq. (5.14), ρ is calculated to be 1.041.

Fig. 5.8**a** shows the performance of TL-EnKF together with covariance inflation (termed as TL-EnKF-Inflation). Visually we find no clear improvements compared to the performance with TL-EnKF (Fig. 5.7**a**), so that one may confuse where the effect of covariance inflation is. Therefore, we carefully check the analysis result at each measurement location along all the assimilation time. The result (see Fig. 5.8**b**) shows TL-EnKF[50]-Inflation performs better than the case without inflation and the correction of the ash concentrations is shown to be more accurate (i.e., the values are closer to TL-EnKF[500]). Based on this investigation, although the effect of covariance inflation is not as strong as that of covariance localization (two-way-tracking), its positive influence indicates it can be included as an additional improvement to TL-EnKF. We may expect when extensive aircraft measurements are available, the direct correction at the measurement locations could lead to a much wider improvement.

5.4.4. Computational evaluation

According to the discussions above, we have shown the capability of TL-EnKF in maintaining the physical covariances with a rather small ensemble size. Next, another question remains to be answered is what is the computational cost of TL-EnKF

since now a two-way-tracking module is embedded. The EnKF with an ensemble size of 500 is considered improper due to its large computational cost for large scale model, thus it will be no practical use if the computational cost of TL-EnKF is also large.

Table 5.1 shows the computational time of TL-EnKF[50] and EnKF[500], where the computational costs of both serial and parallel cases are reported [1]. In the serial case, the EnKF forecast step is performed on one processor which means the ensembles are forecasted one by one, while in the parallel case, the forecast step is performed in parallel on multi-processors which means the ensembles are propagated at the same time.

It is shown in the serial case that TL-EnKF[50] obtains a big acceleration (13 times) over EnKF[500]. This is mainly because it is realized with a small ensemble size of 50. The additional computation cost for the extra module (two-way-tracking) is quantified as 18% based on Table 5.1 by ($\frac{12.8}{70.4}$, 70.4 m is the time of EnKF[50]), while the additional cost for the increased ensemble size is quantified as 1338% by ($\frac{1012.6-70.4}{70.4}$). Thus, although the additional two-way-tracking module takes some extra computation, its impact (18%) is far smaller than the large ensemble size (1338%) required by EnKF[500].

It is known that EnKF can easily be parallelized in the forecast step, thus it is possible that the computational cost of the parallelized EnKF[500] is equivalent to the parallelized TL-EnKF[50]. Therefore, we also compare the computational cost of the parallel cases (the number of processors used is equal to the ensemble size) in Table 5.1. For the parallel implementations, different ensemble members run on different processors, thus the ensemble forecasts are performed simultaneously. Note that here we employ the commonly used parallelization, i.e., performing the forecast of all ensemble members simultaneously. This means the parallelization does not go as deep as for example to the matrix level in the analysis step which currently is a difficult aspect for EnKF parallelization (Tavakoli *et al.*, 2013). We can see both TL-EnKF[50] and EnKF[500] obtain accelerations with their parallel implementations. The EnKF[500] shows a larger speedup than TL-EnKF[50] because it has a much larger ensemble size and subsequently uses much more processors. However, the parallelized TL-EnKF[50] is still 11 times faster than parallel EnKF[500].

Based on the results of this experiment, we can say the proposed TL-EnKF has an acceptable computational cost. In addition, the adding cost of the inflation process is also examined in Table 5.1 and is evaluated as only 3%($\frac{2.3}{70.4}$), thus TL-EnKF combined with covariance inflation is also computationally efficient.

5.5. Conclusion

In this chapter on volcanic ash assimilation, the aim was to design an accurate localization matrix for covariance localization to maintain the correctly specified physical forecast error covariances and remove as many of the spurious covariances as possible. As a reference, the physical ("real") forecast error covariances were

[1] The results are obtained from the Bullx B720 thin nodes of the Cartesius cluster, which is one computing facility of SURFsara, the Netherlands Supercomputing Center. Each node is configured with 2 × 12-core 2.6 GHz Intel Xeon E5-2690 v3 (Haswell) CPUs and with 64 GB memory.

first approximated as accurate as possible by the sampled forecast error covariance matrix using an ensemble size of 500.

The structure of the forecast error covariances was investigated directional along the wind forcing, but sometimes "upwind-dominant" or "downwind-dominant" or possibly "upwind-downwind-equivalent". By checking the estimated (at an ensemble size of 500) correlations and standard deviations, the latter is revealed as the key to represent the directional strength of the covariances. Therefore, "two-way-anisotropic" and "standard-deviation-dependent" characteristics were concluded as the two most important properties of the physical forecast error covariances.

Motivated by these analysis, a two-way-tracking approach was proposed to define the localization matrix (for covariance localization), aiming at accurately capturing the specified physical covariances. The forward model was used to track the downwind correlations during the past time. The approach of tracking the upwind correlations was essentially based on the adjoint model to trace the sensitivities of the state with respect to the measurement backwards in time. However, the adjoint was approximated in a practical way using a backward simulation of the original model. In the two-way-tracking formulation, we only considered the model processes of advection and diffusion. This consideration is consistent with the reality that, in the distal part of an ash plume, the advection and diffusion are the dominant processes. After the correlations were two-way tracked, the information of the standard deviations was further included. Finally, a covariance mask required for the localization matrix was created.

According to the experimental results, the two-way-tracking localization (TL) approach was examined and verified as a proper and accurate covariance localization for the application of volcanic ash assimilation. Although our case study showed TL successfully captured the "upwind-dominant" covariances, TL can also work for other types of covariance structures (e.g., "downwind-dominant") because the information of standard deviations was explicitly included in the method. The forecast performance with TL-EnKF was shown to be comparable with the referenced (with a much larger ensemble size) EnKF performance. It indicates that the accumulated inaccuracies of TL-EnKF in approximating the physical error covariances are actually small and acceptable. It also showed that the formulated two-way-tracked covariance mask can roughly capture the covariance patterns with an acceptable accuracy, because it is only used for constructing the domain for the localization procedure. Additionally, it has been shown that the additional computational cost of TL-EnKF is very modest when compared with the referenced EnKF both in serial or parallel cases.

Distance-based localization (DL), the commonly used covariance localization approach, was also performed as comparisons with TL. The experimental results showed that the effect of DL-EnKF either is very small (with a small filtering length scale) or largely over-corrects the concentrations (with a large filtering length scale). Although DL-EnKF is not accurate in dealing with sampling errors compared to TL-EnKF, some other variants of DL-EnKF (e.g., with adaptive radius or radius based on various distance-based functions) might be expected to achieve an acceptable performance for maintaining the"two-way-anisotropic" and "standard-

deviation-dependent" covariances. An approach to correct the problem of underestimation in the sampled forecast error covariance matrix, covariance inflation was also investigated when embedded in TL-EnKF. The impact of inflation was clearly positive.

6

A mask-state algorithm to accelerate volcanic ash data assimilation

In this chapter, we investigate a strategy for accelerating data assimilation on volcanic ash forecasts. Based on evaluations of computational time, the analysis step of the assimilation is known to be the most expensive part. After a careful study on the characteristics of the ensemble ash state, we propose a mask-state algorithm which records the sparsity information of the full ensemble state matrix and transforms the full matrix into a relatively small one. This will reduce the computational cost in the analysis step.

Experimental results show the mask-state algorithm significantly speeds up the expensive analysis step. Subsequently, the total amount of computing time for volcanic ash data assimilation is reduced to an acceptable level, which is important for providing timely and accurate aviation advices. The mask-state algorithm is generic and thus can be embedded in any ensemble-based data assimilation framework. Moreover, ensemble-based data assimilation with the mask-state algorithm is promising and flexible, because it implements exactly the standard data assimilation without any approximation and it realizes the satisfying performance without any change of the full model.

Parts of this chapter have been published in :
(Fu *et al.*, 2016c): *A mask-state algorithm to accelerate volcanic ash data assimilation*, **Geoscientific Model Development Discussions** 1-19. doi:*10.5194/gmd-2016-208*.

6.1. Introduction

To make the methodology efficient also in an operational (real-time) sense, the computational efforts must be acceptable. For volcanic ash assimilation problems, so far, no studies on the computational aspects have been reported in the literature. Actually, when large amounts of volcanic ash erupted into atmospheres, the computational speed of volcanic ash forecasts is just as important as the forecast accuracy (Zehner, 2010). For example, due to the lack of a fast and accurate forecast system, the sudden eruption of the Eyjafjallajökull volcano in Iceland from 14 April to 23 May 2010, had caused an unprecedented closure of the European and North Atlantic airspace resulting in a huge global economic loss of 5 billion US dollars (Oxford-Economics, 2010). Since then, research on fast and accurate volcanic ash forecasts have gained much attention, because it is needed to provide timely and accurate aviation advices for frequently operated commercial airplanes. It was shown the accuracy of volcanic ash transport can be significantly improved by the assimilation system in (Fu *et al.*, 2016a). Therefore, it is urgent to also consider the computational aspect, i.e., improving the computational speed of the volcanic ash assimilation system as fast as possible. This is the main focus of this chapter.

Due to the computational complexity of ensemble-based algorithms and the large scale of dynamical applications, applying these methods usually introduces a large computational cost. This has been reported from literature on different applications. For example, for operational weather forecasting with ensemble-based data assimilation, Houtekamer *et al.* (2014) reported computational challenges at Canadian Meteorological Center with an operational EnKF featuring 192 ensemble members, using a large 600 $\times$ 300 global horizontal grid and 74 vertical levels. That an initialization requirement of over 7×10^{10} values to specify each ensemble, results in large computational efforts on the initialization and forecast steps in weather forecasting. For oil reservoir history-matching (Tavakoli *et al.*, 2013), the reservoir simulation model usually has a large number of state variables, thus the forecasts of an ensemble of simulation models are often time-consuming. Besides, when time-lapse seismic or dense reservoir data is available, the analysis step of assimilating these large observations becomes very time-consuming (Khairullah *et al.*, 2013). Large computational requirements of ensemble-based data assimilation have also been reported in ocean circulation models (Keppenne, 2000; Keppenne and Rienecker, 2002), tropospheric chemistry assimilation (Miyazaki *et al.*, 2015), and many other applications.

To accelerate an ensemble-based data assimilation system, the ensemble forecast step can be first parallelized because the propagation of different ensemble members is independent. Thus if a computer with a sufficiently large number of parallel processors is available, all the ensemble members can be simultaneously integrated. In the analysis stage, to calculate the Kalman gain and the ensemble error covariance matrix, all ensemble states must be combined together. In weather forecasting and oceanography sciences, Keppenne (2000); Keppenne and Rienecker (2002); Houtekamer and Mitchell (2001) have reported using parallelization approaches to accelerate the expensive analysis stage. In reservoir history matching, a three-level parallelization has been proposed by Tavakoli *et al.* (2013);

Khairullah *et al.* (2013) in recent years, to significantly reduce computational efforts of both forecast and analysis steps due to massive dense observations and large simulation models. The first parallelization level is to separately perform the ensemble simulations on different processors during the forecast step. This approach is usually quite efficient when a large ensemble size is used. However, the scale or model size of one reservoir simulation is constrained by the memory of a single processor. Thus, the second parallelization level is to perform one ensemble member simulation using a parallel reservoir model. These two levels do not deal with the analysis step, which collects all ensemble members to do computations usually on a single processor. Therefore, a third level of parallelization was implemented by Tavakoli *et al.* (2013); Khairullah *et al.* (2013) through parallelizing matrix-vector multiplications in the analysis steps. Furthermore, some other approaches on accelerating ensemble-based assimilation systems, have also been reported, such as GPU-based acceleration (Quinn and Abarbanel, 2011) in Numerical Weather Prediction (NWP), domain decomposition in atmospheric chemistry assimilation (Segers, 2002; Miyazaki *et al.*, 2015). The observations used in an assimilation system can be also optimized with some preprocessing procedures, as reported by Houtekamer *et al.* (2014).

Although for other applications, there were many efforts in dealing with large computational requirements in an ensemble-based data assimilation system, most of them cannot be directly used to accelerate volcanic ash data assimilation. This is because the acceleration algorithms are strongly dependent on specific problems, such as model complexity (high or low resolution), observation type (dense or sparse), primary requirement (accuracy or speed). These factors determine, for a specific application, which part is the most time-consuming, and which part is intrinsically sequential. Thus, no unified approach for efficient acceleration of all the applications can be found. Although the successful approaches in other applications cannot be directly employed in volcanic ash forecasts, their success do stress the importance of designing a proper approach based on the computational analysis of a specific assimilation system. Therefore, the computational cost of our volcanic ash assimilation system will be first analyzed. Then, based on the computational analysis, we will investigate a strategy to accelerate the ensemble-based data assimilation system for volcanic ash forecasts.

This chapter is organized as follows. Section 6.2 analyzes the computational cost of the conventional volcanic ash data assimilation system. In Section 6.3, the mask-state algorithm is developed for acceleration. The discussions on the mask-state algorithm is in Section 6.4. Finally, the last section summarizes the concluding remarks of our research.

Note that in the chapter we don't use covariance localization as proposed by Hamill *et al.* (2001) for reducing spurious covariances. This is because although localization is possible, the ideal case is not to use it in order to have the correct covariances in a large (converged) ensemble. It is crucial for localization that when unphysical (spurious) covariances are eliminated, physical (correct) covariances can be well maintained (Petrie and Dance, 2010). If the "filtering length scale" for localization is too long (i.e., all the dynamical covariances are allowed), many of the

spurious covariances may not be eliminated. If the length is too short, important physical dynamical covariances then may be lost together with the spurious ones. Therefore, essentially deciding an accurate localization is a challenging subject (Rishojgaard, 1998; Kalnay *et al.*, 2012) especially for accuracy-demanding applications. Therefore, in this chapter we choose the ensemble size of 100 to guarantee the accuracy and avoid large spurious covariances.

6.2. Computational analysis for volcanic ash data assimilation

6.2.1. Computational analysis of the total runtime

Ensemble-based data assimilation is a useful approach to improve the forecast accuracy of volcanic ash transport. However, if it is time-consuming, it cannot be taken as efficient due to the high requirement on speed for volcanic ash assimilation (see Section 6.1). Based on this consideration, we need to analyze the computational cost of a conventional volcanic ash assimilation system.

The total execution time of conventional EnKF comprises four parts, i.e., initialization, forecast, analysis and other computational cost. The initialization time includes reading meteorological data, initializing model geographical and grid configurations, reading emission information, initializing stochastic observer for reading and transforming observations to the model grid, initializing all the ensemble states and ensemble mean, and so on. The forecast time is obtained from Eq. (2.4), while the analysis time corresponds to the computational sum from Eq. (2.5) to (2.10). The other computational time includes script compiling, setting environment variables, starting and finalizing data assimilation algorithms, etc.

The evaluation result of the conventional EnKF is shown in Table 6.1 (the middle column). It can be seen that the total computational time (4.36 h) is relatively large compared to the simulation window (3.0 h, i.e., from 9:00–12:00 UTC, 18 May, 2010), which is too much in an operational sense. Therefore, in this chapter, we aim to accelerate the computation to within an acceptable runtime (i.e., requires less runtime than the time period of the data assimilation application).

It can be also observed from Table 6.1 that the main contribution to the total execution time is the analysis step. Compared to the initialization and forecast time, the analysis stage takes 72% of the total runtime. Due to the expensive analysis step, although some approaches (such as MPI-parallel I/O (Filgueira *et al.*, 2014), domain decomposition (Segers, 2002)) can potentially accelerate the initialization and forecast step, the effect to the final acceleration of the total computational cost is little. Therefore, to get acceptable computational time, the cost reduction in the analysis step is the target. One may wonder that since the amount of observations is small, why does analysis takes so much time? The large state vector seems to be left responsible for the problem. To know the exact reason, the detailed computational cost of the analysis step must be evaluated.

Table 6.1: Comparison of the computational cost of conventional EnKF and MS-EnKF. (h=hour, simulation window = 3.0 h, the time is Wall clock time. The results are obtained from the bullx B720 thin nodes of the Cartesius cluster, which is a computing facility of SURFsara, the Netherlands Supercomputing Centre. Each node is configured with 2 × 12-core 2.6 GHz Intel Xeon E5-2690 v3 (Haswell) CPUs and with memory 64 GB.)

Case	Conventional EnKF	MS-EnKF
Cores used	102	102
Tracer number (n_{spec})	6	6
Measurements of tracers (m)	2	2
Ensemble size (N)	100	100
Parallel in forecast step	Yes	Yes
Parallel in analysis step	No	No
Mask-state in analysis step	No	Yes
Initialization	0.42 h	0.42 h
Forecast	0.65 h	0.65 h
Analysis	3.14 h	0.88 h
Others	0.15 h	0.12 h
Total Runtime	4.36 h	1.95 h

6.2.2. Cost estimation of all analysis procedures

We start with the formulations of the analysis step. The analysis step is represented by Eq. (2.10), which can be written in a full matrix format with Eq. (6.1),

$$\mathbf{A}^a_{n\times N} = \mathbf{A}^f_{n\times N} + \mathbf{K}_{n\times m}(\mathbf{Y}_{m\times N} - \mathbf{H}_{m\times n}\mathbf{A}^f_{n\times N}), \tag{6.1}$$

where the subscripts represent the matrix's dimensions. $\mathbf{A}^f$ and $\mathbf{A}^a$ represent the forecasted and analyzed ensemble state matrix, and are respectively built up from $\boldsymbol{\xi}^f$ and $\boldsymbol{\xi}^a$ with N ensembles. The measurement ensemble matrix $\mathbf{Y}$ is formed by an ensemble of $\mathbf{y} + \mathbf{v}$ (see Eq. (2.10)). $\mathbf{H}$ is the observational matrix, which is used to select state variables (at measurement locations) in the full ensemble state matrix corresponding to the measurement ensemble matrix $\mathbf{Y}$. n is the number of model state variables in a three-dimensional (3D) domain, i.e., $\sim 10^6$ in this chapter (see Section 2.1.3). m is the amount of measurements at one assimilation time, which depends on the measurement type. For aircraft in situ measurements used in this chapter (see Fig. 4.1), two measurements are made at each time by one research flight, so that m is 2 here. N is the ensemble size and is taken as 100 in this chapter. As described in Eq. (2.6), the ensemble perturbation matrix $\mathbf{L}^f$ in EnKF can be re-written as

$$\mathbf{L}^f_{n\times N} = \mathbf{A}^f_{n\times N} - \bar{\mathbf{A}}^f_{n\times N} = \mathbf{A}^f_{n\times N}(\mathbf{I}_{N\times N} - \frac{1}{N}\mathbf{1}_{N\times N}) = \mathbf{A}^f_{n\times N}\mathbf{B}_{N\times N}, \tag{6.2}$$

where $\mathbf{I}$ is an $N\times N$ unit matrix and $\mathbf{1}$ is an $N\times N$ matrix with all elements equal to 1. Thus, $\mathbf{L}^f = \mathbf{A}^f\mathbf{B}$ where $\mathbf{B}_{N\times N}$ is introduced to represent $(\mathbf{I}_{N\times N} - \frac{1}{N}\mathbf{1}_{N\times N})$. So that, $\mathbf{HL}^f = \mathbf{O}^f\mathbf{B}$, where $\mathbf{O}^f_{m\times N}$ is used to represent $(\mathbf{HA}^f)$. Here we explicitly express $\mathbf{L}^f$ and $\mathbf{HL}^f$ in the form of $\mathbf{A}^f$ and $\mathbf{O}^f$, respectively. This is because in our volcanic ash assimilation system, $\mathbf{A}^f$ and $\mathbf{O}^f$ are two of the three inputs (another one is the measurement ensemble matrix $\mathbf{Y}$ for the analysis step. These are the three inputs used for actual computations in the analysis step. As shown in Fig. 6.1a, $\mathbf{A}^f$ is obtained from the forecast step, $\mathbf{O}^f$ and $\mathbf{Y}$ are acquired from our stochastic observer module (see Fig. 6.1a) which is used for a volcanic ash transport model to integrate geophysical measurements. With the input $\mathbf{Y}$, the measurement error covariance $\mathbf{R}$, as introduced in Eq. (2.9), can be then computed with

$$\mathbf{R}_{m\times m} = \frac{1}{N-1}(\mathbf{Y}_{m\times N} - \bar{\mathbf{Y}}_{m\times N})(\mathbf{Y}_{m\times N} - \bar{\mathbf{Y}}_{m\times N})' = \frac{1}{N-1}(\mathbf{YB})(\mathbf{YB})'. \tag{6.3}$$

Based on previous definitions and Eq. (2.5) to (2.10), the analysis step can be

a

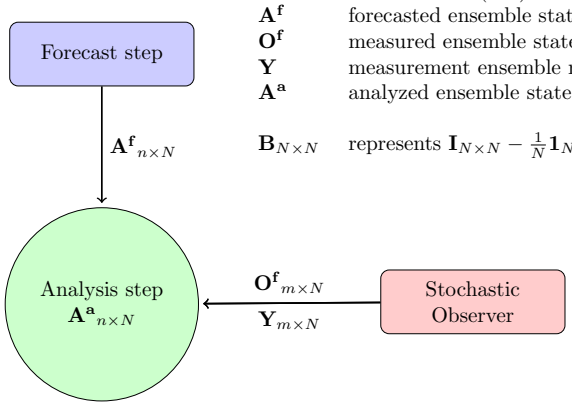

n	ash state number (3.888×10^6)
m	measurement number (2)
N	ensemble size (100)
$\mathbf{A^f}$	forecasted ensemble state matrix ($n \times N$)
$\mathbf{O^f}$	measured ensemble state matrix ($m \times N$)
$\mathbf{Y}$	measurement ensemble matrix ($m \times N$)
$\mathbf{A^a}$	analyzed ensemble state matrix ($n \times N$)
$\mathbf{B}_{N\times N}$	represents $\mathbf{I}_{N\times N} - \frac{1}{N}\mathbf{1}_{N\times N}$

b

Computational cost of analysis step

Procedures	Cost
$\mathbf{X_1} = \mathbf{O}^f\mathbf{B}$	$\mathrm{O}(mN^2)$
$\mathbf{X_2} = \mathbf{YB}$	$\mathrm{O}(mN^2)$
$\mathbf{X_3} = \mathbf{X_1X_1}' + \mathbf{X_2X_2}'$	$\mathrm{O}(m^2N)$
$\mathbf{X_4} = \mathbf{X_3}^{-1}$ (Singular Value Decomposition (SVD))	$\mathrm{O}(m^3)$
$\mathbf{X_5} = \mathbf{BX_1}'$	$\mathrm{O}(mN^2)$
$\mathbf{X_6} = \mathbf{X_5X_4}$	$\mathrm{O}(m^2N)$
$\mathbf{X} = \mathbf{I} + \mathbf{X_6}(\mathbf{Y} - \mathbf{O}^f)$	$\mathrm{O}(mN^2)$
$\mathbf{A^a} = \mathbf{A^fX}$	$\mathrm{O}(nN^2)$
	(n=3.888×10^6, m=2, N=100.)

Figure 6.1: **Computational evaluation of the analysis step.** **a**, Illustration of the analysis step. **b**, Computational cost of all sub-part of the analysis step.

reformulated as followings,

$$\begin{aligned}\mathbf{A}^a_{n\times N} &= \mathbf{A}^f + \mathbf{K}(\mathbf{Y}-\mathbf{H}\mathbf{A}^f)\\ &= \mathbf{A}^f + \mathbf{P}^f\mathbf{H}'(\mathbf{H}\mathbf{P}^f\mathbf{H}'+\mathbf{R})^{-1}(\mathbf{Y}-\mathbf{H}\mathbf{A}^f)\\ &= \mathbf{A}^f + \frac{1}{N-1}\mathbf{L}^f(\mathbf{H}\mathbf{L}^f)'[\frac{1}{N-1}(\mathbf{H}\mathbf{L}^f)(\mathbf{H}\mathbf{L}^f)' + \frac{1}{N-1}(\mathbf{Y}\mathbf{B})(\mathbf{Y}\mathbf{B})']^{-1}(\mathbf{Y}-\mathbf{H}\mathbf{A}^f)\\ &= \mathbf{A}^f + \mathbf{A}^f\mathbf{B}(\mathbf{O}^f\mathbf{B})'[(\mathbf{O}^f\mathbf{B})(\mathbf{O}^f\mathbf{B})' + (\mathbf{Y}\mathbf{B})(\mathbf{Y}\mathbf{B})']^{-1}(\mathbf{Y}-\mathbf{O}^f)\\ &= \mathbf{A}^f\{\mathbf{I}+\mathbf{B}(\mathbf{O}^f\mathbf{B})'[(\mathbf{O}^f\mathbf{B})(\mathbf{O}^f\mathbf{B})' + (\mathbf{Y}\mathbf{B})(\mathbf{Y}\mathbf{B})']^{-1}(\mathbf{Y}-\mathbf{O}^f)\}\\ &= \mathbf{A}^f_{n\times N}\mathbf{X}_{N\times N} \quad ,\end{aligned} \tag{6.4}$$

where

$$\mathbf{X}_{N\times N} = \{\mathbf{I}+\mathbf{B}(\mathbf{O}^f\mathbf{B})'[(\mathbf{O}^f\mathbf{B})(\mathbf{O}^f\mathbf{B})' + (\mathbf{Y}\mathbf{B})(\mathbf{Y}\mathbf{B})']^{-1}(\mathbf{Y}-\mathbf{O}^f)\}. \tag{6.5}$$

Eq. (6.4) shows how the analysis step is performed in a volcanic ash assimilation system. In order to accelerate the analysis step, the most time-consuming part must be reduced. Fig. 6.1b shows estimations of the computational cost for each procedure in the analysis step. Considering that the state number n ($\sim 10^6$) is significantly larger than the measurement number m (m=2 here) and the ensemble size N (N=100), thus the most time-consuming procedure in the analysis step is the last one, that is $\mathbf{A^a} = \mathbf{A^f X}$ with computational cost of O(nN^2). Therefore, in our volcanic ash assimilation system, this part is the most time-consuming part in the analysis step. Note that the procedure $[(\mathbf{O}^f\mathbf{B})(\mathbf{O}^f\mathbf{B})' + (\mathbf{Y}\mathbf{B})(\mathbf{Y}\mathbf{B})']^{-1}$ for Singular Value Decomposition (SVD) in our chapter is not time-consuming, which is quite different from some other applications, such as reservoir history matching (Tavakoli *et al.*, 2013; Khairullah *et al.*, 2013). This is because the SVD procedure costs O(m^3), and due to the measurement size in the order of the size of the state in those cases, SVD procedure thus requires a huge computational cost for reservoir assimilation.

6.3. The mask-state algorithm for acceleration of the analysis step

6.3.1. Characteristic of ensemble state matrix $\mathbf{A^f}$

Analysis in the previous section shows that $\mathbf{A^a} = \mathbf{A^f X}$ is most expensive in the analysis step. Each column of $\mathbf{A^f}$ is constructed from a forecasted ensemble state, thus the dimension of $\mathbf{A^f}$ is $n \times N$. In each column, the element values correspond to volcanic ash concentrations in a 3D domain. Fig. 6.2 shows the coverage of all ensemble forecast states at a selected time 10:00 UTC 18 May, 2010, without loss of generality. A common phenomenon can be observed, that is only a part of the 3D domain are filled with volcanic ash. The ash clouds only concentrate in a plume which is transported over time. This is because volcanic eruption is a fast and strong process. The advection dominates the transport, and the volcanic ash

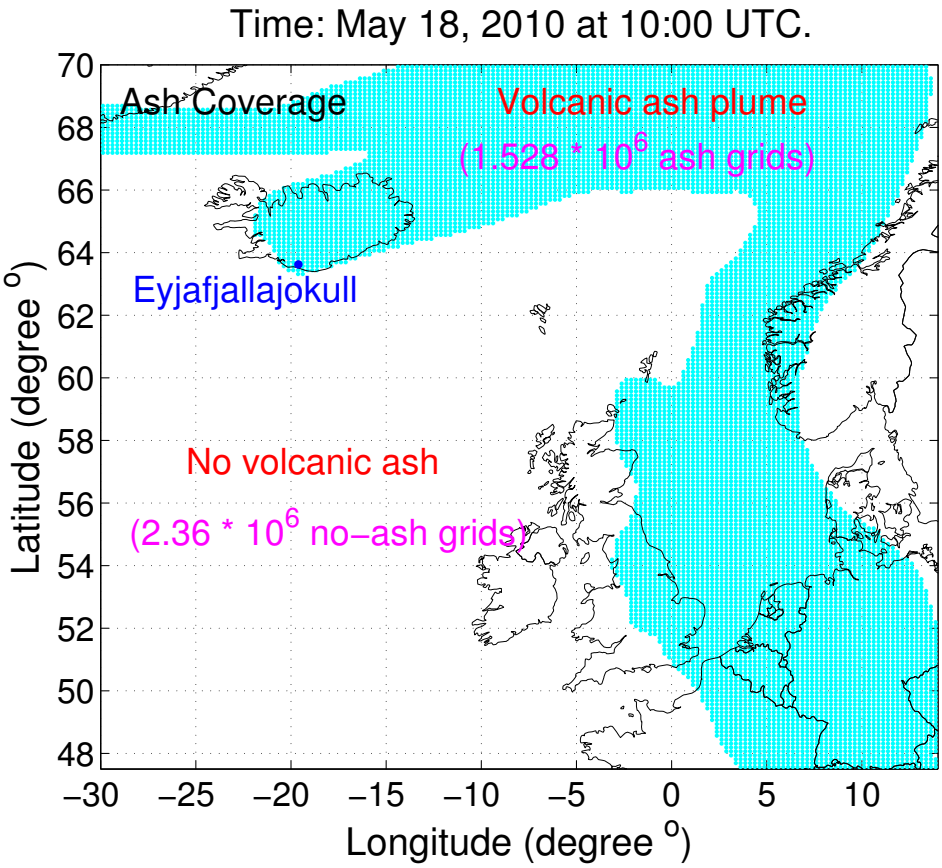

Figure 6.2: **Characteristic of volcanic ash state.**

plume is transported with the wind. This is a particular characteristic for volcanic ash transport, in contrast to other atmospheric related applications such as ozone (Curier *et al.*, 2012), SO_2 (Barbu *et al.*, 2009), CO_2 (Chatterjee *et al.*, 2012). For those applications, the concentrations are everywhere in the domain, the emission sources are also everywhere, and observations are available throughout the domain too (especially for satellite data). Whereas for application of volcanic ash transport, the source emission is only at the volcano, thus usually only a limited domain is polluted by ash. As shown in Fig. 6.2, in the 3D domain with grid size of 3.888×10^6, the number of grids in the area with volcanic ash is counted as 1.528×10^6, whereas the number of no-ash grids is 2.36×10^6. Note that shown in the figure are accumulated ash coverages of all ensemble states, thus in the no-ash grids, there are no ash for all the ensemble states. Thus a very large number of rows in $\mathbf{A^f}$ are zero corresponding to the no-ash grids. These zero rows in $\mathbf{A^f}$ have no contributions to $\mathbf{A^a} = \mathbf{A^f X}$, because a zero row in $\mathbf{A^f}$ always results in a zero row in $\mathbf{A^a}$. Therefore, for the case of Fig. 6.2, $\frac{2}{3}$ of the computations are redundant and can be avoided. To realize this, one may think to limit the domain for the entire assimilation steps, then the number of zero rows certainly would be largely reduced. This is actually incorrect, because these zero rows are changing along with the transport of ash clouds, and not constant at each analysis step. So the full domain must be considered and it should be adaptive (choose different zero rows according to different $\mathbf{A^f}$ at different analysis time).

6.3.2. Derivation of the mask-state algorithm (MS)

Here we introduce item n_{noash} to represent the number of zero rows in the ensemble state matrix $\mathbf{A^f}$, and use n_{ash} to represent the number of other rows (also n_{ash} represents the grid size of ash plume). When computing $\mathbf{A^a} = \mathbf{A^f X}$, to avoid all the computations related to n_{noash} rows with zero elements, the index of other n_{ash} rows must be first decided. This index is meant to reduce the dimensions of $\mathbf{A^f}$. After getting a $\mathbf{A^a}$ with a dimension of $n_{ash} \times N$, the index will be used again to reconstruct the full matrix $\mathbf{A^a}$ with the dimension of $n \times N$. Based on this idea, we propose a mask-state algorithm (MS) which deals with the time-consuming analysis update. MS includes five steps:

(i) **Compute ensemble mean state** $\bar{\mathbf{A}}^\mathbf{f}$: The mean state $\bar{\mathbf{A}}^\mathbf{f}_{n\times1}$ can be easily computed by averaging $\mathbf{A^f}_{n\times N}$ along N columns. Due to all elements in $\mathbf{A^f}_{n\times N}$ corresponding to ash concentrations, thus all elements in $\mathbf{A^f}_{n\times N}$ are larger than zero, so that the index of non-zero rows in $\bar{\mathbf{A}}^\mathbf{f}_{n\times1}$ is equivalent to that in $\mathbf{A^f}_{n\times N}$. The computational cost for this step is O(nN).

(ii) **Construct mask array** $\mathbf{z}$: Based on previously obtained $\bar{\mathbf{A}}^\mathbf{f}_{n\times1}$, we search the non-zero elements of $\bar{\mathbf{A}}^\mathbf{f}_{n\times1}$ and record the index into a mask array $\mathbf{z}_{n_{ash}\times1}$. With this strategy, we don't need to search the full matrix $\mathbf{A^f}_{n\times N}$ and build an index matrix for storage. This is a benefit for saving memory. The computational cost for this step is O(n).

(iii) **Construct masked ensemble state matrix** $\tilde{\mathbf{A}}^\mathbf{f}$: Using the mask array

$\mathbf{z}_{n_{ash}\times 1}$ obtained from step (ii), $\tilde{\mathbf{A}}^{\mathbf{f}}_{n_{ash}\times N}$ can be constructed column by column according to Eq. (6.6), and the computational cost (overhead) for this step is O($n_{ash}N$).

$$\tilde{\mathbf{A}}^{\mathbf{f}}(1:n_{ash},1:N)=\mathbf{A}^{\mathbf{f}}(\mathbf{z}(1:n_{ash}),1:N), \tag{6.6}$$

(iv) **Compute $\tilde{\mathbf{A}}^{\mathbf{a}}$ by multiplying $\tilde{\mathbf{A}}^{\mathbf{f}}$ and $\mathbf{X}$:** Perform matrix computation $\tilde{\mathbf{A}}^{\mathbf{a}}_{n_{ash}\times N}=\tilde{\mathbf{A}}^{\mathbf{f}}_{n_{ash}\times N}\mathbf{X}_{N\times N}$. This step is similar to $\mathbf{A}^{\mathbf{a}}=\mathbf{A}^{\mathbf{f}}\mathbf{X}$, as described in Section 6.2.2, but the computational cost now becomes O($n_{ash}N^2$) instead of O(nN^2).

(v) **Construct analyzed ensemble state matrix $\mathbf{A}^{\mathbf{a}}$:** With the computed $\tilde{\mathbf{A}}^{\mathbf{a}}$ from step (iv) and the mask array $\mathbf{z}$ from step (ii), the final analyzed ensemble state matrix $\mathbf{A}^{\mathbf{a}}{}_{n\times N}$ can be constructed based on Eq. (6.7). The computational cost (overhead) for this step is O(nN).

$$\mathbf{A}^{\mathbf{a}}(\mathbf{z}(1:n_{ash}),1:N)=\tilde{\mathbf{A}}^{\mathbf{a}}(1:n_{ash},1:N), \tag{6.7}$$

According to the derivations of MS, the computational cost related to zero rows are avoided. Here the "zero rows" doesn't equal to "zero elements". The former corresponds to the regions where there are no ash for all the ensemble members, while the latter also counts the no-ash regions specifically for some ensembles. Certainly the consideration of all "zero elements" can include all the sparsity information of the ensemble state matrix, but extra computations and memories must be spent on searching the full matrix $\mathbf{A}^{\mathbf{f}}{}_{n\times N}$ with a computational cost of O(nN) and storing a mask state matrix with dimensions of $n\times N$. This is expensive compared to construct the mask array in the procedure (ii). Actually, after a careful check on the volcanic ash ensemble plumes, there is no "bad" ensemble which is really different from others. Although the concentration level in ensemble members are distinct, the main direction and the occurrence to the grid cells are more or less same. This means, the "zero rows" actually more or less equals to "zero elements", but much faster than the way with "zero elements", which confirms the suitability and advantage of procedure (ii). Probably when there are big meteorological uncertainties, the "zero elements" will be much larger than "zero rows". In this case, how to make use of the sparsity information in the ensemble state matrix, will be considered in future.

Based on procedures of MS, the computational cost of $\mathbf{A}^{\mathbf{a}}=\mathbf{A}^{\mathbf{f}}\mathbf{X}$ can be reduced. However, without a careful evaluation, we cannot conclude MS is fast, because the algorithm also employs other procedures. If these procedures (i)(ii) (iii)(v) are much cheaper than the main procedure (iv), MS can definitely speed up the analysis step, and vice versa. Now we analyze MS's computational cost, which can be summed as O(nN)+ O(n)+ O($n_{ash}N$)+ O($n_{ash}N^2$)+ O(nN), i.e., O($nN+n_{ash}N^2$). Thus, the computational overhead involved to transform the full matrix to a small one (i.e., O($n_{ash}N$) for procedure (iii)) has little effect in the total computation cost of MS (i.e., O($nN+n_{ash}N^2$)). However, the computational overhead of transforming the small matrix to the full one (i.e., O(nN) for procedure (v)) does contribute a part,

which cannot be ignored, to the total MS's computational cost. The computational cost without MS is O(nN^2).

The comparison between both cost (with and without MS, i.e., O($nN + n_{ash}N^2$) and O(nN)) indicates when the number of non-zero rows (n_{ash}, i.e., the number of grids with ash) of the forecasted ensemble state matrix satisfies $n_{ash} < \frac{N-1}{N}n$, then MS can accelerate $\mathbf{A^a} = \mathbf{A^f X}$. Here, O($nN + n_{ash}N^2$) and O($nN$) are of the same order when $n_{ash} < \frac{N-1}{N}n$. The larger the difference between n_{ash} and $\frac{N-1}{N}n$, the better the speedup can be achieved. According to this analysis, and the characteristic (e.g., $\frac{n_{ash}}{n}$ approximately equals to $\frac{1}{3}$ in this case) of volcanic ash transport as described in Section 6.3.1, the relation is certainly satisfied and is actually $n_{ash} \ll \frac{N-1}{N}n$ (significantly smaller) for our study. Therefore, for our volcanic ash assimilation system, with MS, the computational cost for the time-consuming part $\mathbf{A^a} = \mathbf{A^f X}$ is O($n_{ash}N^2$), which is much reduced compared to O(nN^2) with conventional computations.

The relation $n_{ash} < \frac{N-1}{N}n$ indicates whether we would have speedup by the MS method, actually it can be extended to Eq. (6.8),

$$S_{\mathbf{ms}} = \frac{\mathbf{O}(nN^2)}{\mathbf{O}(nN + n_{ash}N^2)} = \mathbf{O}(\frac{n}{n_{ash}}), \tag{6.8}$$

which explicitly specifies the expected amount of speedup ($S_{\mathbf{ms}}$) of $\mathbf{A^a} = \mathbf{A^f X}$ by the MS algorithm. In this case study, N is taken at 100 and $\frac{n_{ash}}{n} \approx \frac{1}{3}$, so $S_{\mathbf{ms}}$ is approximately 3.0.

According to Amdahl's law (Amdahl, 1967), the total computational speedup ($S_{\mathbf{total}}$) by MS can be predicted by Eq. (6.9),

$$S_{\mathbf{total}} = \frac{1}{(1 - p_{\mathbf{ms}}) + \frac{p_{\mathbf{ms}}}{S_{\mathbf{ms}}}}, \tag{6.9}$$

where $p_{\mathbf{ms}}$ is the proportion of the computational cost of $\mathbf{A^a} = \mathbf{A^f X}$ in the overall data assimilation computations. It has been evaluated that the computational cost of $\mathbf{A^a} = \mathbf{A^f X}$ dominates the analysis step (see Fig. 6.1**b**), thus the proportion of the computational cost of $\mathbf{A^a} = \mathbf{A^f X}$ approximates the proportion of the analysis step in the total data assimilation computations (i.e., $p_{\mathbf{ms}}$ ≈72% in this case, as described in Section 6.2.1). Therefore, based on Eq. (6.9), the maximum ("ideal") computational speedup can be predicted to be $\frac{1}{1-p_{\mathbf{ms}}}$ (i.e., ≈3.57 for this case study) when $S_{\mathbf{ms}}$ approximates infinity. However, this is not the actual speedup because $S_{\mathbf{ms}}$ is in fact specified by Eq. (6.8). (Based on discussions above, $S_{\mathbf{total}}$ can be therefore estimated by Eq. (6.8) at ≈2.0 in this case.)

6.3.3. Experimental results

Analysis of the algorithmic complexity of the mask-state algorithm (MS) shows MS is an efficient approach to reduce the computational cost of the time-consuming $\mathbf{A^a} = \mathbf{A^f X}$. Now MS will be applied in the real volcanic ash assimilation system, to investigate whether in practice it can well speed up the analysis step. We perform MS in the conventional EnKF, which means initialization, forecast steps are

all computed as the conventional EnKF. The only difference between MS-EnKF and conventional EnKF is that in the former MS is employed for analysis step, and in the latter is standard analysis step. The result and related specifications are shown in Table 6.1. As introduced in Section 2.2.3, the forecast step has been configured with the conventional parallelization, thus N+2 (102 here) cores are actually used (one core for the data assimilation algorithm, the other N+1 cores for the parallel forecast of N ensemble members and one ensemble mean). It can be seen that MS indeed largely accelerates the analysis step (as expected, by a factor of about 3.0 for this chapter) which confirms the theoretical cost evaluation. The mask-state algorithm is now experimentally proven as efficient to significantly reduce the computational time for the analysis step during volcanic ash assimilation.

Note that it can also be observed that the computational time for the "other" parts in Table 6.1 (such as operations for setting environmental variables, starting and finalizing data assimilation algorithms, as mentioned in Section 6.2.1) is slightly reduced by the MS method (i.e., 0.03 h in this case). This is because in the conventional EnKF, the ensemble mean state $\bar{\mathbf{A}}^{\mathbf{f}}$ is calculated in the "other" parts as an output to finalize the data assimilation algorithms, while in MS-EnKF, the calculations of $\bar{\mathbf{A}}^{\mathbf{f}}$ are needed and directly involved in the "Analysis" part.

The result shows that benefiting from the success of reduced analysis step, the overall computational cost indeed gets significantly reduced. The total execution time is 1.95 h which is less than the simulation window of 3 h (09:00 – 12:00 UTC, May 18, 2010). This result satisfies our goal to accelerate the computation to an acceptable runtime (i.e., requires less run time than the time period of the data assimilation application). Therefore, aviation advices based on the MS-EnKF can be provided as not only accurate, but also sufficiently fast. Note that the result (1.95 h) is obtained after the volcanic ash is transported to the continental Europe. If the assimilation is performed in the starting phase of volcanic ash eruption (when aircraft measurements are available), a more significant acceleration would be obtained. This is because in this case the volcanic ash is only transported in an area near to the volcano, thus the number of no-ash grid cells will take a large proportion (much higher than $\frac{2}{3}$ for this case study) of the full domain.

Another note is that in this chapter, we only perform the commonly used ensemble parallelization for the forecast step (already efficient compared to the expensive analysis step), but do not choose model-based parallelization (e.g., tracer or domain decomposition). As specified in Table 6.1, no parallelization is implemented on the 6 tracers. This is because due to the important aggregation process (Folch *et al.*, 2010), there are big dependencies between different ash components and thus it doesn't make much sense to parallelize them. As for domain-decomposed parallelization (Segers, 2002), it is not efficient here. This is because volcanic ash is special in the sense that the model is only doing computations in a small part of the domain (i.e., there is no data in a rather large part of domain), but this part is continuously changing. Thus, a fixed domain decomposition is not very useful here because of the changing plume position. In this sense, some advanced approach such as adaptive domain-decomposed parallelization (Lin *et al.*, 1998) might add additional acceleration to the volcanic ash forecast stage. This is an interesting sub-

ject for future in case, when a more complicated model is employed, only ensemble parallelization may be not enough for the forecast stage.

6.4. Discussions

6.4.1. Applicability

For volcanic ash forecasts, only a relatively small domain is polluted compared to the full 3D domain, so that the mask-state algorithm (MS) can work efficiently. For other applications with similar characteristic (e.g., exploding nuclear plants or factories, chemicals or oil leaking on seas), MS can achieve the same effect on the computations of $\mathbf{A^a} = \mathbf{A^f X}$. It has been analyzed that when the number of non-zero rows (n_{ash}, i.e., the number of ash grids in a 3D domain) of $\mathbf{A^f}$ satisfies $n_{ash} < n$, MS can work faster than standard EnKF. For volcanic ash application, because n_{ash} is much less than n, the acceleration is thus quite large. Hence in this case, we propose to embed the mask-state algorithm (MS) in all ensemble-based data assimilation methods because it is fast and the implementation using MS is exact to the standard ensemble-based methods, i.e., it doesn't introduce any approximation in view of MS procedures. Actually this proposal can be extended to all real applications, even if the condition is not satisfied. This is because, in this case the computational cost of MS for $\mathbf{A^a} = \mathbf{A^f X}$ becomes O(nN^2), which is the same as that of using the standard assimilation (shown in Fig. 6.1b). Therefore, if the state numbers equal to or close to the number of the total number of grid points in the domain, the added computational cost by using MS is very small (neglectable), so that the computational time with MS is almost the same as the time of using the standard approach. Whereas, when the condition $n_{ash} < n$ is satisfied, MS will accelerate the analysis step. Thus MS is generic and can be directly used in any ensemble-based data assimilation, and this acceleration can be automatically realized for some potential applications, without spending time investigating if the condition is satisfied. In a real (or operational) 3D assimilation system, MS can be easily included, i.e., we only need to invoke the MS module when computing $\mathbf{A^a} = \mathbf{A^f X}$, without any other change to the current framework.

As stated in Eq. (6.8), the speedup of the MS method is approximately the inverse of $\frac{n_{ash}}{n}$. So far there is no statistical data on the value of $\frac{n_{ash}}{n}$. Consider the problem of volcanic ash transport, there is only one emission point (at the volcano), all the ashes in atmospheres are transported by the directional wind drive from the same source point. Thus volcanic ash cloud is actually transported in a shape of a plume, which in general doesn't cover the full but only a small part of the 3D domain. At the start phase of a volcanic ash eruption, $\frac{n_{ash}}{n}$ is much smaller than 1.0 (started from 0). During transport over a long time (one and a half months for this case study), $\frac{n_{ash}}{n}$ increases to approximately $\frac{1}{3}$. Therefore, the speedup of MS on volcanic ash data assimilation will be significant.

6.4.2. MS and localization

Based on the formulation of MS, one may think it can be taken as a localization approach ((Hamill *et al.*, 2001)). There is indeed a similarity between MS and the

localization approach, in a sense that when computing $\mathbf{A^a} = \mathbf{A^f X}$, both get rid of a large number of cells, and only do computations related to the selected grids. These two algorithms are however functionally different. This is because the localization approach is meant for reducing spurious correlations outside a local region which is built up around the measurement, thus the results with and without localization approaches are different. While, MS is developed for the acceleration purpose. The masked region is discontinuous and independent of locations of measurement, but dependent on the model domain. Thus, there is no difference on the assimilation results between using MS and without using it. Therefore, based on the functional difference, MS cannot be taken as a localization approach.

In this chapter, we don't employ the localization strategy in the analysis step, because we use a rather large ensemble size of 100 to guarantee the accuracy. But for some applications (e.g., ozone, CO_2, sulfur dioxide) especially when assimilating satellite data, localization is a necessary approach and has been widely used in reducing spurious correlations (Barbu *et al.*, 2009; Chatterjee *et al.*, 2012; Curier *et al.*, 2012). In these cases, because the localization approach forces the analysis only to update state within a localization region, one may think that localization could replace MS and there would be no significance to employ MS. Actually this is not correct. We explain the reason as follows.

The Schur product $\mathbf{f} \circ \mathbf{P}^f$ in Eq. (2.9) is defined by the element-wise multiplication of the covariance matrix $\mathbf{P}^f$ and a localization matrix $\mathbf{f}$. $\mathbf{f}$ is defined based on the distance between two locations, thus it is dependent on the domain and needs information of the full ensemble state locations. In this way, $\mathbf{f} \circ \mathbf{P}^f$ can contain more zeros than $\mathbf{P}^f$, but the dimensions are not changed, so that the computations related to $\mathbf{f} \circ \mathbf{P}^f$ are actually not reduced. Therefore, we can understand the localization approach in the analysis step as that the state within and outside a local region are both updated with increments, but just the increments outside the region are zero (which seems like not updating). This is also the reason why the localization approach is not meant for acceleration but only for reducing spurious covariances. Now it is clear that localization cannot replace MS. Actually both can be performed together in dealing with the time-consuming part $\mathbf{A^a} = \mathbf{A^f X}$. The localization approach can first transfer $\mathbf{A^f}$ to a localized matrix with more zero rows. Then MS can be used to accelerate the multiplication of the localized matrix and $\mathbf{X}$. In this way, MS is expected to accelerate $\mathbf{A^a} = \mathbf{A^f X}$ with a high speedup rate, because the computational cost of more zero rows in the localized ensemble state matrix are avoided.

6.5. Conclusions

In this chapter, based on evaluations on the computational cost of volcanic ash data assimilation, the analysis step was estimated as very expensive. Although some potential approaches can accelerate the initialization and forecast step, there would be no notable improvement to the total computational time due to the dominant expensive analysis step. Therefore, to get an acceptable computational cost, the key is to efficiently reduce the execution time of the analysis step.

After a detailed evaluation on various parts of the analysis stage, the most time-

consuming part was revealed. The mask-state algorithm was developed based on a careful study on the characteristic of the ensemble ash states. The algorithm transforms the full ensemble state matrix into a relatively small matrix using a constructed mask array. Subsequently, the computation of the analysis step was sufficiently reduced. The mask-state algorithm is developed as generic, thus it can be embedded in all ensemble-based data assimilation implementations. The extra computational cost of the algorithm is small and usually neglectable.

The conventional ensemble-based data assimilation with the mask-state algorithm is shown to successfully reduce the total computational time to within an acceptable level, i.e., the time must be less than the time period of data assimilation. Consequently, timely and accurate volcanic ash forecasts can be provided for aviation advices. This approach is flexible. It boosts the performance without considering any model-based parallelization, such as domain or component decomposition. Thus, when a parallel model is available, the mask-state approach can be easily combined with the model to gain a further speedup. It implements exactly the standard data assimilation without any approximation and with easy configurations, so that it can be used to accelerate the standard data assimilation in a wide range of applications.

7

Satellite data assimilation to improve forecasts of volcanic ash concentrations

Infrared satellite measurements of volcanic ash mass loadings are often used as input observations into the assimilation scheme. However, these satellite-retrieved data are often two-dimensional (2D), and cannot be easily combined with a three-dimensional (3D) volcanic ash model to continuously improve the volcanic ash state in a data assimilation system.

By integrating available data including ash mass loadings, cloud top heights and thickness information, we propose a satellite observational operator (SOO) that translates satellite-retrieved 2D volcanic ash mass loadings to 3D concentrations at the top layer of the ash cloud. Ensemble-based data assimilation is used to continuously assimilate the extracted measurements of ash concentrations. The results show that satellite data assimilation can force the volcanic ash state to match the satellite observations, and that it improves the forecast of the ash state. Comparison with highly accurate aircraft in situ measurements shows that the effective duration of the improved volcanic ash forecasts is about a half day.

Parts of this chapter have been published in:
(Fu *et al.*, 2016b): *Satellite data assimilation to improve forecasts of volcanic ash concentrations*, **Atmospheric Chemistry and Physics Discussions** 1-22. doi:*10.5194/acp-2016-436*.

7.1. Introduction

Satellite measurements are of special interest, because the detection domain is large and the output data is long-time continuous. For example, the Spin Enhanced Visible and Infrared Imager (SEVIRI), on board the Meteosat Second Generation (MSG) platform provides a large view coverage of the atmosphere and earth's surface (Schmetz *et al.*, 2002). There are 3712 × 3712 pixels covering the full-disk. Images can be acquired for the whole disk every 15 minutes. These satellite data have been used for many years to retrieve ash mass loadings in a dispersing volcanic plume (Prata and Prata, 2012). Nowadays, ash mass loadings (Prata and Prata, 2012), the effective particle size (Kylling *et al.*, 2015) as well as the ash cloud top height (Francis *et al.*, 2012), are available in near real-time as satellite products during volcanic plume transport. The availability of satellite-based data provides us with an opportunity to employ data assimilation with a VATDM to continuously correct the volcanic ash state, and then improve the forecast accuracy of volcanic ash concentrations.

There still exist difficulties on how to efficiently use volcanic ash mass loadings, because a VATDM is in most cases a 3D model, while the satellite-retrieved ash mass loadings are 2D data. One 2D mass loading can be considered as an integral of ash concentrations along a retrieval path (the path can be a line or a curve which depends on a specified retrieval algorithm) (Prata and Prata, 2012). Thus, the 2D measurements are not directly suited in a 3D data assimilation system. Since satellites provides 2D ash mass loadings and the model has 3D concentrations, an observational operator is needed by the data assimilation algorithm, and must be derived to make both types of information directly comparable. For this purpose, vertical information of the ash cloud, such as the ash cloud top height (de Laat and van der A, 2012), the cloud thickness and the corresponding uncertainties, should be included. Cloud-Aerosol Lidar with Orthogonal Polarization (CALIOP) (Winker *et al.*, 2012) lidar measurements can provide detailed vertical information on plumes, but the measurements are spatially sparse and have low temporal resolution (polar-orbit) and the data processing and delivery is not designed for near real-time applications. Thus CALIOP data is not suitable to provide the near real-time thickness information for the overall volcanic ash plume.

For the vertical thickness information of volcanic ash clouds, Schumann *et al.* (2011) investigated on the 2010 Eyjafjallajökull eruption using airborne data that the volcanic ash clouds spread over large parts of Central Europe, mostly from hundreds to 3 km depth. This is consistent with the results of (Marenco *et al.*, 2011) who observed layer depths between 0.5 and 3.0 km. Dacre *et al.* (2015) also examined the ground-based lidar data for the Eyjafjallajökull eruption and found a mean layer depth of 1.2±0.9 km and compared this with model based estimates of 1.1±0.8 km. Prata and Prata (2012) found variable thicknesses ranging from 0.2 up to 3 km. Recently, Clarisse and Prata (2016) reported 16 cases using ground-based lidar measurements during the Eyjafjallajökull eruption and found 3 cases where the cloud thickness was less than 500 m. Cloud thicknesses for Kasatacho (1.01±0.43 km), Sarychev Peak (1.37±0.42 km) and Puyehue-Cordon Caulle (1.80±0.58 km) (private communication) all exceed 1 km, but Prata *et al.* (2015) reported lower

cloud thickness with 80% of cases for the 2006 Chaiten eruption less than 400 m. The vast majority of data suggest thickness in the range 0.5–3 km, but it is entirely possible that thinner clouds (<400 m) do exist. Such clouds must have higher concentrations to be detectable by current infrared satellite techniques (Prata and Prata, 2012; Pavolonis, 2010)) that suggest a lower sensitivity in mass loading of 0.2 g m^{-2}. Thin ash clouds, by their nature are of less concern to aviation because such clouds would be traversed rapidly avoiding the possibility of particle build-up that might lead to engine failure. From a modeling perspective lack of vertical resolution in model wind data makes it not useful to make the cloud depth any less than 500 m.

Based on these investigations, it is not realistic to use a deterministic value to represent the overall ash cloud thickness, but we can reasonably assume that the thickness has a range of 0.5–3.0 km at the corresponding horizontal location of the SEVIRI retrieved measurements. Although this thickness information is not deterministic, its uncertainty spread is suitable in an observational operator for satellite data assimilation. Note that we are only considering the distal plume, at least the part >100 km's from source, which is because close to the emission source the layering of volcanic ash did not necessarily take place.

In this chapter we focus on the case study of the Eyjafjallajökull volcanic ash plume in May 2010. In order to integrate data and information about volcanic ash clouds, the first goal in this chapter is to develop a satellite observational operator to translate satellite-retrieved 2D ash mass loadings to 3D concentrations at the top layer of the ash cloud. Secondly, using the extracted in situ measurements, we investigate whether ensemble-based data assimilation can significantly improve the volcanic ash state. Finally, the effective duration of the improved volcanic ash forecasts after satellite data assimilation is quantified.

7.2. Available data for data assimilation

In this chapter, geostationary SEVIRI observations for the 2010 Eyjafjallajökull volcanic eruption plume (Prata and Prata, 2012) are used as the study case to design a suitable satellite observational operator (SOO) for data assimilation. SEVIRI is a 12-channel spin-stabilized imaging radiometer. Measurements are made with a spatial resolution from 3 km × 3 km at the sub-satellite point to 10 km × 10 km at the edges of the scan. A region covering 30° W to 15° E and 45° N to 70° N is selected here for analysis which includes the geographic area affected by the Eyjafjallajökull volcanic ash (see Fig. 7.1).

The main retrieval products from SEVIRI are ash mass loadings (Prata and Prata, 2012; Kylling *et al.*, 2015) (see Fig. 7.1**a**, value at 0 means no data) where 03:15 UTC 16 May 2010 is chosen for the illustration, without loss of generality. The mass loading at each 2D pixel gives information on the ash cloud from the top view (Prata and Prata, 2012), which can be taken as an integration of ash concentrations along the retrieval path. Besides ash mass loadings, other products including the ash cloud top height (Fig. 7.1**b**), and the error of ash mass loadings (Fig. 7.1**c**) are also available in a near real-time sense (Francis *et al.*, 2012; Prata and Prata, 2012). As a parameter used in SEVIRI retrievals, the data of ash cloud top height

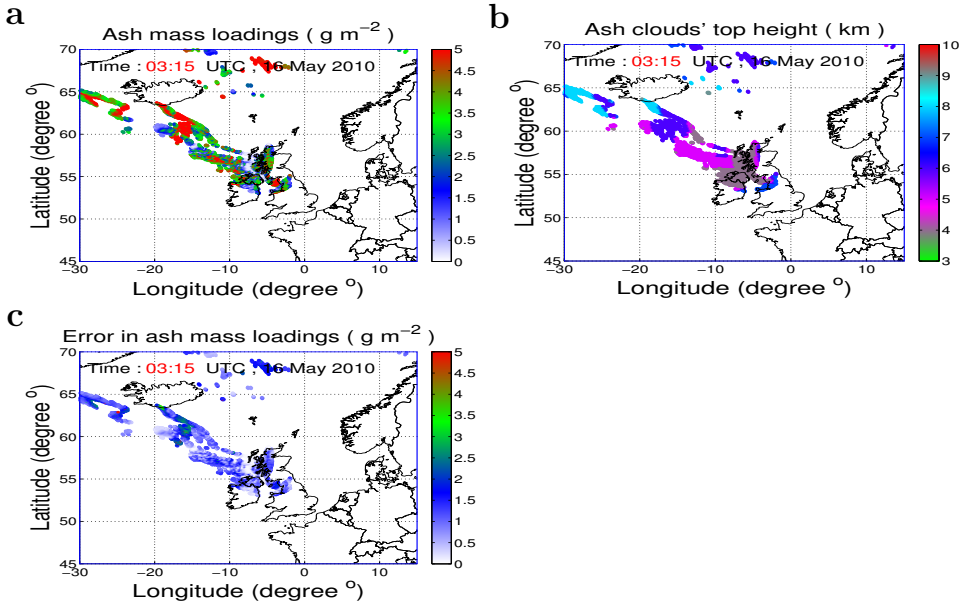

Figure 7.1: **Available volcanic ash data from SEVIRI on 16 May 2010 at 03:15 UTC.** Data are acquired from the European Space Agency (ESA) funded projects Volcanic Ash Strategic Initiative Team (VAST). **a**, Ash mass loadings. Values at 0 mean no data. **b**, Ash cloud top height. **c**, Error in the retrieved ash mass loadings.

is adopted with the SEVIRI-KNMI product of ash height, which has been evaluated with a reasonable accuracy, as reported by de Laat and van der A (2012). The error of ash mass loadings indicates the uncertainty and accuracy of the retrieved mass loadings.

All the data shown in Fig. 7.1 are acquired from the European Space Agency (ESA) funded project – Volcanic Ash Strategic Initiative Team (VAST). The VAST retrieval utilizes two techniques: 1) A rudimentary cloud detection scheme implemented in the Eumetsat operational scheme caled "VOLE" (http://navigator.eumetsat.int/discovery/Start/DirectSearch/DetailResult.do?f%28r0%29=EO:EUM:DAT:MSG:VOLE), and 2) A more complex scheme called CID (Cloud Identification). This scheme is described in an Algorithm Theoretical Basis Document (ATBD) (unpublished but available here: (http://vast.nilu.no/satellite-observations/)). We have used retrievals from the CID scheme. In this chapter, additional processing on the retrieved data is needed to translate the data from the original SEVIRI resolution to the VATDM resolution.

Limited validation has shown that the satellite ash retrievals are sufficiently accurate for use with dispersion models to correct ash concentration forecasts (Prata and Prata, 2012; Kylling *et al.*, 2015). However, the correction cannot be directly and automatically implemented by data assimilation due to the insufficient vertical resolution in satellite data (Bocquet *et al.*, 2015).

7.3. Satellite observational operator (SOO)

7.3.1. Derivation

The derivation of the satellite observational operator (SOO) is shown in Fig. 7.2. The retrieved values by SEVIRI for the ash mass loadings (ML) can be taken as an integration of ash concentrations along the retrieval path. In principle, the satellite retrieval path could be complicated but generally it is assumed to be a straight line (along the line-of-sight, ignoring refraction) from the measuring apparatus. The angle between the local zenith and the line of sight to the satellite is called Viewing Zenith Angle (VZA). The VZA for each pixel is computed according to the satellite VZA algorithms (Gieske *et al.*, 2005) by using general parameters (such as longitude, latitude of each pixel). With the cosine of this angle and the retrieved ash mass loadings (ML), the mass loadings in the vertical direction ($\mathrm{ML_{vert}}$) can be calculated by Eq. (7.1),

$$\mathrm{ML_{vert}} = \mathrm{ML} \times \cos(\mathrm{VZA}). \tag{7.1}$$

To extract ash concentrations from SEVIRI retrievals, $\mathrm{ML_{vert}}$ only is not sufficient and knowledge about the vertical distribution of ash cloud must be included. The cloud vertical profile can be described with the height of the top and the thickness of the cloud. As introduced in Section 7.2, the cloud top height ($\mathrm{H_{top}}$) is available from satellite remote sensing and the thickness of the plume is investigated ($\mathrm{T_{low}}$ to $\mathrm{T_{high}}$, i.e., 0.5 to 3 km). Fig. 7.2 illustrates how the 3D ash concentrations are extracted from the obtained mass loadings in the vertical direction ($\mathrm{ML_{vert}}$). The

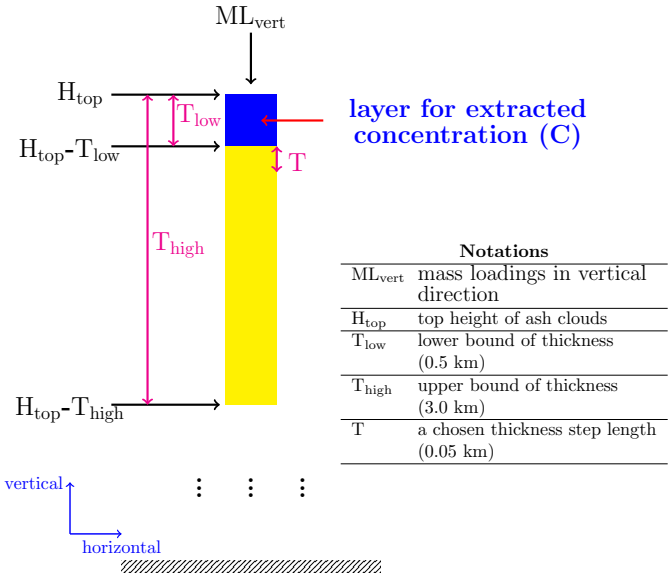

Notations

ML_{vert}	mass loadings in vertical direction
H_{top}	top height of ash clouds
T_{low}	lower bound of thickness (0.5 km)
T_{high}	upper bound of thickness (3.0 km)
T	a chosen thickness step length (0.05 km)

Figure 7.2: **Illustration of the satellite observational operator (SOO)**. The ash concentration is extracted at the cloud top layer.

blue layer in Fig. 7.2 is determined by the lowest possible thickness (T_{low}) and the extraction layer used in this chapter only refers to the blue layer.

When the top height and the thickness range of ash cloud are known, the ash concentration (C) in the extraction layer can be calculated by using the ash mass loadings (ML_{vert}) at the corresponding horizontal location. The details are formulated as follows. First we define

$$N_s = \lceil \frac{T_{high} - T_{low}}{T} \rceil \quad , \tag{7.2}$$

$$T_i = T_{low} + (i-1) \times T, \quad C_i = \frac{ML_{vert}}{T_i}, \qquad i = 1, 2, \cdots, N_s \quad , \tag{7.3}$$

where T is a step length and N_s is the number of the possible thickness. T_{low} represents the blue layer (see Fig. 7.2) with the fixed thickness of 0.5 km and $T_{high} - T_{low}$ represents the yellow layer with the fixed thickness of 2.5 km. T is chosen at a small value compared to T_{low}, which guarantees N_s is not too small (e.g., less than 2) to sample enough thickness T_1, T_2, ⋯, T_{N_s} with equal probability. (e.g., T is chosen as 0.05 km in this case study, thus N_s is calculated as 50.)

Corresponding to the sampled thickness, the ash concentration can be calculated as also a sample from C_1 to C_{N_s}, as shown in Eq. (7.3). Therefore, the mean (C_{mean}) and the standard deviation (C_{std}) of the sampled ash concentrations can

be calculated by Eq. (7.4) and (7.5),

$$\mathrm{C_{mean}} = \frac{1}{N_s}(\mathrm{C}_1 + \mathrm{C}_2 + \cdots + \mathrm{C}_{N_s}) \quad , \tag{7.4}$$

$$\mathrm{C_{std}} = \sqrt{\frac{1}{N_s - 1}[(\mathrm{C}_1 - \mathrm{C_{mean}})^2 + (\mathrm{C}_2 - \mathrm{C_{mean}})^2 + \cdots + (\mathrm{C}_{N_s} - \mathrm{C_{mean}})^2]} \quad . \tag{7.5}$$

$\mathrm{C_{mean}}$ is therefore used in this chapter as the extracted concentration C between the heights [$\mathrm{H_{top}}$ - $\mathrm{T_{low}}$] and $\mathrm{H_{top}}$ (i.e., the blue layer in Fig. 7.2). How much of the mass is distributed to the blue layer ($\mathrm{ML_{blue}}$) can be calculated by Eq. (7.6),

$$\mathrm{ML_{blue}} = \mathrm{C_{mean}} \times \mathrm{T_{low}}. \tag{7.6}$$

Note that, below the height [$\mathrm{H_{top}}$ - $\mathrm{T_{low}}$] (the yellow layer shown in Fig. 7.2), ash concentrations should not be extracted, because the concentrations there can be zero. For example, when $\mathrm{H_{top}}$ equals to 8.0 km and the cloud's thickness is 1.0 km, thus ash concentrations between 7.5 km and 8.0 km can be obtained from Eq. (7.4). However, the ash concentrations at 5.0 km cannot be extracted because actually there is no concentration at that height. Another note is that Eq. (7.5) is calculated based on the most commonly used assumption of Gaussian distribution in error analysis. Gaussian often occurs in nature, and by lack of other information this is therefore a suitable first choice.

7.3.2. Extraction error

Fig. 7.2 and Eq. (7.2) to (7.5) describe the details of the SOO. The operator transforms the 2D ash mass loadings (ML) to 3D ash concentrations (C, here C=$\mathrm{C_{mean}}$). Fig. 7.3**a** is the extracted ash concentrations (C) at the cloud top layer. It can be seen that the extracted ash concentrations in the ash plume are between 0.1 and 0.9 mg $\mathrm{m^{-3}}$.

Now we quantify the extraction error $\mathrm{C_{error}}$ (i.e., error in the extracted concentrations), which is important for a data assimilation system. The extraction error is not equivalent to $\mathrm{C_{std}}$, but depends on both the retrieval error $\mathrm{ML_{error}}$ (error in mass loadings, as shown in Fig. 7.1**c**) and $\mathrm{C_{std}}$. The dependence is described by Eq. (7.7) in terms of uncertainty,

$$\mathrm{U_C} = 1 - (1 - \frac{\mathrm{ML_{error}}}{\mathrm{ML}})(1 - \frac{\mathrm{C_{std}}}{\mathrm{C}}) \quad , \tag{7.7}$$

where the uncertainty ($\mathrm{U_C}$) of the extracted concentrations is calculated based on the derivation uncertainty ($\frac{\mathrm{C_{std}}}{\mathrm{C}}$, normalized standard deviation) and the retrival uncertainty ($\frac{\mathrm{ML_{error}}}{\mathrm{ML}}$). Eq. (7.7) is defined according to the fact that the extraction is performed on the uncertain ash mass loadings, indicating the conditional probability relation. Now $\mathrm{U_C}$ is quantified, the error ($\mathrm{C_{error}}$) in the extracted concentrations can be easily obtained by Eq. (7.8),

$$\mathrm{C_{error}} = \mathrm{C} \times \mathrm{U_C} \quad . \tag{7.8}$$

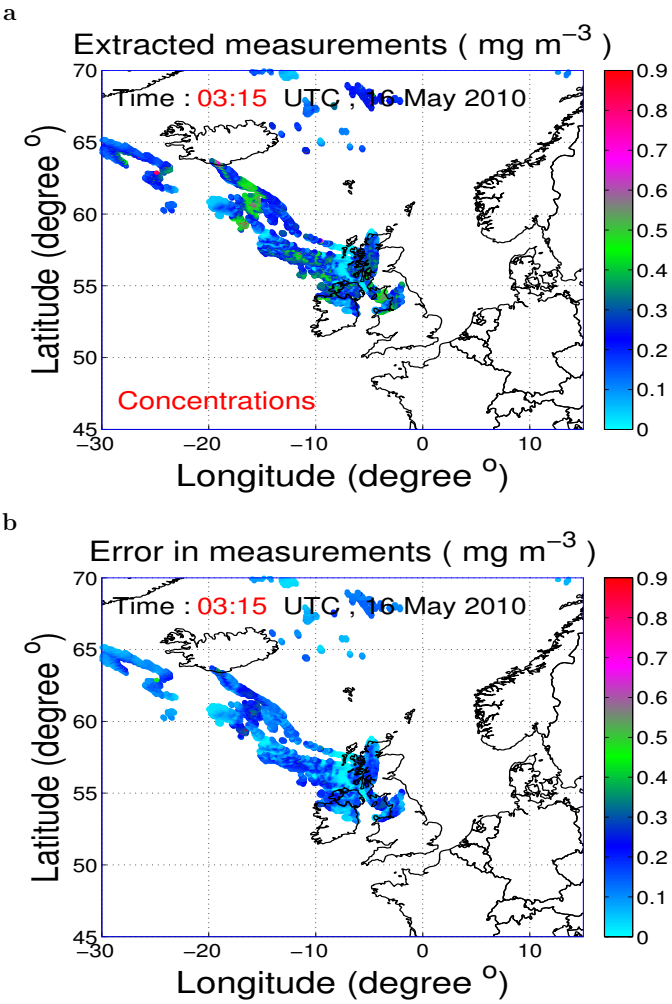

Figure 7.3: **Results of the satellite observational operator (at 16 May 2010 at 03:15 UTC). a**, Extracted ash concentrations at the cloud top layer. **b**, Error in the extracted ash concentrations.

Fig. 7.3**b** is the illustration of the extraction error $\mathrm{C}_{\mathrm{error}}$, which together with C describes the 3D measurements (mean, error) for ensemble-based data assimilation.

The outcome of SOO can be considered as preprocessing to the satellite data assimilation system. The extracted data only represents the data at the cloud top height, which can be taken as the data within the 0.5 km layer thickness. The other layer thickness is also of high importance, which is used for the derivation of uncertainties.

7.4. Assimilation of satellite-extracted ash concentrations

7.4.1. Satellite data assimilation system

The ensemble square root filter (EnSR, see Section 2.2.4), in most applications a more efficient method (Evensen, 2004) than the ensemble Kalman filter, is employed in this chapter to perform the ensemble-based data assimilation. Note that the observational operator ($\mathbf{H}$, see Section 2.2.4) used in EnSR is different from SOO. SOO is an operator designed as a preprocessing procedure before data assimilation, which doesn't depend on the model space and aims to transfer 2D satellite data into 3D measurements for later usage in EnSR. While, $\mathbf{H}$ is an intrinsic operator in the EnSR algorithm as specified in Section 2.2.4.

The model run starts at 00:00 UTC 15 May 2010 with an initial ash load obtained from previous LOTOS-EUROS model run. As the model state changes with time in the numerical simulation (the time step of the model run is 15 minutes used by Fu *et al.* (2015)), the model result from the previous time step is taken as the initial state for the next time step. When the model run arrives at 01:00 UTC 16 May, the volcanic ash state gets continuously modified by the data assimilation process until 00:00 UTC 18 May, by combining the extracted measurements of ash concentrations.

7.4.2. Total measurement error

To assimilate measurements in a simulation model, the total measurement error must be first estimated, which not only contains the extraction error (Section 7.3.2), but also includes an estimate of the model representation error (Fu *et al.*, 2015). The model representation error is the discrepancy between the measurement location and where the model can represent the measurement. Concentration values are defined on discrete grids with a finite resolution at discrete time steps. The grid resolution of the model used in the chapter is 0.25° longitude × 0.125° latitude × 1 km altitude, while the SEVIRI pixel size here is 0.1° longitude × 0.1° latitude. After a careful check on the SEVIRI measurements, a measurement location does not coincide with the grid center point where the concentration value is defined. In this chapter, a preprocessing procedure before data assimilation is employed to average all measurements in a model grid to generate a new measurement value for this model grid. With this approach, one new measurement thus almost corresponds to one model state point, which means the representation error of the model is probably small. For the moment we will therefore not explicitly specify

a model representation error, but implicitly assume that it is zero. Therefore, the total measurement error used in data assimilation, is equal to the extraction error in this chapter.

After the measurements of concentrations are extracted and the total measurement error is quantified, EnSR can be used to combine them with the LOTOS-EUROS model running to reconstruct optimal estimates.

7.4.3. Assimilation performance

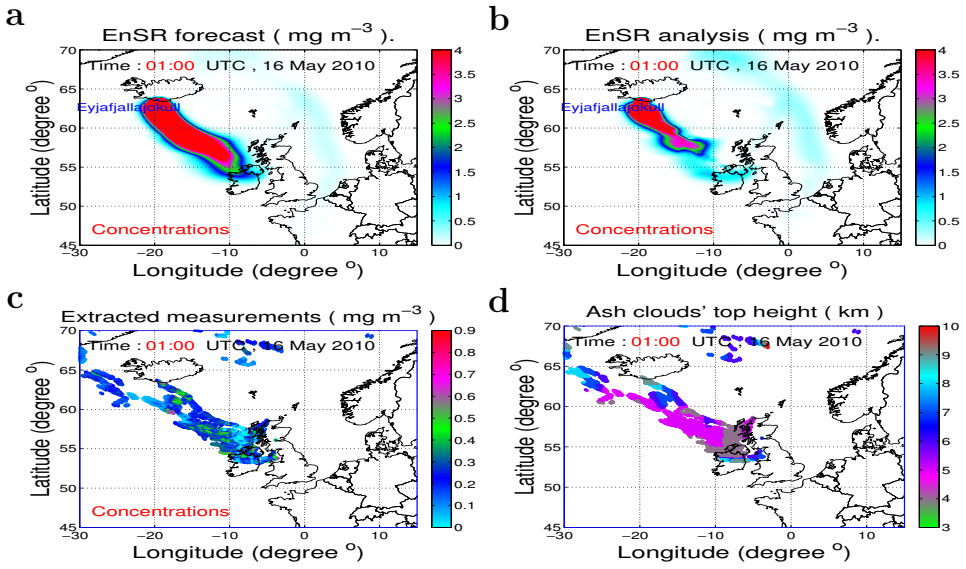

Figure 7.4: **Examination of EnSR effect when assimilating SEVIRI-extracted ash concentrations at 01:00 UTC 16 May 2010. a**, EnSR forecast (ensemble mean) of PM_{10} concentrations. **b**, EnSR analysis (ensemble mean) of PM_{10} concentrations. **c**, Extracted measurements of PM_{10} concentrations from the satellite observational operator. Ash concentrations shown in **a**, **b**, **c** are at the ash cloud top layer height **d**.

In the following, we first examine how data assimilation actually works in the system (see Fig. 7.4). The first assimilation result with EnSR (Fig. 7.4**a**, **b**), at 01:00 UTC 16 May 2010, is shown against the SEVIRI extracted measurements (Fig. 7.4**c**). Ensemble-based data assimilation includes two steps (forecast and analysis, see Section 2.2.4). After one-day of model running started from 00:00 UTC 15 May 2010, the EnSR forecasted state at 01:00 UTC 16 May 2010 is shown in Fig. 7.4**a**. Comparing the state to the extracted measurements (Fig. 7.4**c**), the former (with concentrations higher than 2.0 mg m^{-3} in the main plume) shows a much larger estimation compared to the latter (with concentrations mostly lower than 0.8 mg m^{-3}). After the EnSR analysis step (see Fig. 7.4**b**), the concentrations in large parts are now closer to the extracted measurements. In reality, a potential overestimation is usually elusive and hard to avoid, which is mainly due to lack of sedimentation processes (Fu *et al.*, 2016a). The comparison between the state of

analysis and forecast illustrates that the EnSR assimilation process can potentially solve the problem of overestimation. Note that, in this chapter only PM_{10} ash component is considered in the assimilation system, which is consistent with that during satellite retrievals, only the fine particles (mostly with sizes <10.0 μm) can be detected in the tropospheric volcanic plume based on the robust and reliable retrieval algorithms (Prata, 1989; Corradini *et al.*, 2008). It is also the main mass fraction that is transported at large distances from the source, since most of the large particles (and therefore mass) is removed quickly from the plume.

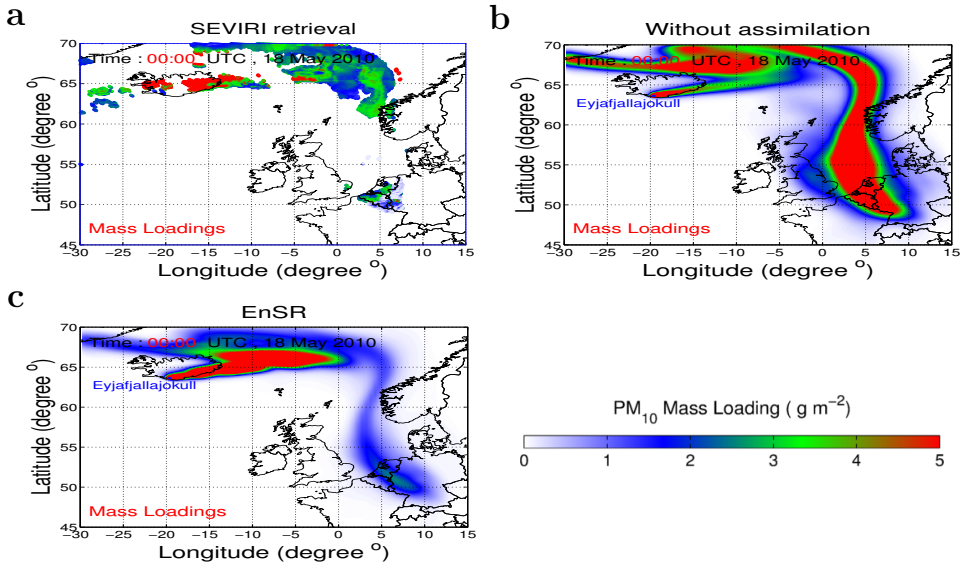

Figure 7.5: **PM_{10} mass loadings with EnSR against the SEVIRI retrieval at 00:00 UTC 18 May 2010.** **a**, SEVIRI retrieved mass loadings. **b**, Simulated mass loadings without assimilation. **c**, Mass loadings (ensemble mean) after 2-days EnSR assimilation.

The results above were compared in terms of concentrations, not the original mass loadings. To guarantee the assimilation performance, the comparison in concentrations only is not sufficient, because the original data is not concentrations but mass loadings. If SOO is not accurate enough for extracting the concentrations at specified heights, the assimilation results still can approximate well the inaccurate extracted concentrations due to the intrinsic forcing of ensemble-based algorithms. Obviously, the approximation in this case is incorrect. Based on this consideration, original measurements (i.e., SEVIRI ash mass loadings, see Fig. 7.5**a**) need to be employed for a further validation. After two-days continuously assimilating SEVIRI measurements of the extracted PM_{10} concentrations, the analyzed volcanic ash state at 00:00 UTC 18 May 2010 is shown in in Fig. 7.5**c**. The conventional simulation without assimilation is also presented (Fig. 7.5**b**), which is currently the commonly used strategy for the simulation of volcanic ash transport (Webley *et al.*, 2012; Fu *et al.*, 2015). It is clear that the mass loadings with EnSR are in a good agreement with the SEVIRI mass loadings, in almost the entire plume. For exam-

ple, in the area of the Netherlands, the mass loadings from EnSR are accumulated to 2.9 – 3.2 g m^{-2}, which is in good match with SEVIRI retrieved 3.1 g m^{-2}. While with the conventional simulation, the mass loadings in this area exceed 5.0 g m^{-2}. It can be seen that EnSR effectively decreases the estimation level compared to the conventional simulation. Because the measurements used in the assimilation system are extracted with the SOO, thus the good results with respect to mass loadings also verify the suitability of SOO for extracting reliable 3D concentrations. Note that here we also checked the SEVIRI mass loading retrieval error and the standard deviation of the mass loadings, and found that both have the same order of magnitude.

7.5. Quantification of the effective forecast duration using aircraft in situ measurements

According to discussions above, the accuracy of volcanic ash state is significantly improved by ensemble-based data assimilation after a continuous assimilation period (e.g., two days). Apparently, with the improved state as initialization, an improved forecast can be obtained (Fu *et al.*, 2015). However, it remains unknown how long the improvement on forecasts will last.

To investigate the effective duration of the improved ash forecasts after assimilation, a one-day forecast is performed by initializing EnSR analyzed state (Fig. 7.5**b**) at 00:00 UTC 18 May 2010. For this investigation, the best way is to compare the forecasted concentrations with high-accurate real-time measurements. Satellite-based data may not be the best choice because usually there are big uncertainties in the measurements (Prata and Prata, 2012; Lu *et al.*, 2016b). Aircraft-based measurements can be the optimal type of observations for this investigation, because the measurements allow sampling of the ash cloud with a high spatial and temporal resolution and by using optical particle counters (OPC) this type of measurement is estimated at a high accuracy of 10% (Weber *et al.*, 2010).

Fortunately, some aircraft measurements on 18 May 2010 from 09:30 to 15:30 UTC are available, which were performed by the group Environmental Measurement Techniques at Düsseldorf university of Applied Sciences. The measurements took place in the North-West part of Germany including the border between the Netherlands and Germany, see Fig. 7.6**a**. The aircraft took off from the airfield "Schwarze Heide" in the Northern part of the Rhein-Ruhr area, headed along the Dutch-German border in the direction of the North Sea, continued towards Hamburg and then returned to the airfield. Along the route, concentrations of PM_{10} and $PM_{2.5}$ were measured. Fig. 7.6**b** and 7.6**c** are the comparison of aircraft PM_{10} measurements against the forecasted concentrations after assimilation and without assimilation.

For the period from 09:30 to 11:00 UTC (Fig. 7.6**b**), although the forecasting time has been over 9 hours (i.e., the last assimilation is 9 hours ago), the forecasted concentrations still have a good match with the accurate aircraft measurements, while the conventional forecast (i.e., forecast without assimilation) doesn't. This result shows the forecast over 11 hours after assimilation has also a high accuracy

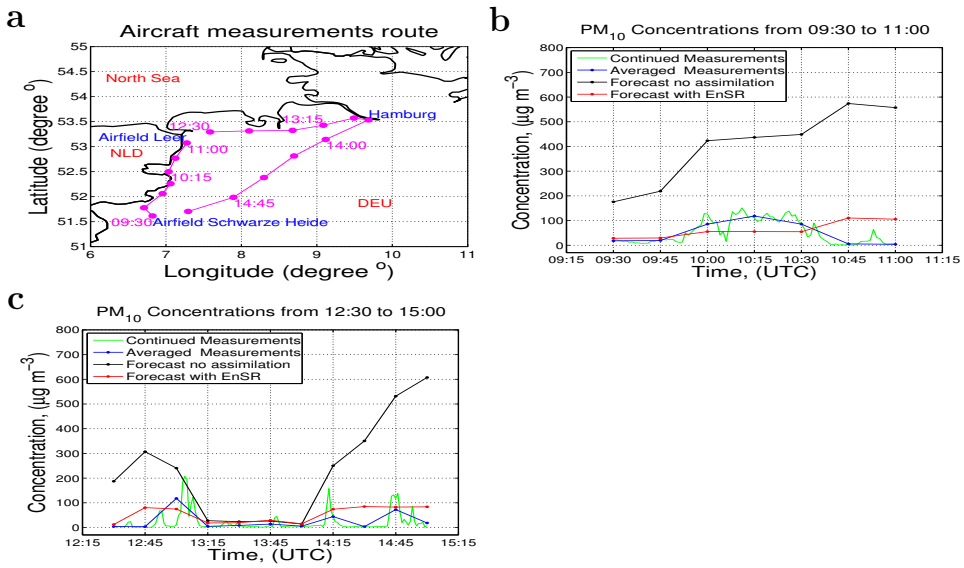

Figure 7.6: **Quantification of effective assimilation forecasts using aircraft measurements (Date: 18 May 2010). a**, Aircraft measurements route. **b**, Comparisons of measurements, forecasts after assimilation (ensemble mean) or without assimilation from 09:30 to 11:00 UTC. **c**, Comparisons from 12:30 to 15:00 UTC.

compared to the measurements. The result can be extended to 15 hours comparing with the other period from 12:30 to 15:00 UTC (Fig. 7.6**c**). Therefore, the validation test with aircraft in situ measurements shows that the regional forecasts (i.e., in the regions of North-West part of Germany) after satellite data assimilation remains valid and accurate for at least 15 hours. This is an important indication about how long a valid regional aviation advice based on the forecast after assimilation can last. This time duration lasts probably even longer, but we don't have aircraft measurements later than 15 hours available to evaluate this. Considering that this duration is likely to be dependent on the weather dynamics, so in this study we quantify the effective time duration at a shorter length for a conservative estimate, e.g., 12 hours (a half day).

7.6. Conclusions

In this chapter, we choose the Eyjafjallajökull volcanic ash plume in May 2010 as the study case. In this chapter, a satellite observational operator (SOO) was developed to translate 2D satellite ash mass loadings to 3D ash concentrations at the top layer of volcanic ash clouds. To extract ash concentrations, not only the SEVIRI data of ash mass loadings, ash cloud top height are employed, but also a reasonable assumption of the ash cloud thickness range (0.5–3 km), at the corresponding horizontal location of the SEVIRI retrieved measurements, are combined. The advantage of SOO is that it can use rough thickness information to get uncertain

concentrations, which are suitable for the data assimilation methodology.

The extracted ash concentration measurements enable us to perform ensemble-based data assimilation in a 3D volcanic ash transport model. By employing a pre-processing procedure before data assimilation to generate new measurement values by averaging all surrounding measurements, the model representation error is approxiamtely zero. The extraction error is also calculated, and the total measurement error (defined as the sum of the extraction error and the model representation error) is therefore quantified, which together with the concentrations describe the 3D measurements (mean, error) for a data assimilation system. The results showed the assimilation significantly reduces the estimation level of the conventional simulation. The accuracy of the volcanic ash state was shown to be significantly improved by the assimilation of satellite mass loadings. The good assimilation performance also verifies the suitability of the proposed SOO.

With the improved volcanic ash state as initialization, improved volcanic ash forecasts are obtained. Quantification using highly accurate aircraft in situ measurements showed that the forecasts after satellite data assimilation remain valid and accurate up to a half day. This effective time period probably lasts even longer and this should be further tested when more aircraft measurements are available.

8

Conclusion

8.1. Overview

The conclusions of this thesis are given in this chapter and are listed as follows (Con1–Con5) corresponding to the research questions and objectives (RQ1–RQ5, see Chapter 1.5)

Con1: In this thesis aircraft-based measurements have been assimilated in an ensemble-based data assimilation system to provide volcanic ash transport forecasts. By assimilating aircraft-based measurements, the forecasts of volcanic ash transport were significantly improved. The advice of aeroplane flying safety made using the assimilation forecast was accurate, whereas the simulation result gave a wrong advice. The aircraft-based measurements should be taken at the same level as the level of interest. When at this level measurements are not available, it has been shown that by assimilating measurements from close levels, an acceptable advice can still be obtained. In twin experiments, through comparing assimilation results of PH, MER and measurement uncertainty with those using wrong uncertainty information, we found that assimilating aircraft-based measurements only performs well when sufficient knowledge of the statistics of the uncertainties is available. Otherwise, accurate assimilation results cannot be guaranteed.

Con2: Aircraft-based type of measurements can perform well in data assimilation systems. Therefore aircraft in situ measurements in distal volcanic ash clouds were assimilated in the LOTOS-EUROS model. During the assimilation, the error of the analyzed volcanic ash state was significantly reduced through assimilating real-life in situ measurements. The improved volcanic ash state after assimilation are the result of an accumulation of all previous assimilation effects. It was shown that all the assimilation steps contribute to

the final result. To examine whether the assimilated volcanic ash states were indeed more accurate than the conventional simulation, a validation with future in situ measurements was conducted. The forecast with assimilation was shown to be more accurate than the conventional forecast without assimilation. It was concluded that the assimilation process performed well in combining with the LOTOS-EUROS transport model with real measurements.

The validation results also revealed that with the transport model alone, it is difficult to accurately model volcanic ash movements. This is probably because model parameters (e.g., the plume height) are uncertain and some processes are missing, for example, coagulation, evaporation, and resuspension. Analysis of the results showed that the data assimilation approach used herein is able to compensate for some of the model's deficiencies. Aircraft in situ measurements have a high accuracy and plays an important role to a successful data assimilation. The aircraft can enter the plume to selectively obtain observations, so that the measurements are in situ and optimal for the ensemble-based data assimilation methodology.

A study has also been carried out on the impact of the improved forecasts of distal ash plume on aviation advice. We found that after assimilation, the most significant improvements on distal ash clouds are in the downwind direction which in our case was mainly Germany. This phenomenon is due to the wind direction and the transport process during the assimilation. Our investigation shows that the accuracy of aviation advice within the area influenced by the data assimilation can significantly benefit from the ensemble-based data assimilation process. The computer experiments revealed that the time period of the improvements in the areas downwind of the assimilated observations can be taken as 24 hours. Based on this result, we suggest to schedule an aircraft measurement campaign at a frequency of once per day. This can be used to provide guidelines for planning future regional measurement tasks. The suggested frequency should be adjusted by the temporal strength (due to wind induced transport) on the assimilation influenced area.

Con3: An accurate localization matrix has been designed for covariance localization to maintain the correctly specified physical forecast error covariances and remove as many of the spurious covariances as possible. As a reference, the physical ("real") forecast error covariances were first approximated as accurate as possible by the sampled forecast error covariance matrix using an ensemble size of 500.

The structure of the forecast error covariances was investigated directional along the wind forcing, but sometimes "upwind-dominant" or "downwind-dominant" or possibly "upwind-downwind-equivalent". By checking the estimated (at an ensemble size of 500) correlations and standard deviations, the latter is revealed as the key to represent the directional strength of the covariances. Therefore, "two-way-anisotropic" and "standard-deviation-

dependent" characteristics were concluded as the two most important properties of the physical forecast error covariances.

Motivated by these analysis, a two-way-tracking approach was proposed to define the localization matrix (for covariance localization), aiming at accurately capturing the specified physical covariances. The forward model was used to track the downwind correlations during the past time. The approach of tracking the upwind correlations was essentially based on the adjoint model to trace the sensitivities of the state with respect to the measurement backwards in time. However, the adjoint was approximated in a practical way using a backward simulation of the original model. In the two-way-tracking formulation, we only considered the model processes of advection and diffusion. This consideration is consistent with the reality that, in the distal part of an ash plume, the advection and diffusion are the dominant processes. After the correlations were two-way tracked, the information of the standard deviations was further included. Finally, a covariance mask required for the localization matrix was created.

According to the experimental results, the two-way-tracking localization (TL) approach was examined and verified as a proper and accurate covariance localization for the application of volcanic ash assimilation. Although our case study showed TL successfully captured the "upwind-dominant" covariances, TL can also work for other types of covariance structures (e.g., "downwind-dominant") because the information of standard deviations was explicitly included in the method. The forecast performance with TL-EnKF was shown to be comparable with the referenced (with a much larger ensemble size) EnKF performance. It indicates that the accumulated inaccuracies of TL-EnKF in approximating the physical error covariances are actually small and acceptable. It also showed that the formulated two-way-tracked covariance mask can roughly capture the covariance patterns with an acceptable accuracy, because it is only used for constructing the domain for the localization procedure. Additionally, it has been shown that the additional computational cost of TL-EnKF is very modest when compared with the referenced EnKF both in serial or parallel cases.

Distance-based localization (DL), the commonly used covariance localization approach, was also performed as comparisons with TL. The experimental results showed that the effect of DL-EnKF either is very small (with a small filtering length scale) or largely over-corrects the concentrations (with a large filtering length scale). Although DL-EnKF is not accurate in dealing with sampling errors compared to TL-EnKF, some other variants of DL-EnKF (e.g., with adaptive radius or radius based on various distance-based functions) might be expected to achieve an acceptable performance for maintaining the "two-way-anisotropic" and "standard-deviation-dependent" covariances. An approach to correct the problem of underestimation in the sampled forecast error covariance matrix, covariance inflation was also investigated when embedded in TL-EnKF. The impact of inflation was clearly positive.

Con4: Based on evaluations on the computational cost of volcanic ash data assimilation, the analysis step turned out to be very expensive. Although some potential approaches can accelerate the initialization and forecast step, there would be no notable improvement to the total computational time due to the dominant analysis step. Therefore, to get an acceptable computational cost, the key is to efficiently reduce the execution time of the analysis step.

After a detailed evaluation on various parts of the analysis stage, the most time-consuming part was revealed. The mask-state algorithm was developed based on a study on the characteristic of the ensemble ash states. The algorithm transforms the full ensemble state matrix into a relatively small matrix using a constructed mask array. Subsequently, the computation of the analysis step was sufficiently reduced. The mask-state algorithm is developed as generic, thus it can be embedded in all ensemble-based data assimilation implementations. The extra computational cost of the algorithm is small and usually neglectable.

The conventional ensemble-based data assimilation with the mask-state algorithm is shown to successfully reduce the total computational time to an acceptable level, i.e., less than the time period of the data assimilation. Consequently, timely and accurate volcanic ash forecasts can be provided for aviation advices. This approach is flexible. It boosts the performance without considering any model-based parallelization, such as domain or component decomposition. Thus, when a parallel model is available, the mask-state approach can be easily combined with the model to gain a further speedup. It implements exactly the standard data assimilation without any approximation and with easy configurations, so that it can be used to accelerate the standard data assimilation in a wide range of applications.

Con5: After getting good results from aircraft data assimilation, the assimilation of satellite data, being the most popular measurements, was investigated. A satellite observational operator (SOO) was developed to translate 2D satellite ash mass loadings to 3D ash concentrations at the top layer of volcanic ash clouds. To extract ash concentrations, not only the SEVIRI data of ash mass loadings, ash cloud top height are employed, but also a reasonable assumption of the ash cloud thickness range (0.5–3 km), at the corresponding horizontal location of the SEVIRI retrieved measurements, are combined. The advantage of SOO is that it can use rough thickness information to get uncertain concentrations, which are suitable for the data assimilation methodology.

The extracted ash concentration measurements enable us to perform ensemble-based data assimilation in a 3D volcanic ash transport model. By employing a preprocessing procedure before data assimilation to generate new measurement values by averaging all surrounding measurements, the

model representation error is approxiamtely zero. The extraction error is also calculated, and the total measurement error (defined as the sum of the extraction error and the model representation error) is therefore quantified, which together with the concentrations describe the 3D measurements (mean, error) for a data assimilation system. The results showed the assimilation significantly reduces the estimation level of the conventional simulation. The accuracy of the volcanic ash state was shown to be significantly improved by the assimilation of satellite mass loadings. The good assimilation performance also verifies the suitability of the proposed SOO.

With the improved volcanic ash state as initialization, improved volcanic ash forecasts are obtained. Quantification using highly accurate aircraft in situ measurements showed that the forecasts after satellite data assimilation remain valid and accurate up to a half day. This effective time period probably lasts even longer and this should be further tested when more aircraft measurements are available.

8.2. Outlook

In this thesis, we applied an off-line approach for model running and simply used the deterministic meteorological input data. These data also contain uncertainties that influence ash cloud transport. In future work, in order to further improve the accuracy of ash forecasting, uncertainties in the meteorological data such as wind speed should also be considered. We may expect that with other types of measurements (e.g., satellite-based or LIDAR-based) together, the assimilation results will be further improved since the aircraft measurements cannot always be obtained. However, for this multi-observation data assimilation, other challenges need to be first considered such as insufficient vertical resolution of certain satellite data.

For two-way-tracking localization, in future, if the aircraft in situ measurements are close to the volcano, not only advection and diffusion, but also some other model processes such as emission, sedimentation and deposition might be important. How to two-way track the localization region, including these processes, remains an interesting issue for future investigations. The TL-EnKF can also be applied to other assimilation applications with in situ measurements. However, for applications where there are a lot of measurements at one analysis time, TL-EnKF may require a large computational effort, unless the two-way track can be done in parallel or it is restricted to a small domain only. Whether this approach is useful for large numbers of observations that constrain a larger portion of the state space is a broader question that will be investigated in future work.

The mask-state algorithm is developed as a generic approach, thus it can be embedded in all ensemble-based data assimilation implementations. The extra computational cost of the algorithm is small and usually neglectable. The mask-state algorithm currently is only designed for the sequential case. Actually this approach

can also be adapted for parallel implementation. This is because the related matrix multiplication can be easily parallelized on multiple processors. Optimization and evaluation on the parallelized mask-state algorithm will be considered in future.

The mask-state is flexible. It boosts the performance without considering any model-based parallelization, such as domain or component decomposition. Thus, when a parallel model is available, the mask-state approach can be easily combined with the model to gain a further speedup. It implements exactly the standard data assimilation without any approximation and with easy configurations, so that it can be used to accelerate the standard data assimilation in a wide range of applications.

The use of aircraft in situ measurements is the essential reason why the mask-state algorithm perfectly works. For each analysis step, the number of measurements are quite small, and the procedure of the singular value decomposition (SVD) costs little. However, in other applications when many measurements are assimilated (e.g., satellite-based or seismic-based data), and the number of measurements is of the same order as the number of state variables, the most time-consuming part will be the SVD. In these cases, the contributions of the mask-state algorithm will be limited.

For assimilating satellite retrieved 2D ash mass loadings in 3D VATDM, we developed a satellite observational operator by considering cases where one singular ash cloud is present. Actually, it could happen that there are several isolated volcanic ash clouds in the vertical direction. The methodology of SOO is also valid for these cases, where the top isolated ash cloud does not correspond to the full but to a fraction of SEVERI ash mass loadings. How to determine the reasonable proportions/percentages for multiple isolated vertical ash clouds will be investigated in future.

References

Amdahl, G. M., *Validity of the Single Processor Approach to Achieving Large Scale Computing Capabilities,* in *Proceedings of the April 18-20, 1967, Spring Joint Computer Conference*, AFIPS '67 (Spring) (ACM, New York, NY, USA, 1967) pp. 483–485.

Anderson, J. L., *An Ensemble Adjustment Kalman Filter for Data Assimilation,* Mon. Wea. Rev. **129**, 2884 (2001).

Anderson, J. L. and Anderson, S. L., *A Monte Carlo Implementation of the Nonlinear Filtering Problem to Produce Ensemble Assimilations and Forecasts,* Mon. Wea. Rev. **127**, 2741 (1999).

Ansmann, A., Tesche, M., Groß, S., Freudenthaler, V., Seifert, P., Hiebsch, A., Schmidt, J., Wandinger, U., Mattis, I., Müller, D., and Wiegner, M., *The 16 April 2010 major volcanic ash plume over central Europe: EARLINET lidar and AERONET photometer observations at Leipzig and Munich, Germany,* Geophys. Res. Lett. **37**, L13810+ (2010).

Arroyo, E., Devegowda, D., Datta-Gupta, A., and Choe, J., *Streamline-Assisted Ensemble Kalman Filter for Rapid and Continuous Reservoir Model Updating,* SPE Reservoir Evaluation & Engineering **11**, 1046 (2013).

Barbu, A. L., Segers, A. J., Schaap, M., Heemink, A. W., and Builtjes, P. J. H., *A multi-component data assimilation experiment directed to sulphur dioxide and sulphate over Europe,* Atmospheric Environment **43**, 1622 (2009).

Bocquet, M., Elbern, H., Eskes, H., Hirtl, M., Žabkar, R., Carmichael, G. R., Flemming, J., Inness, A., Pagowski, M., Pérez Camaño, J. L., Saide, P. E., San Jose, R., Sofiev, M., Vira, J., Baklanov, A., Carnevale, C., Grell, G., and Seigneur, C., *Data assimilation in atmospheric chemistry models: current status and future prospects for coupled chemistry meteorology models,* Atmospheric Chemistry and Physics **15**, 5325 (2015).

Bonadonna, C. and Costa, A., *Plume height, volume, and classification of explosive volcanic eruptions based on the Weibull function, Bulletin of Volcanology*, Bulletin of Volcanology **75**, 1 (2013).

Bonadonna, C., Folch, A., Loughlin, S., and Puempel, H., *Future developments in modelling and monitoring of volcanic ash clouds: outcomes from the first IAVCEI-WMO workshop on Ash Dispersal Forecast and Civil Aviation, Bulletin of Volcanology*, Bulletin of Volcanology **74**, 1 (2012).

Bonadonna, C., Webley, P. W., Hort, M. C., Folch, A., Loughlin, S. C., and Puempel, H., *2nd IUGG-WMO Workshop on Ash Dispersal Forecast and Civil Aviation, Consensual Document,* (2014).

Bukowiecki, N., Zieger, P., Weingartner, E., Jurányi, Z., Gysel, M., Neininger, B., Schneider, B., Hueglin, C., Ulrich, A., Wichser, A., Henne, S., Brunner, D., Kaegi, R., Schwikowski, M., Tobler, L., Wienhold, F. G., Engel, I., Buchmann, B., Peter, T., and Baltensperger, U., *Ground-based and airborne in-situ measurements of the eyjafjallajökull volcanic aerosol plume in Switzerland in spring 2010,* Atmospheric Chemistry and Physics **11**, 10011 (2011).

Casadevall, T. J., *The 1989–1990 eruption of Redoubt Volcano, Alaska: impacts on aircraft operations,* Journal of Volcanology and Geothermal Research **62**, 301 (1994).

Chatterjee, A., Michalak, A. M., Anderson, J. L., Mueller, K. L., and Yadav, V., *Toward reliable ensemble Kalman filter estimates of CO2 fluxes,* J. Geophys. Res. **117**, D22306+ (2012).

Clarisse, L. and Prata, F., *Infrared Sounding of Volcanic Ash,* in *Volcanic Ash* (Elsevier, 2016) pp. 189–215.

Corradini, S., Spinetti, C., Carboni, E., Tirelli, C., Buongiorno, M. F., Pugnahi, S., and Gangale, G., *Mt. Etna tropospheric ash retrieval and sensitivity analysis using moderate resolution imaging spectroradiometer measurements,* Journal of Applied Remote Sensing **2**, 023550 (2008).

Cummings, J. A., *Operational multivariate ocean data assimilation,* Q.J.R. Meteorol. Soc. **131**, 3583 (2005).

Curier, R. L., Timmermans, R., Calabretta-Jongen, S., Eskes, H., Segers, A., Swart, D., and Schaap, M., *Improving ozone forecasts over Europe by synergistic use of the LOTOS-EUROS chemical transport model and in-situ measurements,* Atmospheric Environment **60**, 217 (2012).

Dacre, H. F., Grant, A. L. M., Harvey, N. J., Thomson, D. J., Webster, H. N., and Marenco, F., *Volcanic ash layer depth: Processes and mechanisms,* Geophys. Res. Lett. **42**, 2014GL062454+ (2015).

Deng, X. and Stull, R., *A Mesoscale Analysis Method for Surface Potential Temperature in Mountainous and Coastal Terrain,* Mon. Wea. Rev. **133**, 389 (2005).

Draxler, R. R. and Hess, G. D., *An overview of the HYSPLIT_4 modelling system for trajectories, dispersion, and deposition,* Australian Meteorological Magazine **47**, 295 (1998).

Durant, A. J., Bonadonna, C., and Horwell, C. J., *Atmospheric and Environmental Impacts of Volcanic Particulates,* Elements **6**, 235 (2010).

Durant, A. J. and Rose, W. I., *Sedimentological constraints on hydrometeor-enhanced particle deposition: 1992 Eruptions of Crater Peak, Alaska,* Journal of Volcanology and Geothermal Research **186**, 40 (2009).

EASA, *EASA Safety Information Bulletin 2010-17R7,* (2015).

Eliasson, J., Palsson, A., and Weber, K., *Monitoring ash clouds for aviation,* Nature **475**, 455 (2011).

Emeis, S., Forkel, R., Junkermann, W., Schäfer, K., Flentje, H., Gilge, S., Fricke, W., Wiegner, M., Freudenthaler, V., Grob, S., Ries, L., Meinhardt, F., Birmili, W., Münkel, C., Obleitner, F., and Suppan, P., *Measurement and simulation of the 16/17 April 2010 Eyjafjallajökull volcanic ash layer dispersion in the northern Alpine region,* Atmospheric Chemistry and Physics **11**, 2689 (2011).

Errico, R. M., *What Is an Adjoint Model? Bulletin of the American Meteorological Society*, Bull. Amer. Meteor. Soc. **78**, 2577 (1997).

Evensen, G., *Sequential data assimilation with a nonlinear quasi-geostrophic model using Monte Carlo methods to forecast error statistics,* J. Geophys. Res. **99**, 10143 (1994).

Evensen, G., *The Ensemble Kalman Filter: theoretical formulation and practical implementation, Ocean Dynamics*, Ocean Dynamics **53**, 343 (2003).

Evensen, G., *Sampling strategies and square root analysis schemes for the EnKF, Ocean Dynamics*, Ocean Dynamics **54**, 539 (2004).

Evensen, G., *Data Assimilation – The Ensemble Kalman Filter*, 2nd ed. (Springer, Dordrecht Heidelberg London New York, 2009) Chap. 15.

Evensen, G. and van Leeuwen, P. J., *An Ensemble Kalman Smoother for Nonlinear Dynamics,* Mon. Wea. Rev. **128**, 1852 (2000).

Filgueira, R., Atkinson, M., Tanimura, Y., and Kojima, I., *Applying Selectively Parallel I/O Compression to Parallel Storage Systems,* in *Euro-Par 2014 Parallel Processing*, Lecture Notes in Computer Science, Vol. 8632, edited by Silva, F., Dutra, I., and Santos Costa, V. (Springer International Publishing, 2014) pp. 282–293.

Flemming, J. and Inness, A., *Volcanic sulfur dioxide plume forecasts based on UV satellite retrievals for the 2011 Grímsvötn and the 2010 Eyjafjallajökull eruption,* J. Geophys. Res. Atmos. **118**, 10,172 (2013).

Flentje, H., Claude, H., Elste, T., Gilge, S., Köhler, U., Plass-Dülmer, C., Steinbrecht, W., Thomas, W., Werner, A., and Fricke, W., *The eyjafjallajökull eruption in April 2010 – detection of volcanic plume using in-situ measurements, ozone sondes and a new generation ceilometer network,* Atmospheric Chemistry and Physics Discussions **10**, 14947 (2010).

Folch, A., Costa, A., Durant, A., and Macedonio, G., *A model for wet aggregation of ash particles in volcanic plumes and clouds: 2. Model application,* J. Geophys. Res. **115**, B09202+ (2010).

Francis, P. N., Cooke, M. C., and Saunders, R. W., *Retrieval of physical properties of volcanic ash using Meteosat: A case study from the 2010 Eyjafjallajökull eruption,* J. Geophys. Res. **117**, D00U09+ (2012).

Fu, G., Heemink, A., Lu, S., Segers, A., Weber, K., and Lin, H.-X., *Model-based aviation advice on distal volcanic ash clouds by assimilating aircraft in situ measurements,* Atmospheric Chemistry and Physics **16**, 9189 (2016a).

Fu, G., Lin, H.-X., Heemink, A., Segers, A., Prata, F., and Lu, S., *Satellite data assimilation to improve forecasts of volcanic ash concentrations,* Atmospheric Chemistry and Physics Discussions , 1 (2016b).

Fu, G., Lin, H.-X., Heemink, A., Segers, A., van Velzen, N., Lu, T., Xu, S., and Lu, S., *A mask-state algorithm to accelerate volcanic ash data assimilation,* Geoscientific Model Development Discussions , 1 (2016c).

Fu, G., Lin, H. X., Heemink, A. W., Segers, A. J., Lu, S., and Palsson, T., *Assimilating aircraft-based measurements to improve Forecast Accuracy of Volcanic Ash Transport,* Atmospheric Environment **115**, 170 (2015).

Gaspari, G. and Cohn, S. E., *Construction of correlation functions in two and three dimensions,* Q.J.R. Meteorol. Soc. **125**, 723 (1999).

Gieske, A. S. M., Hendrikse, J., Retsios, V., van Leeuwen, B., Maathuis, B. H. P., Romaguera, M., Sobrino, J. A., Timmermans1, W. J., and Su1, Z., *Processing of MSG-1 SEVIRI data in the thermal infrared–Algorithm development with the use of the SPARC 2004 data set,* in *Proc. WPP-250: SPARC Final Workshop* (Enschede, Netherlands, 2005) pp. 1–8.

Groß, S., Gasteiger, J., Freudenthaler, V., Schnell, F., and Wiegner, M., *Characterization of the Eyjafjallajökull ash-plume by means of lidar measurements over the Munich EARLINET-site,* (SPIE, 2010) pp. 78320M–78320M–8.

Gudmundsson, M. T., Thordarson, T., Höskuldsson, A., Larsen, G., Björnsson, H., Prata, F. J., Oddsson, B., Magnússon, E., Högnadóttir, T., Petersen, G. N., Hayward, C. L., Stevenson, J. A., and Jónsdóttir, I., *Ash generation and distribution from the April-May 2010 eruption of Eyjafjallajökull, Iceland,* Scientific Reports **2** (2012), 10.1038/srep00572.

Hamill, T. M., Whitaker, J. S., and Snyder, C., *Distance-Dependent Filtering of Background Error Covariance Estimates in an Ensemble Kalman Filter,* Mon. Wea. Rev. **129**, 2776 (2001).

Heim, M., Mullins, B. J., Umhauer, H., and Kasper, G., *Performance evaluation of three optical particle counters with an efficient " multimodal" calibration method,* Journal of Aerosol Science **39**, 1019 (2008).

Houtekamer, P. L., He, B., and Mitchell, H. L., *Parallel Implementation of an Ensemble Kalman Filter,* Mon. Wea. Rev. **142**, 1163 (2014).

Houtekamer, P. L. and Mitchell, H. L., *Data Assimilation Using an Ensemble Kalman Filter Technique,* Mon. Wea. Rev. **126**, 796 (1998).

Houtekamer, P. L. and Mitchell, H. L., *A Sequential Ensemble Kalman Filter for Atmospheric Data Assimilation,* Mon. Wea. Rev. **129**, 123 (2001).

Houtekamer, P. L. and Mitchell, H. L., *Ensemble Kalman filtering,* Q.J.R. Meteorol. Soc. **131**, 3269 (2005).

Jones, A., Thomson, D., Hort, M., and Devenish, B., *The U.K. Met Office's Next-Generation Atmospheric Dispersion Model, NAME III,* in *Air Pollution Modeling and Its Application XVII*, edited by Borrego, C. and Norman, A.-L. (Springer US, 2007) pp. 580–589.

Kalnay, E., Ota, Y., Miyoshi, T., and Liu, J., *A simpler formulation of forecast sensitivity to observations: application to ensemble Kalman filters,* Tellus A **64** (2012), 10.3402/tellusa.v64i0.18462.

Keppenne, C. L., *Data Assimilation into a Primitive-Equation Model with a Parallel Ensemble Kalman Filter,* Mon. Wea. Rev. **128**, 1971 (2000).

Keppenne, C. L. and Rienecker, M. M., *Initial Testing of a Massively Parallel Ensemble Kalman Filter with the Poseidon Isopycnal Ocean General Circulation Model,* Mon. Wea. Rev. **130**, 2951 (2002).

Khairullah, M., Lin, H., Hanea, R. G., and Heemink, A. W., *Parallelization of Ensemble Kalman Filter (EnKF) for Oil Reservoirs with Time-lapse Seismic Data,* International Journal of Mathematical, Computational Science and Engineering **7** (2013), waset.org/Publication/16317.

Kylling, A., Kristiansen, N., Stohl, A., Buras-Schnell, R., Emde, C., and Gasteiger, J., *A model sensitivity study of the impact of clouds on satellite detection and retrieval of volcanic ash,* Atmospheric Measurement Techniques **8**, 1935 (2015).

de Laat, A. T. J. and van der A, R. J., *Validation and evaluation of SEVIRIvolcanic ash heights*, Tech. Rep. (Royal Netherlands Meteorological Institute (KNMI), 2012).

Langmann, B., *Volcanic Ash versus Mineral Dust: Atmospheric Processing and Environmental and Climate Impacts,* ISRN Atmospheric Sciences **2013**, 1 (2013).

Liang, B., Sepehrnoori, K., and Delshad, M., *An Automatic History Matching Module with Distributed and Parallel Computing,* Petroleum Science and Technology **27**, 1092 (2009).

Lin, H.-X., Cosman, A., Heemink, A., Stijnen, J., and van Beek, P., *Parallelization of the Particle Model SIMPAR,* in *Advances in Hydro-Science and Engineering*, Vol. 3, edited by Holz, K. P., Bechteler, W., Wang, S. S. Y., and Kawahara, M. (1998).

Lolli, S., Conil, S., Dabas, A., Donovan, D., Gryning, S. E., Mikkelsen, T., Ricketts, H., Sauvage, L., Vaughan, G., Walter, J., and Wienhold, F., *Eyjafjallajökull volcano ash plume detection in the frame of the new constituting lidar network leonet,* (2010) pp. 78320K–78320K–7.

Lu, S., Lin, H. X., Heemink, A., Segers, A., and Fu, G., *Estimation of volcanic ash emissions through assimilating satellite data and ground-based observations,* J. Geophys. Res. Atmos. **121**, 10,971 (2016a).

Lu, S., Lin, H. X., Heemink, A. W., Fu, G., and Segers, A. J., *Estimation of Volcanic Ash Emissions Using Trajectory-Based 4D-Var Data Assimilation,* Mon. Wea. Rev. **144**, 575 (2016b).

Macedonio, G., Costa, A., Scollo, S., and Neri, A., *Effects of eruption source parameter variation and meteorological dataset on tephra fallout hazard assessment: example from Vesuvius (Italy),* Journal of Applied Volcanology **5** (2016), 10.1186/s13617-016-0045-2.

Marenco, F., Johnson, B., Turnbull, K., Newman, S., Haywood, J., Webster, H., and Ricketts, H., *Airborne lidar observations of the 2010 Eyjafjallajökull volcanic ash plume,* J. Geophys. Res. **116**, D00U05+ (2011).

Mastin, L. G., Guffanti, M., Servranckx, R., Webley, P., Barsotti, S., Dean, K., Durant, A., Ewert, J. W., Neri, A., Rose, W. I., Schneider, D., Siebert, L., Stunder, B., Swanson, G., Tupper, A., Volentik, A., and Waythomas, C. F., *A multidisciplinary effort to assign realistic source parameters to models of volcanic ash-cloud transport and dispersion during eruptions,* Journal of Volcanology and Geothermal Research **186**, 10 (2009).

Miffre, A., David, G., Thomas, B., and Rairoux, P., *Characterization of Iceland volcanic aerosols by UV-polarization lidar at Lyon, SW Europe,* (2010) pp. 78320Q–78320Q–9.

Miyazaki, K., Eskes, H. J., and Sudo, K., *A tropospheric chemistry reanalysis for the years 2005–2012 based on an assimilation of OMI, MLS, TES, and MOPITT satellite data,* Atmospheric Chemistry and Physics **15**, 8315 (2015).

Nerger, L. and Hiller, W., *Software for ensemble-based data assimilation systems—Implementation strategies and scalability,* Computers & Geosciences **55**, 110 (2013).

Oberhuber, J. M., Herzog, M., Graf, H.-F., and Schwanke, K., *Volcanic plume simulation on large scales,* Journal of Volcanology and Geothermal Research **87**, 29 (1998).

Oxford-Economics, *The Economic Impacts of Air Travel Restrictions Due to Volcanic Ash, Report for Airbus*, Tech. Rep. (2010).

Pappalardo, G., Amodeo, A., Ansmann, A., Apituley, A., Alados Arboledas, L., Balis, D., Böckmann, C., Chaikovsky, A., Comeron, A., D'Amico, G., De Tomasi, F., Freudenthaler, V., Giannakaki, E., Giunta, A., Grigorov, I., Gustafsson, O., Gross, S., Haeffelin, M., Iarlori, M., Kinne, S., Linné, H., Madonna, F., Mamouri, R., Mattis, I., McAuliffe, M., Molero, F., Mona, L., Müller, D., Mitev, V., Nicolae, D., Papayannis, A., Perrone, M. R., Pietruczuk, A., Pujadas, M., Putaud, J.-P., Ravetta, F., Rizi, V., Serikov, I., Sicard, M., Simeonov, V., Spinelli, N., Stebel, K., Trickl, T., Wandinger, U., Wang, X., Wagner, F., and Wiegner, M., *Earlinet observations of the eyjafjallajökull ash plume over europe,* (2010) pp. 78320J–78320J–9.

Pavolonis, M. J., *Advances in Extracting Cloud Composition Information from Spaceborne Infrared Radiances—A Robust Alternative to Brightness Temperatures. Part I: Theory,* J. Appl. Meteor. Climatol. **49**, 1992 (2010).

Petrie, R. E. and Dance, S. L., *Ensemble-based data assimilation and the localisation problem,* Weather **65**, 65 (2010).

Prata, A. J., *Infrared radiative transfer calculations for volcanic ash clouds,* Geophys. Res. Lett. **16**, 1293 (1989).

Prata, A. J. and Prata, A. T., *Eyjafjallajökull volcanic ash concentrations determined using Spin Enhanced Visible and Infrared Imager measurements,* J. Geophys. Res. **117**, D00U23 (2012).

Prata, A. T., Siems, S. T., and Manton, M. J., *Quantification of volcanic cloud top heights and thicknesses using A-train observations for the 2008 Chaitén eruption,* J. Geophys. Res. Atmos. **120**, 2014JD022399+ (2015).

Quinn, J. C. and Abarbanel, H. D. I., *Data assimilation using a GPU accelerated path integral Monte Carlo approach,* Journal of Computational Physics **230**, 8168 (2011).

Riishojgaard, L. P., *A direct way of specifying flow-dependent background error correlations for meteorological analysis systems,* Tellus A **50**, 42 (1998).

Sakov, P. and Oke, P. R., *A deterministic formulation of the ensemble Kalman filter: an alternative to ensemble square root filters,* Tellus A **60**, 361 (2008a).

Sakov, P. and Oke, P. R., *Implications of the Form of the Ensemble Transformation in the Ensemble Square Root Filters,* Mon. Wea. Rev. **136**, 1042 (2008b).

Schaap, M., Timmermans, R. M. A., Roemer, M., Boersen, G. A. C., Builtjes, P. J. H., Sauter, F. J., Velders, G. J. M., and Beck, J. P., *The LOTOS EUROS model: description, validation and latest developments,* International Journal of Environment and Pollution **32**, 270+ (2008).

Schäfer, K., Birmili, W., Cyrys, J., Emeis, S., Forkel, R., Gilge, S., Münkel, C., Pitz, M., Ries, L., and Suppan, P., *Temporal and spatial structure of a volcanic ash cloud: ground-based remote sensing and numerical modeling,* (2010) pp. 78320R–78320R–12.

Schäfer, K., Thomas, W., Peters, A., Ries, L., Obleitner, F., Schnelle-Kreis, J., Birmili, W., Diemer, J., Fricke, W., Junkermann, W., Pitz, M., Emeis, S., Forkel, R., Suppan, P., Flentje, H., Gilge, S., Wichmann, H. E., Meinhardt, F., Zimmermann, R., Weinhold, K., Soentgen, J., Münkel, C., Freuer, C., and Cyrys, J., *Influences of the 2010 Eyjafjallajökull volcanic plume on air quality in the northern Alpine region,* Atmospheric Chemistry and Physics **11**, 8555 (2011).

Schmetz, J., Pili, P., Tjemkes, S., Just, D., Kerkmann, J., Rota, S., and Ratier, A., *An Introduction to Meteosat Second Generation (MSG),* Bull. Amer. Meteor. Soc. **83**, 977 (2002).

Schumann, U., Weinzierl, B., Reitebuch, O., Schlager, H., Minikin, A., Forster, C., Baumann, R., Sailer, T., Graf, K., Mannstein, H., Voigt, C., Rahm, S., Simmet, R., Scheibe, M., Lichtenstern, M., Stock, P., Rüba, H., Schäuble, D., Tafferner, A., Rautenhaus, M., Gerz, T., Ziereis, H., Krautstrunk, M., Mallaun, C., Gayet, J. F., Lieke, K., Kandler, K., Ebert, M., Weinbruch, S., Stohl, A., Gasteiger, J., Groß, S., Freudenthaler, V., Wiegner, M., Ansmann, A., Tesche, M., Olafsson, H., and Sturm, K., *Airborne observations of the Eyjafjalla volcano ash cloud over Europe during air space closure in April and May 2010,* Atmospheric Chemistry and Physics **11**, 2245 (2011).

Searcy, C., Dean, K., and Stringer, W., *PUFF: A high-resolution volcanic ash tracking model,* Journal of Volcanology and Geothermal Research **80**, 1 (1998).

Segers, A. J., *Data Assimilation in Atmospheric Chemistry Models Using Kalman Filtering* (Delft Univ Pr, 2002).

Sparks, R. S. J., Burski, M. I., Carey, S. N., Gilbert, J. S., Glaze, L. S., Sigurdsson, H., and Woods, A. W., *Volcanic Plumes*, 1st ed. (Wiley, 1997).

Stohl, A., Prata, A. J., Eckhardt, S., Clarisse, L., Durant, A., Henne, S., Kristiansen, N. I., Minikin, A., Schumann, U., Seibert, P., Stebel, K., Thomas, H. E., Thorsteinsson, T., Tørseth, K., and Weinzierl, B., *Determination of time- and height-resolved volcanic ash emissions and their use for quantitative ash dispersion modeling: the 2010 eyjafjallajökull eruption,* Atmospheric Chemistry and Physics **11**, 4333 (2011).

Tavakoli, R., Pencheva, G., and Wheeler, M. F., *Multi-level Parallelization of Ensemble Kalman Filter for Reservoir History Matching,* in *SPE Reservoir Simulation Symposium* (Society of Petroleum Engineers, 2013).

Tesche, M., Ansmann, A., Hiebsch, A., Mattis, I., Schmidt, J., Seifert, P., and Wandinger, U., *Lidar observations of the Eyjafjallajokull volcanic ash plume at Leipzig, Germany,* (2010) pp. 78320L–78320L–9.

van Velzen, N. and Segers, A. J., *A problem-solving environment for data assimilation in air quality modelling,* Environmental Modelling & Software **25**, 277 (2010).

van Velzen, N. and Verlaan, M., *COSTA a problem solving environment for data assimilation applied for hydrodynamical modelling,* Meteorologische Zeitschrift **16**, 777 (2007).

Verlaan, M. and Heemink, A. W., *Tidal flow forecasting using reduced rank square root filters, Stochastic Hydrology and Hydraulics*, Stochastic Hydrology and Hydraulics **11**, 349 (1997).

Walcek, C. J. and Aleksic, N. M., *A simple but accurate mass conservative, peak-preserving, mixing ratio bounded advection algorithm with FORTRAN code,* Atmospheric Environment **32**, 3863 (1998).

Weber, K., Eliasson, J., Vogel, A., Fischer, C., Pohl, T., van Haren, G., Meier, M., Grobéty, B., and Dahmann, D., *Airborne in-situ investigations of the Eyjafjallajökull volcanic ash plume on Iceland and over north-western Germany with light aircrafts and optical particle counters,* Atmospheric Environment **48**, 9 (2012).

Weber, K., Vogel, A., Fischer, C., van Haren, G., and Pohl, T., *Airborne measurements of the Eyjafjallajökull volcanic ash plume over northwestern Germany with a light aircraft and an optical particle counter: first results,* (2010) pp. 78320P–78320P–15.

Webley, P. W., Steensen, T., Stuefer, M., Grell, G., Freitas, S., and Pavolonis, M., *Analyzing the Eyjafjallajökull 2010 eruption using satellite remote sensing, lidar and WRF-Chem dispersion and tracking model,* J. Geophys. Res. **117**, D00U26+ (2012).

Webley, P. W., Stunder, B. J. B., and Dean, K. G., *Significant eruption source parameter(s) for operational ash cloud transport and dispersion models,* Journal of Volcanology and Geothermal Research **186(1-2)**, 108 (2009b).

Webster, H. N., Thomson, D. J., Johnson, B. T., Heard, I. P. C., Turnbull, K., Marenco, F., Kristiansen, N. I., Dorsey, J., Minikin, A., Weinzierl, B., Schumann, U., Sparks, R. S. J., Loughlin, S. C., Hort, M. C., Leadbetter, S. J., Devenish, B. J., Manning, A. J., Witham, C. S., Haywood, J. M., and Golding, B. W., *Operational prediction of ash concentrations in the distal volcanic cloud from the 2010 Eyjafjallajökull eruption,* J. Geophys. Res. **117**, D00U08+ (2012).

Wiegner, M., Gasteiger, J., Groß, S., Schnell, F., Freudenthaler, V., and Forkel, R., *Characterization of the Eyjafjallajökull ash-plume: Potential of lidar remote sensing,* Physics and Chemistry of the Earth, Parts A/B/C **45-46**, 79 (2012).

Winker, D. M., Liu, Z., Omar, A., Tackett, J., and Fairlie, D., *CALIOP observations of the transport of ash from the Eyjafjallajökull volcano in April 2010,* J. Geophys. Res. **117**, D00U15 (2012).

Witham, C. S., Hort, M. C., Potts, R., Servranckx, R., Husson, P., and Bonnardot, F., *Comparison of VAAC atmospheric dispersion models using the 1 November 2004 Grimsvötn eruption,* Met. Apps **14**, 27 (2007).

Zehner, C., ed., *Proceedings of the ESA-EUMETSAT workshop on the 14 April to 23 May 2010 eruption at the Eyjafjoll volcano,South Iceland* (ESA communication Production Office, 2010).

Zhang, L., *A size-segregated particle dry deposition scheme for an atmospheric aerosol module,* Atmospheric Environment **35**, 549 (2001).

Epilogue

For future, I want to contribute to all data assimilation related fields.

Guangliang Fu
July 2016

Acknowledgements

This work was carried out at Delft University of Technology in a close cooperation with TNO. I thank the financial support from China Scholarship Council. This PhD thesis is a result of support and guidance from many people. I extend my thanks to all the people I worked with during my PhD life and in particular to some of them.

Firstly, I would like to thank my supervisors Hai Xiang Lin and Arnold Heemink. When I started my PhD, I knew nothing about how to do an independent PhD researcher in the Netherlands. This was because I used to get direct instructions from supervisors and also highly dependent. Thank both of you for guiding me, at the start, that how to independently build up knowledge, stimulate my potentials, discuss and connect with other experts, find and execute research ideas efficiently. Not just for the thesis, but this experience is the most important accomplishment from my PhD life, and will be benefitting my whole life. Besides in the professional field, I am also grateful to Hai Xiang and Arnold for their every kind help to my personal life. I appreciate their infinite power of understanding every problem I had. I cannot express how lucky I am to have them as my PhD supervisors. To be honest, they are not just supervisors to me, but dear friends who I can talk and discuss any problems.

Working with Arjo Segers has been a very nice experience for me, who supervises and helps me with all sort technical problems with LOTOS-EUROS. Thank you for providing me the LOTOS-EUROS model for my volcanic ash assimilation work. Without your kind assistance, I won't be able to obtain these interesting results. Also, your comments along my whole PhD period have brought me to a professional level in the broad atmospheric society. As a friend, you always support my every ambitious attempt. I have to admit that I have a personality at fearing nothing, so that I submitted my 2nd paper to Nature. After I got rejection, you encouraged me at earliest time and suggested me to take this as a nice experience. It means a lot to me.

Sha Lu, thank you for always giving me critical comments on my research, not only at our monthly meeting, but also in our daily discussions. Your strong theoretical knowledge lets me feel ashamed often, although my background was also mathematics. I enjoyed every argue we had, which helped me a lot to strengthen my research more significant and reasonable with more deep analysis.

I would like to thank my data assimilation collegues: Prof. Martin Verlaan, Dr. Nils van Velzen, Dr. Umer Altaf. You always selflessly share your knowledge to me. Martin, I appreciate your kind support and patience to answer my every stupid question and your very important comments to improve my papers. Nils, thank you for your assistance of OpenDA and your programming skills are always impressive to

me. Umer, thanks for every nice discussion with you on assimilation methodology. I would also want to thank my group dear collegues and my frieds: Evelyn Sharabi, Dorothée Engering, Kees Lemmens, Wim van Horssen, Peter Wilders, you always help provide me the most convenient and comfortable working atmospheres. I also want to thank my close friends Shiming Xu, Kaihua Xi, Jianbing Jin, Xinchao Li, Changgong Zhang, Zhijie Ren, Yunlong Gong, Yu Xin, Jianbin Fang, Yong Guo, Cong Xiao, Senlei Wang, Yandong Wang, Nick Gaiko, Hyder Syed, et al. Without your company, my PhD life would never be interesting. Here I am very grateful to my English teacher Claire Taylor for her kindly assisting with correction of English grammars for my published journal articles.

During my PhD research, I worked also with some international experts on volcanic ash measurements. I thank them for their big support of data and most importantly how to efficiently represent and use the data. Dr. Fred Prata (Nicarnica Aviation, Norway), as a leading researcher in satellite retrieval, thank you for providing the validated satellite measurements. I really appreciate your patience to answer me and explain every detail of the satellite retrieved measurements. Without your assistance, I cannot clearly know the knowledge and eventually find an efficient way to use the measurements. Thank you very much. Prof. Konadin Weber (Hochschule Düsseldorf, Germany), I would express my thanks to you for prividing me aircraft in situ measurements. Without employing these highly accurate measurements in both assimilation and validation, I cannot prove my data assimilation approach work nice for volcanic ash forecasts. Many thanks also to Thorgeir Palsson (Reykjavik University, Iceland). It is you that introduced the research topic of volcanic ash forecasts. Thank you for helping me in my first year to build up the motivation of this topic.

A very special place in my mind to European Geosciences Union. It helps me to build up my connections with experts on both modeling, measurements and assimilation fields. I am very grateful for these experiences, which will help much to my future research. I want to thank SURFsara, the Netherlands Supercomputing Center for providing me the use of the Cartesius cluster in performing the parallel experiments.

I would like to thank Shandong University in China and so many respects and thanks to Prof. Tongchao Lu and Prof. Aijie Cheng who are both my supervisors in my master period in China. Thank you for recommending me and providing me the opportunity to TU Delft to do a PhD research.

Finally, I want to thank my family, for all their support, encouragements which always keep me going further.

Guangliang Fu
Delft, June 2016

Curriculum Vitæ

Guangliang Fu was born on 6 May 1986 in Shandong, China. He finished his undergraduate degree in Numerical Mathematics in 2009 at Shandong University, China. After this, Guangliang Fu continued his studies in Numerical Mathematics at Shandong University. He received the title of Master of Science in Numerical Mathematics from this university in 2012.

Since 2012, Guangliang Fu has been working on his PhD project at the Delft Institute of Applied Mathematics at Delft University of Technology, the Netherlands. He worked on the project: Ensemble-based data assimilation to improve volcanic ash forecasts. This project investigated the benefits of ensemble-based data assimilation with available observations to improve volcanic ash forecast accuracy. In his project, in situ aircraft measurements of ash concentrations and infrared satellite measurements of volcanic ash mass loadings were used as the observations into the assimilation scheme. The project has been supervised by Prof. H.X. Lin and Prof. A.W. Heemink and in a close cooperation with Dr. A.J. Segers at TNO, Department of Climate, Air and Sustainability, Utrecht, the Netherlands.

List of Publications

- **Journals**

1. **Fu, G.***, Lin, H.X., Heemink, A.W., Segers, A.J., Lu, S., and Palsson, T.: *Assimilating aircraft-based measurements to improve Forecast Accuracy of Volcanic Ash Transport*, **Atmospheric Environment**, 115, 170-184, 2015. doi:*10.1016/j.atmosenv.2015.05.061*.

2. **Fu, G.***, Heemink, A., Lu, S., Segers, A., Weber, K. and Lin, H.-X.: *Model-based aviation advice on distal volcanic ash clouds by assimilating aircraft in situ measurements*, **Atmospheric Chemistry and Physics**, 16 (14), 9189-9200, 2016. doi:*10.5194/acp-16-9189-2016*.

3. **Fu, G.***, Lin, H.-X., Heemink, A., Segers, A., Verlaan, M., Lu, T.: *A two-way-tracking localized ensemble Kalman filter for assimilating aircraft in situ volcanic ash measurements*, **Monthly Weather Review (under review)**.

4. **Fu, G.***, Lin, H.-X., Heemink, A., Segers, A., Prata, F., and Lu, S.: *Satellite data assimilation to improve forecasts of volcanic ash concentrations*, **Atmospheric Chemistry and Physics Discussions** 1-22, 2016. doi:*10.5194/acp-2016-436*.

5. **Fu, G.***, Lin, H.-X., Heemink, A., Segers, A., van Velzen, N., Lu, T., Xu, S., and Lu, S.: *A mask-state algorithm to accelerate volcanic ash data assimilation*, **Geoscientific Model Development Discussions** 1-19, 2016. doi:*10.5194/gmd-2016-208*.

- **Conferences**

1. **Fu, G.***, Lin, H.X., Heemink, A.W., Segers, A.J., Lu, S., and Palsson, T.: *Assimilating Aircraft-based measurements to improve the State of Distal Volcanic Ash Cloud* , **EGU General Assembly Conference 2015**, *(http:meetingorganizer.copernicus.org/EGU2015/EGU2015-6086.pdf)*.

2. **Fu, G.***, Lin, H.X., Heemink, A.W., Segers, A.J. and Lu, S..: *Assimilation of satellite-retrieved data to improve forecasts of volcanic ash concentrations* , **EGU General Assembly Conference 2016**, *(http:meetingorganizer.copernicus.org/EGU2016/EGU2016-3166.pdf)*.

3. **Fu, G.***, Lin, H.X., Heemink, A.W., Segers, A.J. and Lu, S..: *An accelerated data assimilation approach for volcanic ash forecast* , **EGU**

General Assembly Conference 2016,
(http://meetingorganizer.copernicus.org/EGU2016/EGU2016-10360-2.pdf).